

**QUANTIFICATION OF CORONARY FLOW VELOCITY VIA
CONTRAST DISPERSION PATTERNS: INSIGHTS FROM
COMPUTATIONAL MODELING AND COMPUTED
TOMOGRAPHY EXPERIMENTS**

By

Parastou Eslami

A dissertation submitted to Johns Hopkins University in conformity with the
requirements for the degree of Doctor of Philosophy

Baltimore, Maryland
June, 2016

© 2016 Parastou Eslami
All Rights Reserved

A B S T R A C T

Advances in multi-detector cardiac computed tomography (CT) have expanded its use beyond coronary atherosclerosis to a suite of functional myocardial imaging options that now closely parallels magnetic resonance imaging; including ventricular function, viability and perfusion. Despite these advances, there are currently no existing CT based methods to assess coronary luminal blood flow/hemodynamics.

Recent studies have shown that CT derived axial transluminal contrast gradients (TCG) are greater in coronary arteries with atherosclerotic lesions when compared with normal arteries; suggesting TCG may be related to local coronary hemodynamics. Despite this provocative observation, the basic mechanisms responsible for TCG and their possible connection with coronary hemodynamics have not been explained.

In the current work, we hypothesize that TCG is related to the temporal gradients of the contrast bolus and that TCG encodes coronary flow velocity. An analytical relationship between spatial (TCG) and temporal measurements of contrast dispersion is proposed and this allows for estimation of coronary flow velocity from TCG. This is a novel method (called transluminal attenuation flow encoding-TAFE) integrates: a) anatomic features of the coronary vessels, b) TCG and c) temporal gradients in contrast associated with the arterial input function (AIF) that are readily available in conventional CT to allow non-invasive CT derived coronary flow quantification.

The TAFE formulation is validated in computational models as well as in CT-compatible experimental phantom studies with configurations that mimic coronary vessels. The experimental studies revealed factors that were absent in computational modeling

including imaging artifacts and imaging reconstruction kernels where by imaging analysis TAFE has been modified.

In addition, computational simulations of the aortic arch including a semi-patient specific aortic valve model were performed to study contrast dispersion through the arch. This study was done to assess a key assumption in TAFE, that the clinically available AIF at the descending aorta can be used as an accurate estimate of the AIF at the coronary ostium.. The work provides support for the ability of TAFE to provide quantitative estimates of coronary flow velocity but also reveals a number of issues that require further assessment for improved accuracy of TAFE.

Advisor: Rajat Mittal, Ph.D.

Readers: Marcus Chen, MD.

Albert Lardo, Ph.D.

Jung-Hee Seo, Ph.D.

ACKNOWLEDGEMENTS

In preparation and completion of this thesis, my sincere gratitude goes to my advisor and mentor, Prof. Rajat Mittal for all the guidance, encouragement and support he provided throughout my graduate years. I am grateful and honored to have him as my mentor.

My co-advisor, Dr. Marcus Chen at NIH, although I had a pleasure working with him later in my graduate years, provided me with instant support and mentorship. I am so lucky to have worked with someone with such deep understanding of cardiovascular systems and medical imaging. His teachings transformed my view and knowledge about medical imaging. I would also like to thank the friendly NIH staff, including Shirley Rollison for making my research experience very productive and pleasant.

Many thanks to our collaborator at Johns Hopkins Hospital, Dr. Albert Lardo whom I had a privilege to know right from the beginning. His friendly manner made going back to school after two years of working in industry much smoother. Dr. Lardo's multi-disciplinary perspective always inspired me to view cardiovascular problems with an engineer mind.

I would be forever thankful and grateful to Dr. Jung-Hee Seo who patiently and kindly answered all my none-ending questions. Without you and your guidance, my Ph.D. years would be spent in many lost hours. Thank you!

I would also thank my friends and colleagues in our lab, at FPCL and outside. My years at Hopkins although filled with many long hour days (and nights!), was truly joyful and you made it all possible. I decide not to mention any names in the fear of leaving someone behind. I made many good friends here and hope to continue my friendship for many years to time.

My path to where I am would be impossible without the support and unconditional love of my parents, Ali and Mahshid. Among many things, I learned perseverance and hard work from you and your selfless sacrifices made the person I am today allowing me to follow my dreams. Parnian, we grew so much closer when we left Iran together. Thank you for being the "bigger" sister at the times I was not; I could not ask for a better younger sister and a friend.

Last, but certainly not least, I would like to thank Omid for his endless love and support. You inspire and encourage me to be strong and strive to become a better person every day. Our friendship more than a decade ago has evolved to become the most beautiful friendship I have ever had. Thank you for being my rock and my best friend!

TABLE OF CONTENTS

ABSTRACT.....	ii
ACKNOWLEDGEMENTS	iv
TABLE OF CONTENTS	v
LIST OF TABLES	x
LIST OF FIGURES	xi
CHAPTER 1: INTRODUCTION.....	1
1.1. MOTIVATION AND BACKGROUND	1
1.1.1. Trends in Coronary Heart Disease (CHD) and Diagnostics	1
1.1.1.1. Epidemiology of CHD	1
1.1.1.2. Current Standard CHD Diagnosis	1
1.1.2. Trends in Computing	4
1.2. LITERATURE REVIEW	5
1.2.1. Existing Coronary Flow Assessment and Limitations.....	5
1.3. CURRENT OBJECTIVES	9
Objective 1: Study the flow physics associated with TCG and explore methods for estimating coronary flow velocity from transluminal contrast dispersion patterns obtained from CT angiography.....	9
Objective 2: Validate and modify the TAFE formulation based on preclinical and phantom studies.....	10

Objective 3: Examine AIF dispersion in the aortic arch.....	11
CHAPTER 2: COMPUTATIONAL MODELING FOR FLOW AND CONTRAST DISPERSION IN CARDIOVASCULAR FLOWS.....	12
2.1. MEDICAL IMAGING – COMPUTED TOMOGRAPHY ANGIOGRAPHY (CTA) 15	
2.2. MODEL CONSTRUCTION	17
2.2.1. Vessel segmentation.....	17
2.2.1.1. Coronary Arteries.....	17
2.2.1.2. Aorta and Aortic Arch.....	18
2.2.1.3. Aortic valve (AV) modeling	20
2.2.1.4. Surface Registration and Interpolation.....	24
2.3. GOVERNING EQUATIONS AND CFD SOLVERS.....	26
2.3.1. ViCar3D	26
2.3.1.1. Immersed Boundary Method.....	26
2.3.1.2. Scalar Addition for Contrast Dispersion	29
2.3.2. ANSYS CFX.....	30
CHAPTER 3: HEMODYNAMICS OF LARGE VESSELS VIA DISPERSION OF CONTRAST AGENT IN CTA	32
3.1. INTRODUCTION	32
3.2. METHODS	35

3.2.1.	Governing Equations	35
3.2.2.	Arterial Input Function (AIF)	36
3.2.3.	Arterial Attenuation and TCG Calculation	39
3.2.4.	Fractional Flow Reserve	40
3.2.5.	Analytical Investigation of Mechanism for TCG	41
3.2.6.	Quantitative Flow rate Estimation using TCG.....	45
3.3.	RESULTS	48
3.3.1.	Idealized Model	48
3.3.2.	Physiological Model Based on Coronary CT Angiography	54
3.4.	DISCUSSION	56
3.5.	SUMMARY	62

CHAPTER 4: ASSESSMENT OF TAFE VIA CARDIAC CT COMPATIBLE

PHANTOM EXPERIMENTS	64
4.1. INTRODUCTION	64
4.1.1. Partial Volume Averaging	66
4.2. MATERIALS & METHODS	68
4.2.1. Theory	68
4.2.2. Experimental Setup	69
4.2.3. Image Reconstruction	74
4.2.4. Image Analysis and Phantom Segmentation.....	76

4.2.5.	<i>TAFE</i> Analysis	78
4.2.5.1.	Errors due to Flow Non-Uniformity.....	80
4.2.5.2.	Errors due to Imaging Resolution	85
4.3.	RESULTS AND DISCUSSION	87
4.3.1.1.	Limitations and Caveats	91
4.4.	SUMMARY	93
CHAPTER 5: CONTRAST DISPERSION IN AORTIC ARCH AND EFFECT OF FLOW PATTERN ON ARTERIAL INPUT FUNCTION		94
5.1.	INTRODCUTION	94
5.2.	METHODS	100
5.2.1.	Segmentation and Generation of CFD-Ready Aorta Model.....	101
5.2.2.	Aortic Valve Modeling and Motion.....	103
5.2.3.	CFD Model and Non-Dimensional Parameters	107
5.3.	RESULTS	110
5.3.1.	Flow Patterns	110
5.3.2.	Contrast Dispersion.....	116
5.1.	DISCUSSION	120
5.1.1.	Flow Pattern and its Correlation with Contrast Dispersion	120
5.1.2.	AIF Comparison in the Ascending and Descending Aorta.....	124
5.1.3.	Effect of Schmidt Number on Contrast Dispersion and Diffusion	126

5.1.4.	Transient Time vs. Transport Time	127
5.2.	SUMMARY	132
CHAPTER 6: CONCLUSIONS		134
6.1.	SUMMARY	134
6.2.	Ongoing and Future Work	135
LIST OF REFERENCES.....		139

LIST OF TABLES

Table 4-1. List of flowrates estimated by TAFE and the corresponding corrections for the straight phantom.....	89
Table 4-2. List of flowrates estimated by TAFE and the corresponding corrections for the tapered phantom.....	90
Table 5-1. List of flow and contrast concentration parameter	106
Table 5-2. List of calculated slope of the AIF (dC/dt) at $t \approx 4s$ for the shifted AIF in cardiac cycle.....	126

LIST OF FIGURES

Figure 1-1 Representative example of transluminal contrast gradient for a stenosed artery. Luminal cross sections are sampled every 0.5 mm and plotted over the vessel length to obtain an axial variation of cross-sectional averaged attenuation (HU) (top figure). Bottom figure shows the axial and cross-sectional visualizations of lumen area by contrast agent. HU is the Hounsfield unit for the attenuation level. The lesion section is shown with an arrow. CT imaging is acquired using a 320-row detector CT scanner (AquilionTMOne -Toshiba Medical Systems Corporation, Otawara, Japan).	4
Figure 2-1. Framework for image-based patient-specific computational modeling.....	14
Figure 2-2. Comparison of different non-invasive imaging modalities. (Figure taken from (Blankstein, 2012))	16
Figure 2-3. Steps involved in construction of the CFD-ready geometry. Coronary artery probing and segmentation for each plane (a). 3D model construction based on the centerline and cross-sectional area detection (b). STL extraction of the vessel from the DICOM files. (d) Final geometry after “cleaning up” the raw output into STL format.....	18
Figure 2-4. Steps involved in segmentation and creation of model-ready geometry. A dynamic “region growing” methodology was used to segment the aorta (a). The 3D model of the segmented artery is constructed using volume rendering (b). The final version of the model is created by geometry preserving smoothing operations (c) .	19
Figure 2-5. Schematic of the aortic arch and aortic valve (AV) anatomy. The AV contains three leaflets/cusps (Left coronary leaflet (L), Right coronary leaflet (R), and None	

coronary leaflet (N)). (taken from University of Florida’s health webpage https://m.uflhealth.org).....	20
Figure 2-6. Example of plane selection for evaluation of aortic valve morphology in patient with normal aortic valve on ECG-gated multidetector CT. Note normal three cusps and aortic valve in diastolic phase (a, c) and opening in systolic phase (b, d) of double-oblique reconstruction images. (images are taken from Chun et al. 2008) ..	21
Figure 2-7. (a) Aortic valve model construction from the aortic valve annulus. The open and closed forms are created from the observation of valve shapes in literature (De Hart, Peters, et al., 2003; M.-C. Hsu et al., 2014; Wong et al., 2013). (b) Open and closed forms of the aortic valve super-imposed after performing LDDMM algorithm (Beg, Miller, Trounev, & Younes, 2005; Miller, Trounev, & Younes, 2002) to register and match surfaces between the two forms.	22
Figure 2-8. Velocity (a) and displacement (b) time variation of the valve compared with the inflow velocity profile. The opening time of the valve is defined as the time it takes to rises to the peak velocity and the closing phase is the time duration from peak velocity until end systole.	24
Figure 2-9. (a) Triangulated surface of an aorta immersed into the background Cartesian volume grid. The model includes the coronary sinus, aortic valve and three arch branches at the top. (b) Schematic of the stair step method for the immersed boundary treatment.	28
Figure 3-1 Representative example of transluminal contrast gradient for a stenosed artery. Luminal cross sections are sampled every 0.5 mm and plotted over the vessel length to obtain an axial variation of cross-sectional averaged attenuation (HU) (top	

figure). Bottom figure shows the axial and cross-sectional visualizations of lumen area by contrast agent. HU is the Hounsfield unit for the attenuation level. The lesion section is shown with an arrow. CT imaging is acquired using a 320-row detector CT scanner (AquilionTMOne -Toshiba Medical Systems Corporation, Otawara, Japan).....	34
Figure 3-2 Representative Arterial input function (AIF) measured in actual CCTA as well as the fitted function that is employed in the simulations in a human studies (A) and a canonical study (B). Part C is a schematic to illustrate the mechanism described in the paper: TCG is the transluminal (spatial) projection of the time profile of the concentration of the contrast agent and hence is driven by the coronary blood flow velocity (VCF).	39
Figure 3-3. Extraction of cross-sectional lumen area along the axial direction from the CFD simulation for the calculation of transluminal contrast gradients.	40
Figure 3-4 (a) An idealized 3-D model of the coronary artery for the normal (unstenosed) case where Q_n is referred to the normal (no stenosis) flow rate. (b) Model of the artery with a stenosis where Q_s is referred to the flow rate in the vessel with stenosis. (d) Computational meshes employed in the various segments of the model.	45
Figure 3-5. (A) Patient Specific velocity magnitude profile comparison between different grid levels for the cross sections shown in (B) in red planes in the main LAD after the stenosis. (B) Cross section plane used in (A). The 4 different grid levels are ‘Coarse’ with $\approx 2 \times 10^5$, ‘Normal’ with $\approx 3 \times 10^5$, ‘Fine’ with $\approx 4.55 \times 10^5$ and ‘FineR’ with $\approx 9.25 \times 10^5$ tetrahedral elements.	48

Figure 3-6 Pressure (a), velocity magnitude (b) and normalized contrast agent concentration (c) (C/C_{max}) for the $Q_n=50\text{ml/min}$ case with a 70% area constriction. (d) Velocity magnitude and streamlines in the stenosed region in idealized model. 49

Figure 3-7. Normalized transluminal attenuation profiles along the axial direction of main arterial segment for (a) steady flow with $Q_n=50(\text{ml/min})$ ($P_A = 3, P_B=0$ mmHg), (b) pulsatile flow with $Q_n=50(\text{ml/min})$ ($P_A = 3, P_B=2.7$ mmHg), (d) steady flow with $Q_n=69$ (ml/min) ($P_A=4.5, P_B=0$ mmHg), and (d) pulsatile flow with $Q_n=69$ (ml/min) ($P_A=4.5, P_B=4.05$ mmHg). (1) and (2) indicate the locations of bifurcations shown in Fig 3. The attenuation profiles along the stenosed section (between (1)-(2)) are fitted by the linear function; $a \cdot s + b$ and the slope a represents the normalized TCG (TCG*). All the results are for the idealized model at the peak of AIF and the percentage refers to different area stenosis levels..... 51

Figure 3-8. Correlation between (a) TCG and the inverse square of flow rate ($1/Q^2$) for steady flow, (b) for pulsatile flow, (b) TCG and the inverse square of bolus time, ($1/T_d^2$) for 70% stenosis and $Q_n=50$ ml/min, steady flow (d) TCG* and FFR_Q for pulsatile flow for the idealized model..... 52

Figure 3-9. (a) 3-D model of a patient specific coronary artery for the normal (unstenosed) case. (b) Model of the artery with 70% stenosis. (b) Computational meshes employed in the various segments of the model. 53

Figure 3-10. Patient specific computational results: Pressure (a), normalized contrast agent concentration (C/C_{max}) for the $Q_n=375$ ml/min case with a 70% area constriction. (b) and Velocity magnitude and streamlines in the stenosed region (c)

cross sectional plane in which velocity contour in (d) is shown. The segmentations	
S1-S4 are segments of the main LAD before each branch.	55
Figure 3-11. Patient specific normalized transluminal attenuation profiles along the axial	
direction of main arterial segment in LAD (steady flow) with PA=3 and PB=0	
mmHg. (a) Correlation between CFD calculation of flow rate and TAFE calculation	
of the flow rate in the no-stenosis (normal) and 70% area stenosis cases (b).	57
Figure 4-1 Retrospective evaluation of TAFE for nine canine models of ischemic heart	
disease were prepared and underwent CT imaging and microsphere measurements of	
myocardial blood flow (MBF). While TAFE correlated very well with CBF, it	
under-predicts the magnitude of CBF due to partial volume averaging (PVA) effects.	
(from Lardo et al. 2015).....	65
Figure 4-2. (a) Examination of partial volume averaging effects using computational	
models. A coronary artery model employed and planes of data extracted from	
model. (b) An example of the cross-sectional view of contrast concentration	
computed from our simulations where the arterial diameter is about 2 mm. A voxel	
grid of 0.5 mm is superposed on the plot and plot clearly shows how finite resolution	
affects the intensity across the lumen. (c) Comparison ideal (infinite resolution),	
actual (0.5 mm voxel), and corrected (using correction formula) attenuation profile.	
Note that after the PVA.....	67
Figure 4-3. Examples of arterial input function (AIF) at the ostium of the phantom	
sampled at every 2 seconds (a) and contrast concentration vs. the cumulative volume	
(b) the slope of this figure is known to be volumetric transluminal contrast gradient	
(TCG).....	69

Figure 4-4. Illustrative overview of the phantom experiment set up. The contrast is infused into the system by first flowing through the mixing chamber located on a magnetic stirrer to mimic the chambers of left and right ventricle (LV and RV) and the fully mixed solution enters the phantom.....	70
Figure 4-5 (a) Toshiba Aquilon One, 320 detector CT scanner used in the current study. (b): 3-D printed tapered phantom placed in the custom-built laser-cut holder. (c) Set up for flow phantom studies showing syringe pump, mixing chamber and magnetic stirrer and phantom.	72
Figure 4-6. Effect of filter kernel on attenuation. (a) Sectional images for 6 different filter kernels. (b) Sectional profiles for 6 different filter kernels. C. HU values for various kernels. D. Gaussian filter model for the kernel.	75
Figure 4-7. Flowchart of custom-written algorithm for segmentation of the phantom for each cross section of the phantom in a dynamic scan.....	77
Figure 4-8 . Illustration view of segmentation of straight phantom. Original phantom cross-section with the wall included (a). Background and wall level sets are assigned to have zero value and the center point is calculated shown with the blue star (b). ROI is chosen to be a 60 x 60 pixel from the center point (c). Edge of the lumen is defined using the Canny edge-detection method (d). The lumen of phantom is filled based on the edge detected (e). The filled area is corrected using active contour method (f).....	78
Figure 4-9. Transluminal contrast gradient curve for 5 consecutive time points where on the linear regression are shown in dashed lines including both original (in green) and the fit excluding the outlier data points shown with star markers (in blue).....	79

Figure 4-10. Contrast radial contour variation where the phantom wall and the air surrounding it is at 0 or negative (a). Contrast attenuation in HU vs. the radius of the phantom wall for 3 different cross-sections. The lumen radial profile is between radius values of 0 and 4 (b).	81
Figure 4-11. Computational models of straight (a) and tapered (b) phantom with the contrast concentration contour along the phantom at the mid y-plane at t=20 s.	83
Figure 4-12. Radial profile of the mean contrast concentration for straight (a) and tapered (b) phantom with two values of $Sc=1$ and 1000.	85
Figure 4-13. Cross-sectional average concentration of contrast agent along the axial direction of a pre-mixed tapered phantom experiment (a) and in a representative phantom experiment with flow (b). The blue dots show a drop in concentration despite the stationary flow in the phantom. The red dots are the corrected using the α correction factor determined from (c) where the red line is the fitted polynomial in Eq. 4-8b.....	87
Figure 4-14. Comparison of TAFE Estimated flowrate with the true pump flow rate for straight (a) and tapered (b) phantoms. The result significantly improve after the corrections are applied.	91
Figure 4-15. Examples of ‘rough’ and non-uniform surfaces of the inner wall for different locations along the phantom for (a) straight phantom and (b) tapered phantom.	92
Figure 5-1. Schematic of the Aortic root with the coronary sinus, aortic valve leaflets and sinutubular junction defined. This schematic is taken from University of Florida’s health webpage at: https://m.ufhealth.org	94

Figure 5-2. Clinical representative case with (a) Descending aorta ROI cross-sections defined at the sure-start process where 2D images of the heart including the descending aorta is taken. The last image (right most image) is the volume image with the peak contrast value associated. (b) Time profile of contrast or AIF is then created measuring the mean contrast attenuation in HU at the ROI blue regions where the last point belongs to the volume image after the scanner is triggered. (c) Electrocardiogram (ECG) information of the patient while scanning including the HR. The scanning is done through a ECG gated process to prevent motion artifacts where the heart has the least motion in the R-R interval. The yellow bar (or blue shaded region) represents the phase that the image has been acquired. 98

Figure 5-3 Steps involved in segmentation and creation of model-ready geometry.

Dynamic region growing methodology was used to segment the aorta (a). The 3D geometry of the segmented artery is constructed using volume rendering (b). The rendered geometry is then smoothed using property preserving smoothing operations (c). The CFD ready model of aorta including the simple inflow tube along with the valve inserted at the aortic orifice. The snapshot is taken at end diastole. 101

Figure 5-4. Velocity (a) and displacement (b) time variation of the valve compared with the velocity inflow profile. The opening time of the valve is defined as the time it takes to rise to the peak velocity and the closing phase is the time duration where the velocity drop begins in the inflow velocity until end systole. 104

Figure 5-5. (a) *In-vitro* measurements of valve leaflet velocity at 4 different positions on the sinus cusp. Similar trend of opening and closing time is observed. (Bellhouse & Talbot, 1969) (b) *In-vivo* measurements of the aortic valve measurements in systole

via echocardiographic imaging in 3 groups of patients with valve dysfunction after surgical valve preservations. Each group's valve displacement includes a faster raise in opening time and a slower closing time interval. (Leyh et al., 1999).....	105
Figure 5-6. The open formed of the valve is morphed to the closed form using LDDMM. The valve motion is then prescribed between these two reference configurations. A sample of sequence of valve movement is shown here.	107
Figure 5-7. (a) Immersed computational model and (b) reference planes defined for presenting velocity vectors and contrast contour at the inlet and (c) time-averaged normal projected velocity, vorticity and contrast concentration and (d) Arterial Input Function planes at the coronary ostium/ascending aorta in the X-plane (green) and Y-Plane (blue) and the normal to the descending aorta (red).	109
Figure 5-8 Velocity vectors colored with magnitude of velocity in the second cardiac cycle shown at the ascending aorta at two different reference planes of X-plane (a-e) and Y-plane(f-j) for 5 different time points of $t = T_o/2 = 1.06$ s, completely opened valve ($t = T_o = 1.12$ s), $t = (T_o + T_c)/2 = 1.33$ s, end systole ($t = T_o + T_c = 1.54$ s) and end diastole at $t = T = 2$ s).	111
Figure 5-9 Aortic vortex dynamics and breakdown during the cardiac systole. Vortex structures are visualized by the Q criterion (where the second invariant of vorticity tensor is greater than zero i.e. $Q > 0$ (Haller, 2005; Wu et al., 2005)) colored by velocity magnitude and the numbers indicate non-dimensional times.	112
Figure 5-10. Time-averaged contours of velocity at selected cross sections at different orientation of the aortic arch. Medial and Lateral walls are defined to demonstrate the tortuous nature of the aortic arch anatomy.....	114

Figure 5-11. Time-averaged (cycles 2-5) contours of normal projected velocity for different normal to the flow cross-sections defined in Figure 5-7c. The lateral and medial walls denote the outer and inner walls of the aorta, respectively.	115
Figure 5-12. Time-averaged (cycles 2-5) contours of normal projected vorticity for different normal to the flow cross-sections defined in Figure 5-7c. The lateral and medial walls denote the outer and inner walls of the aorta, respectively.	116
Figure 5-13. Cross sectional ROI's defined at the X-plane (a) and Y-plane (b) in ascending aorta and the normal plane (c) at the descending aorta. The reference definitions are shown in Figure 5-7d. The small and large circles are for two different sizes of ROI's to reflect the coronary ostium (small circle) and about $\frac{3}{4}$ of the size of descending aorta to calculate the cross sectional average contrast attenuation.....	117
Figure 5-14. Time profile of normalized cross-sectional averaged contrast concentration at ascending and descending aorta at $\Delta t = 0.01$ s for the large ROI (a) and small ROI (b) defined in Figure 5-13 for $Sc=1000$. Sampled AIF shown in (a) for $\Delta t = 0.5$ s (c) and $\Delta t = 1$ s (d) for $Sc=1000$.The green dashed line represents the inlet contrast concentration profile. Ascending aorta concentration is calculated by: $C_{Asc} = C_{avg} - Xp + C_{avg} - Yp2$	118
Figure 5-15. Comparison of time profile of normalized cross-sectional averaged contrast concentration at ascending and descending aorta for $Sc=1$ (solid lines) and $Sc=1000$ (dashed lines). The green solid line is the inlet contrast time profile.	119
Figure 5-16. Contours of time-accumulated (cycles 2-5) contrast concentration are plotted (for slices S_1 - S_{11} defined in Figure 5-7c) for $Sc=1$ (a) and $Sc=1000$ (b).....	120

Figure 5-17. Tangential to plane time-averaged streamlines at each cross-section defined in Figure 5-7c where the background contour levels are time-averaged normal projected velocity. This figure demonstrates that there is no Dean-type flow pattern present in the aortic arch in contrary to the cases studied in Mori et al. where the streamlines are drawn in planes denoted with k and the locations for different k is shown on the (l), Feintuch et al. where the planar velocity vectors are plotted at the two reference planes 3 and 4 defined on the corresponding aorta (m), Shahcheraghi et al. where the secondary flow pattern are plotted for the defined cross-sections (n) and Kim et al. where the streamlines are shown for the location indicated in the figure with different Womersely numbers, $\alpha(o)$ 122

Figure 5-18. Streamlines through the aortic arch colored by velocity magnitude at three different points in early systole at $t=1.06$ s (a), mid systole at $t=1.12$ s (b) and late systole at $t=1.33$ s (c). Streamlines in available literature in the aortic arch in the computational work of Numata et al. with a patient with the CABG procedure done at peak systole (d) 4D PcMRI visualization of streamline above the valve plane level through the whole aorta in Markl et al. for a healthy patient (e) and PcMRI..... 123

Figure 5-19. AIF at descending aorta with sampling rate of $\Delta t = 0.5$ s where the starting point is shifted by 0.1 second to demonstrate that depending on the time point in cardiac cycle, the AIF slope can vary significantly. 126

Figure 5-20.(a) Mean error between the two AIF curves at ascending and descending aorta. The minimum in this plot is defined as the transport with very close values for $Sc=1$ and 1000. The concave part of the plot is zoomed in to see the difference in the curve for the two Sc numbers. (b) Pathline calculated between the first slice (S_1) and

last slice (S_{11}) shown in Figure 5-7c where the transient time is the time that takes for a fluid particle to travel on the pathline. (c) Centerline defined between each slice on the aortic arch.	129
Figure 5-21. (a) Schematic of velocity profile with pulsatile (Womersely flow) characteristic. The maximum flow V_{\max} is much higher than the mean flow velocity and is transporting the contrast as a faster velocity. Radial time-averaged normal velocity show similar radial profile as the schematic in (a) and are shown for Slices 1 to 5 in (b) and 6-11 in (c).....	130
Figure 6-1. Steps involved in TAFE analysis with tracking the vessel and determining the centerline (a) editing the lumen wall and finding the TCG along the centerline of each vessel with its branches(b) and measuring AIF at the descending aorta (c). Images taken from (Lardo, Rahsepar, Seo, Eslami, Korley, Kishi, et al., 2015)....	137
Figure 6-2. Two representative case of CMR perfusion cases for a patient with severe LCX disease (a) and patient with no significant CAD (b).....	138

CHAPTER 1: INTRODUCTION

1.1. MOTIVATION AND BACKGROUND

1.1.1. Trends in Coronary Heart Disease (CHD) and Diagnostics

1.1.1.1. Epidemiology of CHD

Cardiovascular disease affects 17 million Americans and is the leading cause of death among men and women in the United States with a prevalence of 9.1% and 7.0%, respectively and resulting in approximately 400,000 deaths annually. In 2007, CHD was responsible for ≈ 1 of every 6 deaths in United States. While advances in medical and invasive therapies for CHD have helped to decrease deaths from cardiovascular disease over the past several decades, the estimated indirect and direct cost of CHD is estimated to triple over the next two decades from \$273 to \$881 billion. A large portion of this cost is accounted for by invasive procedures and therapies for CHD including 1,313,000 percutaneous coronary intervention (PCI) procedures; 448,000 inpatient bypass procedures; and 1,115,000 invasive cardiac catheterizations (ICA) in 2006 alone (Roger et al., 2011). Given the cost of invasive procedures, it is necessary to improve current standard-of-care by advanced, improved and economical non-invasive diagnostic methods consolidating multi-disciplinary fields such as medicine, imaging and engineering.

1.1.1.2. Current Standard CHD Diagnosis

For several decades invasive coronary angiography (ICA) has been the standard diagnosis test for the assessment of CHD. This is a cardiac catheterization process where, a catheter is inserted close to the artery of interest and a radio-dense dye injected into the artery in order to display the entire coronary tree of interest, while avoiding artifacts and

vessel overlaps. However, while coronary lesion severity estimation is generally quite accurate with this procedure, accurately detection of the functional severity of CHD disease lesion is not guaranteed (Staniak et al., 2014).

It is well established that fractional flow reserve (FFR) measurements made during ICA improve cardiovascular outcomes and decrease costs when used to make revascularization decision(A. Berger, Botman, & MacCarthy, 2005; Pijls et al., 1996; Tonino et al., 2009). Until recently, the diagnosis of CHD was not possible without performing an ICA. However, with developments in relevant technologies and advancements in imaging, non-invasive diagnostic tools including ECG stress testing, stress echocardiography, advanced imaging nuclear imaging, cardiac Magnetic Resonance Imaging (MRI) and cardiac Computed Tomography Angiography (CTA) (Blankstein, 2012) have been developed. However stress testing with nuclear imaging tends to under or overestimate the presence of ischemia, especially in patients with multi-vessel coronary disease (Melikian et al., 2010).

While MRI imaging modality has been used for various cardiac diseases, advances in multi-detector computed tomography (CT) technology now allows noninvasive access to several important factors in regards to coronary event risk: the overall coronary arterial plaque burden, the severity of coronary arterial stenoses, the location and consistency of plaque, and plaque configuration (Motoyama et al., 2007, 2009). Coronary CTA is a diagnostic procedure to visualize the artery and specifically the lumen area of coronary arteries. The advent of high resolution multi-detector CTA (MDCTA) coupled with prospective ECG gating allows for the image scanning of the entire heart thereby enabling high-resolution assessment of the morphological details of the main coronary vessels (Becker, Ohnesorge, Schoepf, & Reiser, 2000). In order to enhance the boundaries of the lumen, intravenous iodinated contrast agent is injected in to the patient. To minimize the radiation exposure and more accurately determine the optimal scan

delay after the contrast agent administration in patients, the temporal variation of the contrast agent bolus (profile) is tracked at a reference location (typically at the descending aorta); the CT image is acquired when this bolus reached maximum intensity (Vincent Ho & Reddy, 2010). An example of MDCTA image for coronary artery with a lesion is shown in

Figure 1-1, where the lumen is represented by gray area and HU is the Hounsfield units, which measures the level of attenuation of the X-ray beam. While anatomic information on CHD by CT is important and has been shown to correlate with patient outcomes (Hulten, Carbonaro, Petrillo, Mitchell, & Villines, 2011; Min et al., 2007), there are other important determinants of patient outcome with CHD including the degree of epicardial blood flow reduction and the extent and severity of myocardial ischemia. CT allows the assessment of coronary anatomy, coronary blood flow, and myocardial perfusion and thus, is uniquely positioned to acquire comprehensive information to guide the evaluation and management of patients with suspected CHD.

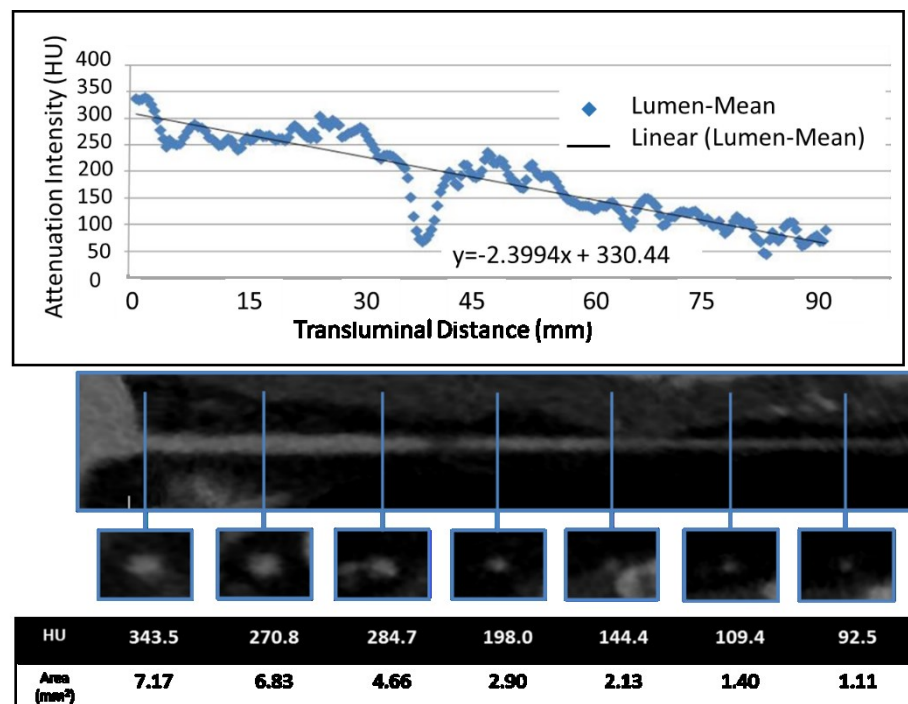


Figure 1-1 Representative example of transluminal contrast gradient for a stenosed artery. Luminal cross sections are sampled every 0.5 mm and plotted over the vessel length to obtain an axial variation of cross-sectional averaged attenuation (HU) (top figure). Bottom figure shows the axial and cross-sectional visualizations of lumen area by contrast agent. HU is the Hounsfield unit for the attenuation level. The lesion section is shown with an arrow. CT imaging is acquired using a 320-row detector CT scanner (AquilionTMOne -Toshiba Medical Systems Corporation, Otawara, Japan).

1.1.2. Trends in Computing

As mentioned before, creating an accurate and cost-effective non-invasive diagnosis of CHD is the ultimate goal. With faster and cheaper computations and rapid development of computing tools and its favorable trend (Moore's Law shown by (Schaller, 1997)), it is possible to counteract the negative trends in CHD. The computational cost of a typical flow simulation in an aortic arch employing high spatial resolution of about 15 million grid points and high temporal resolution of about 10,000 steps (roughly 1 cardiac cycle) is of an order of ExaFLOPS while the current capability of supercomputers are in the range of PetaFLOPS requiring long computational time that is clinically impractical. However, Moore's law predicts Exascale computing is very likely plausible in about a decade from now at a moderate computational cost (Rajat Mittal et al., 2015). In fact, these trends have already been observed with recent rising of GPUs and MICs where supercomputing performances on a desktop PC can be delivered which is mandated in clinical diagnosis and real-time therapy.

In fact, just recently, some groups including ours have made great progress in the simulation based therapeutic approach such as detecting thrombosis formation in the LV after myocardial infarction (Seo, Abd, George, & Mittal, 2016), optimization of Fontan surgical procedure (Kung et al., 2013; Long, Hsu, Bazilevs, Feinstein, & Marsen, 2012) and Kawasaki disease treatment (Sengupta et al., 2012) and the most relevant to present study, estimating FFR by the use of CFD developed by *Heartflow* Inc. (C. A. Taylor, Fonte, & Min, 2013) which will be described in more details later in this Chapter. In addition, computational tools are capable of assisting the clinicians to understand and analyze the physiological flow in healthy cardiovascular and diseased cardiovascular systems. For example, fundamental questions such as effect of trabeculae and papillary muscles on the hemodynamics in the left ventricle (Vedula, Seo, Lardo, & Mittal, 2016) or the role of arterial geometry in growth of vascular aneurysms (Hoi et al., 2004).

Therefore, it is important to appreciate that computational-based modeling coupled with advanced medical imaging provides in the promise of economical and reliable diagnosis and treatment of diseases such as CHD. Hence, it is essential to develop robust platforms and computational frameworks and combined with the appropriate and relevant diagnostic tools, progress towards making simulation-based diagnosis and treatment of cardiovascular diseases a viable option.

1.2. LITERATURE REVIEW

1.2.1. Existing Coronary Flow Assessment and Limitations

Myocardial Perfusion Assessment – In the past several years, there are few ongoing studies by our group and others to develop methods to measure coronary and myocardial physiology from cardiac CT images. The study of George et al.(George et al., 2007) first

validated static myocardial CT perfusion imaging (CTP) in animal model coronary stenosis where qualitative correlation with the microsphere myocardial blood flow (MBF) were demonstrated. CPT has been further validated in patients with suspected coronary artery diseases, and compared with radionuclide myocardial perfusion imaging, it can detect myocardial ischemia with good diagnostic accuracy (Blankstein et al., 2009; Cury et al., 2011; George et al., 2009). However, when compared to FFR, quantitative CTP imaging in its current form has limited sensitivity (79%) and negative predictive value (79%) (Ko et al., 2012). In addition to CTP based attempts to measure MBF, other imaging modalities such as phase contrast MR (CMR) perfusion have been used to quantify the coronary blood flow. Using CMR, Hsu et al. (L.-Y. Hsu, Groves, Aletras, Kellman, & Arai, 2012) have shown qualitative colored map comparison with MBF in canine studies and have later verified it in clinical trials. However, it appears that a qualitative approach to myocardial CTP along with CMR quantification of coronary blood flow has similar limitations as other non-invasive stress testing modalities in the ability to attribute decreases in myocardial perfusion to the physiologic significance of specific stenoses.

Coronary Flow Assessment – As mentioned in the previous section, recently, Min et al. and Taylor et al. (Min et al., 2012; C. A. Taylor et al., 2013) have utilized computational fluid dynamics for determining FFR from CT angiography is a technique called FFR_{CT} developed by *HeartFlow* Inc. In this approach, 3D models of the coronary vasculature including the ascending aorta, are developed from CT angiograms. Blood flow is simulated via CFD and pressure is estimated in the major coronary vessels. Once the pressure in the arteries is computed, FFR can be obtained directly from the CFD results. One positive feature of this idea is that FFR can, in-principle, be obtained non-invasively from a standard

CTA exam. While promising, this technique has shortcomings of its own such as limited diagnosis accuracy of 73%, inability to provide a real-time diagnosis due to its extremely high computational an analysis time (2-12 hours), the requirement of complex modeling and supercomputer processing. The method also depends highly on the image quality and determining lesion morphology with calcification, stents, and motion limiting coronary lesion visualization (Koo et al., 2011; Min et al., 2012).

Thus, methods that are independent of lesion morphology and make measurements of coronary physiology from CT will have significant advantages of the latter. For instance, recent studies have raised the interesting possibility that the data from MDCTA might contain some information on the functional severity of the lesion. In particular, studies (Choi et al., 2011, 2012; Chow et al., 2011; Nakanishi & Budoff, 2014; Stuijzand et al., 2014) have noted a continuous attenuation of contrast agent concentration along the axial direction and this attenuation gradient (termed as the transluminal contrast gradient; TCG) appears to correlate with the severity of the stenotic lesion (Choi et al., 2011, 2012; Chow et al., 2011). Choi et al. also found that adding the attenuation gradient to the interpretation of coronary CTA improved classification of coronary artery stenosis severity, especially in severely calcified lesions. While these studies demonstrate that physiologic information could be present in the attenuation gradients noted on CCTA, the underlying mechanism of these gradients are not well understood. Furthermore, attempts at correlating TCG with well-established, indices of functional significance such as fractional flow reserve (FFR) have not been encouraging (Stuijzand et al., 2014; Wong et al., 2013; M. Zheng et al., 2015) and it was not clear if this lack of correlation reflects an inherent disconnect between physiologic conditions and TCG, or the presence of imaging artifacts (i.e. resolution), or

inadequate control of conditions that effect the correlation between hemodynamics and TCG. This poor relationship between TCG and FFR suggests that TCG may be too simplistic to represent the complex interaction between coronary flow, pressure and stenosis. Further, the lack of proper controls for temporal dispersion effects in these studies resulted in variability and the inability to extract quantitative functional metrics of coronary obstruction.

In parallel with discovery of TCG, just recently, an image-based methodology called time-of-flight (TOF) has been introduced where sequential scanning mode is utilized to calculate vascular flow velocity. However, the work here done requires a dynamic CT imaging which introduced unacceptable radiation dose for use in patients. In addition, the mentioned study merely describes the estimation of CBF from an imaging and radiology standpoint and the method has not been verified in any arterial system with lesion or obstruction and lacks the understanding and explanation of the hemodynamics and physiological significance of stenotic lesions (Prevrhal et al., 2011; Barfett et al., 2014; Korporeal, et al., 2016).

Thus, there is a need for a study that can delineate the confounding effects of physiology and imaging on TCG. Such delineation is difficult to accomplish via *in-vivo* studies firstly because the two effects (physiology and imaging) cannot be separated and secondly, imaging does not by itself provide all the information required (velocity, pressure, contrast agent distribution etc.) for determining the physiological mechanisms of TCG generation. Computational fluid dynamics is a great tool, which it is capable of studying the hemodynamics of blood flow in coronary arteries and coupled with contrast dispersion questions on mechanism of TAG can be answered.

1.3. CURRENT OBJECTIVES

In view of the limitations in the previous research efforts and with an eventual goal of developing a non-invasive, accurate and real-time methodology to estimate coronary flow velocity and provide physiologically significant information about a lesion, the present research aims to achieve the following objectives:

Objective 1: Study the flow physics associated with TCG and explore methods for estimating coronary flow velocity from transluminal contrast dispersion patterns obtained from CT angiography.

The first objective here is to determine physical mechanisms (flow patterns, contrast dispersion physics) that might be responsible for the generation of transluminal contrast gradients. An additional objective is to use our understanding of the physical mechanisms to develop methods that can extract coronary flow velocity using the information in the transc coronary contrast patterns detected by CT imaging. The novel method developed in this work utilizes the already available information from CT images in order to estimate the blood flow. We model contrast dispersion with a convection-diffusion equation and analytically solve for the average flow via our formulation – Transluminal Attenuation Flow Encoding or TAFE. This formulation is developed assuming that the contrast dispersion is convection dominant as well as the flow being unidirectional and one dimensional in the direction of axial direction of the vessel. We validate TAFE against canonical and patient specific models of coronary arteries for two steady and pulsatile pressure boundary conditions. Canonical stenoses are created to mimic the lesion in vessels the spatial gradient of contrast along the vessel, also known as transluminal contrast gradient (TCG) is measured and compared against the normal vessel without any stenosis.

The formulation is also derived for a branched network within a steady flow environment. Finally, the TAFE estimation of flow rate for the branched network is compared against CFD calculated flowrate in the patient specific models.

Objective 2: Validate and modify the TAFE formulation based on preclinical and phantom studies

Subsequent to the development of a non-invasive methodology (called TAFE) for estimating the flow rate from TCG and validating it against CFD models, the next step is to validate the formulation in more realistic settings. Our collaborators have conducted tests of this method in a preclinical setting with canine models. These preclinical comparison that compare total myocardial blood flow (MBF) estimated by TAFE against microsphere measurements of MBF indicate that although the absolute values are underestimated by TAFE, the results show very good correlation with the microsphere measurements. The objective of the current research is explore the factors responsible for the under-prediction in CT compatible phantoms that incorporate many of the imaging-related errors but still provide high degree of experimental control. The dynamic CT images of phantoms are analyzed using a custom written script in MATLAB and several segmentation methods has been applied to optimize the measured cross-sectional attenuation of contrast. In the formulation of TAFE, radial variation of contrast was neglected, however, due to different filtering kernels applied when the CT images are reconstructed as well as fluid dynamics effects, the radial variation is apparent from the CT images. In addition, imaging artifacts such as partial volume effect particularly in tapered vessels are investigated. The previously developed TAFE formulation is then modified

based on the corrections found due to radial variation of contrast as well as imaging artifacts.

Objective 3: Examine AIF dispersion in the aortic arch

The time profile of contrast at the coronary ostium (i.e. the arterial input function or AIF) is a key component of TAFE-based estimation of coronary flow. However, in the clinical setting, AIF is only available at the descending aorta location, and this is assumed to have the same shape and profile as the coronary ostium (or ascending aorta) in the current developed methodology. To test the validity of this assumption, a patient specific of the whole aortic model including the coronary sinus, aortic valve and the arch branches have been created to study the contrast dispersion through the aorta. Realistic pulsatile flow as well as time changing contrast profile is input to the system and the AIF profiles are compared at the ascending and descending levels. In addition, effect of molecular diffusivity in the form of Schmidt number is investigated on the contrast dispersion through the aorta to account for different contrast agents with different molecular diffusivity values. Based on this study, we make conclusions about the validity of using the descending aorta AIF as a surrogate for the AIF at the coronary ostium in TAFE.

CHAPTER 2: COMPUTATIONAL MODELING FOR FLOW AND CONTRAST DISPERSION IN CARDIOVASCULAR FLOWS

In the current research, the flow and dispersion patterns in a wide variety of cardiovascular configurations have to be modeled. These include:

- Simple straight vessels corresponding to CT compatible phantom experiments (see Chapter 4).
- Canonical curved, single and branching vessels (see Chapter 3).
- Patient derived branching coronary vessels (see Chapter 3).
- Patient-derived model of the aorta including aortic valves (see Chapter 5).

Furthermore, there are wide range of flow conditions and features that need to be incorporated into the various simulations; these include:

- Range of Reynolds number from $O(10)$ in the smaller vessels to $O(1000)$ in the aorta.
- Steady and pulsatile flow.
- Laminar and transitional flow.
- Modeling of scalar transport and mixing.
- Moving boundaries in the case of the aortic valve.

The scope of this computational investigation makes it difficult to accomplish all the simulations with a single solver and we have therefore employed multiple simulation and modeling tools for our study.

There are multiple steps involved for the creation of the computational models of patient-specific vascular flow. Figure 2-1. illustrates the major steps for this procedure; the process starts with extracting patient-specific anatomical data for the vessel or vessel network of interest via appropriate in-vivo imaging modalities such as Computed Tomography Angiography (CTA) , Phase-Contrast Magnetic Resonance Imaging (PCMRI) or Echocardiography. In the current research CTA has been the imaging modality of choice. These 4D medical images are then processed through a series of steps such as image edge enhancement, filtering, segmentation, vessel probing and registration to generate the geometrical model for the simulation.

In this work two different vascular network are modeled – left coronary artery (LCA) and the aorta (including the aortic annulus, ascending aorta, aortic arch (AA) and the proximal descending aorta. While all the vessels modeled here undergo dynamic motion during the cardiac cycle, this motion is not included in our modeling and all models are assumed to be stationary. It is expected that the effect of this motion on the flow and contrast dispersion is small. On the other hand in the modeling of the flow/contrast dispersion in the aorta, the movement of the aortic valve leaflets cannot be ignored and the dynamic motion of this valve is incorporated in our model.

Once the 3D stationary or dynamic models of the vessel in question is created, the flow and contrast agent dispersion can be solved computationally using the Navier-Stokes equations for incompressible flow and convection-diffusion for modeling the contrast respectively. Two different flow solvers are employed in this work depending on the nature of the problem. The blood flow in LCA was modeled using ANSYS-CFX which is a commercial finite volume solver appropriate for stationary boundaries and for branching

vessel networks. The solver employed for the aorta is based on the immersed boundary (IB) based solver called ViCar3D, which is described in Mittal et al. (R. Mittal et al., 2008; Seo & Mittal, 2011). This solver is well suited for simulation of flow in configurations that involve geometrically complicated, stationary as well as moving boundaries (such as the aortic valve) and is also appropriate for simulation of high Reynolds number flows that are encountered in the large vessels such as the aorta. The following sections will address each step of framework in details.

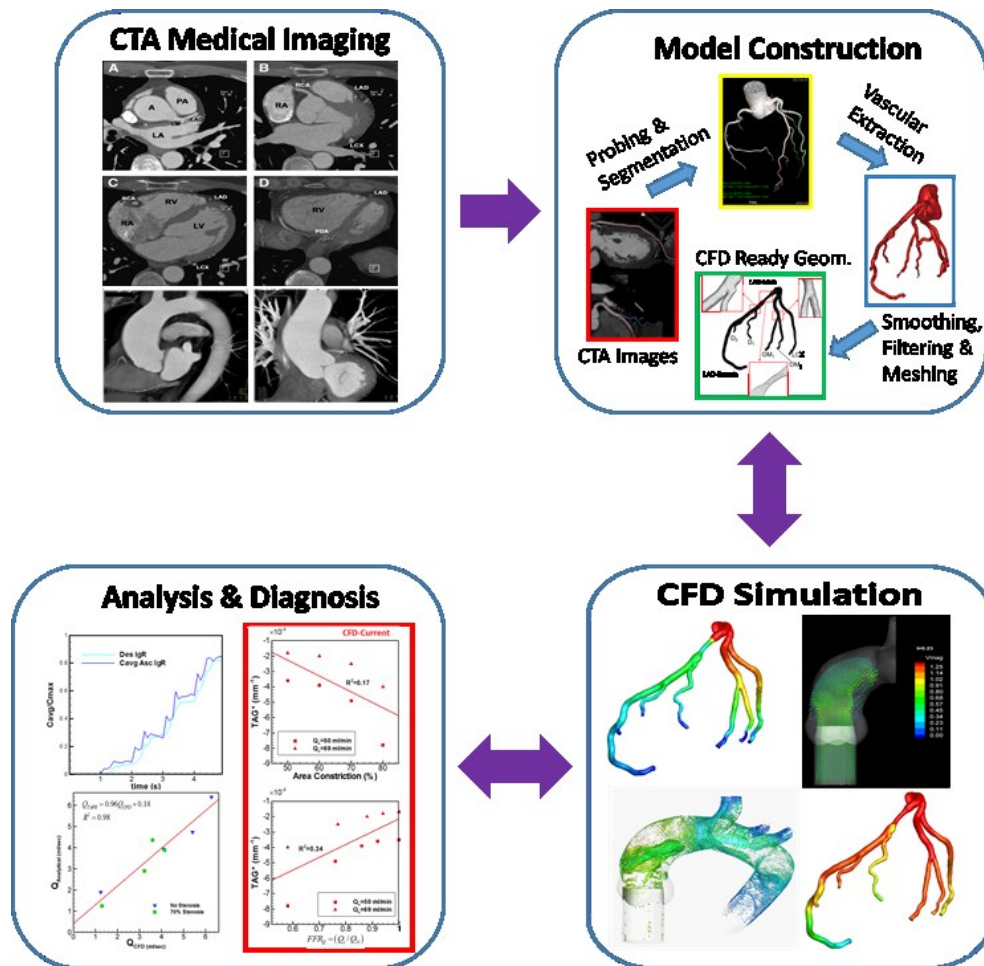


Figure 2-1. Framework for image-based patient-specific computational modeling

2.1. MEDICAL IMAGING – COMPUTED TOMOGRAPHY ANGIOGRAPHY (CTA)

There are in principle, a number of non-invasive cardiac imaging such as Echocardiograph, Nuclear Imaging, MRI, CT Angiography etc. (Figure 2-2). However, the key for a patient-specific vascular modeling is to choose an imaging modality that has the most appropriate best spatio-temporal resolution. Imaging vascular network requires very good spatial resolution and since the myocardium moves during the cardiac cycle, the challenge is to capture the whole heart within one heartbeat. Although Echocardiography provides the best temporal resolution (30-100 Hz) it lacks the spatial resolution needed the development of patient-specific vascular models. Therefore, advanced imaging modalities which offer enhanced spatial resolution such as MRI and CT angiography are required. In these imaging modalities, an ECG gated methodology is used to control the dynamic motion of the heart and synchronize the imaging with the heart dynamics to have the least motion artifacts (Desjardins & Kazerooni, 2004). With an in-plane resolution of 1.5mm x 1.5mm and a more limited through-plane resolution of 8 mm, Cardiac MRI is capable of higher temporal resolution (30-50 msec). On the other hand, Cardiac CT has a high isotropic spatial resolution on the sub-millimeter scale of 0.5 mm, while its temporal resolution depending on the scanner type (Helical, 64,128 and 256 and 320 multidetector) varies between 50 to 300 msec. The quality of these images can be furthered enhanced and improved by angiography (injection of contrast to the patient); MR Angiography (MRA) is excellent for soft-tissue enhancement, however, the vessels' lumen is substantially better captured by CT Angiography (CTA) (Sun, 2013) (See Figure 2-2). Furthermore, it is important to note that even with the cutting-edge imaging techniques and technologies, the

temporal and spatial resolution provided are far less than the required resolution for which the flow is solved in the computational models. Therefore appropriate spatial and temporal interpolations should be employed to create a CFD-ready model.




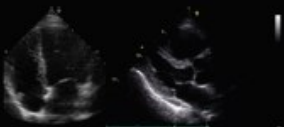

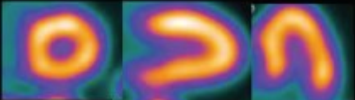

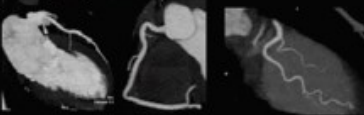
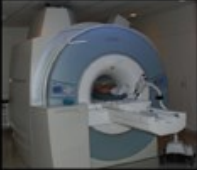
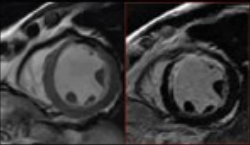
TEST / IMAGING MODALITY	EXAMPLE OF IMAGES / DATA PROVIDED
EXERCISE TREADMILL TESTING 	Electrocardiogram showing electrical activity of the heart during rest / exercise 
ECHOCARDIOGRAM 	Images of heart muscle function and valves 
NUCLEAR CAMERA 	Images showing bloodflow to the heart muscle 
CARDIAC CT 	Images showing arteries that supply blood to the heart muscle 
CARDIAC MRI 	Images showing the heart muscle function / scar related to disease 

Figure 2-2. Comparison of different non-invasive imaging modalities. (Figure taken from (Blankstein, 2012))

2.2. MODEL CONSTRUCTION

2.2.1. Vessel segmentation

In this work, two different software and methodologies are employed for vessel segmentation. The coronary artery network has been segmented using the research module provided to us by Toshiba and the aorta was segmented using a commercial software, Mimics, *Materialise Inc.*

2.2.1.1. Coronary Arteries

The coronary artery is segmented using a custom software analysis tool (Toshiba Medical Systems, Otawara, Japan). Figure 2-3 illustrates the steps involved in creating a CFD-ready model from the imaging data. This software enables a semi-automatic detection of coronary walls and lumen and based on the image quality, the segmentation can be corrected centerline and lumen adjustment using the so called “active snake method” (Kass, Witkin, & Terzopoulos, 1988) (Figure 2-3a). Based on the maximum contrast attenuation level for the specific patient, contrast level thresholds for the lumen and the wall are set and the software (semi-automatically) is able to calculate the cross-sectional area of the vessel. With the area and centerline detected, a 3D image of vessel can be constructed (Figure 2-3b). The 3D DICOM model can then be extracted as a STereoLithography (STL) format (Figure 2-3c). Once the 3D geometry is available, the user needs to “clean up” the vessel. Figure 2-3d represents the final version of the LCA with its typical branches labeled after elimination of the aortic sinus, outlet and inlet adjustments, and smoothing of the lumen. 3-Matic Materialise Inc. was used to smoothen the surfaces and produce the final surface mesh.

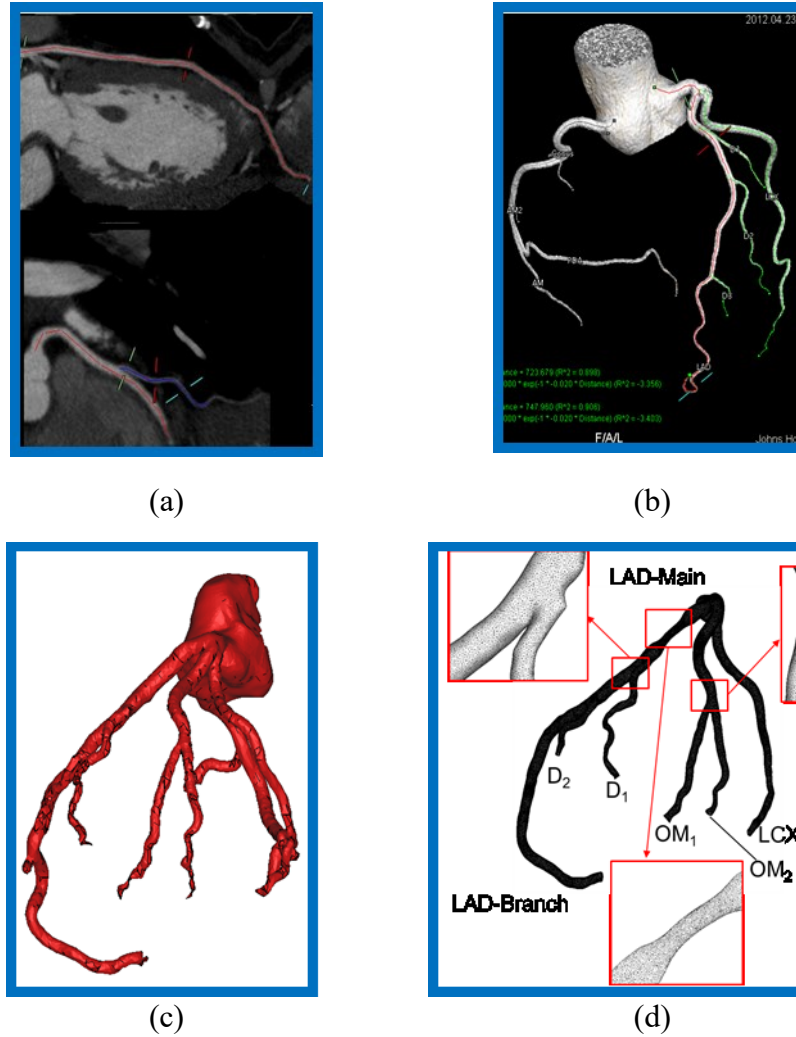


Figure 2-3. Steps involved in construction of the CFD-ready geometry. Coronary artery probing and segmentation for each plane (a). 3D model construction based on the centerline and cross-sectional area detection (b). STL extraction of the vessel from the DICOM files. (d) Final geometry after “cleaning up” the raw output into STL format.

2.2.1.2. Aorta and Aortic Arch

Imaging the aorta, including all the sections such as ascending aorta, branches on the arch and descending aorta, requires a ECG-gated 3D volume scan so that the moving artery can be captured and constructed with minimal motion artifacts. Similar to the coronary arteries, the volume images during CTA are then subjected to a series of filtering operations

to reduce the noise and enhance the contrast (Lardo, Rahsepar, Seo, Eslami, Korley, George, et al., 2015) until the lumen is clearly distinguished from the tissue wall. Image segmentation is performed subsequently to extract the region of interest (i.e the aortic arch) using a commercial software (Mimics, *Materialise Inc*).

Depending on the modality and the image quality, there are many options for automating and optimizing image segmentation of different anatomical body parts. In cardiac imaging also, various methodologies have been investigated- from simple methods such as thresholding and histogram-based methods to region growing, parametric active contours (snake) and level set. (Gao, Huang, & Zhang, 2011; McInerney & Terzopoulos, 1995; Peyrat et al., 2008; Shen, Sundar, Xue, Fan, & Litt, 2005; Y. Zheng et al., 2010). In this work dynamic region growing was used to segment the aortic arch using a thresholding level of 700 HU. The segmented region was then edited manually to ensure correct segmentation of the vessel. Figure 2-4 demonstrates the steps used to segment and finalize the CFD-ready patient-specific model.

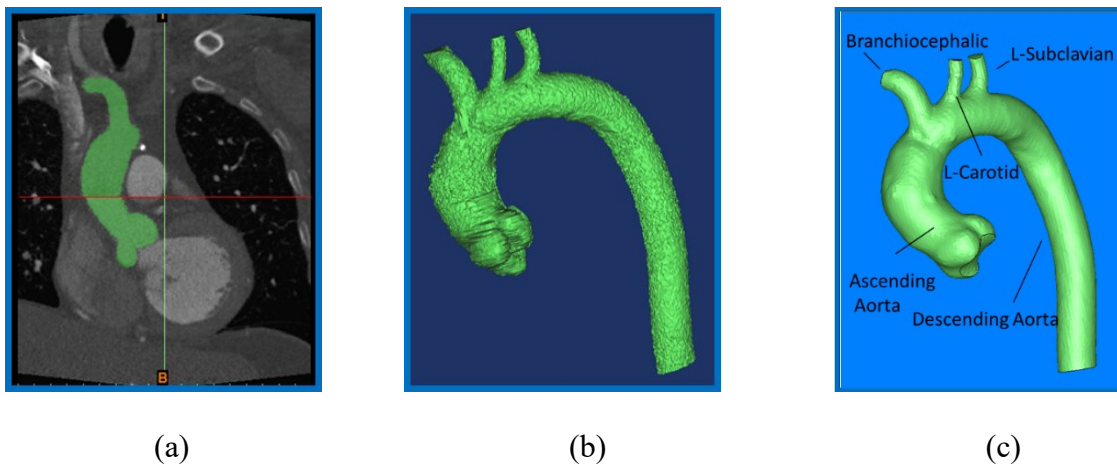


Figure 2-4. Steps involved in segmentation and creation of model-ready geometry. A dynamic “region growing” methodology was used to segment the aorta (a). The 3D model of the

segmented artery is constructed using volume rendering (b). The final version of the model is created by geometry preserving smoothing operations (c)

2.2.1.3. Aortic valve (AV) modeling

The heart valves are passive structures that ensure mostly unidirectional flow between the four chambers of the heart and the connecting 3 main arteries (aorta, right and left pulmonary arteries) by opening and closing in response to the differences in pressure and hemodynamic forcing. Connecting the left ventricular tract to the ascending aorta, the aortic valve placed at the aortic root contains three leaflets/cusps (left coronary leaflet (L), right coronary leaflet (R), and non-coronary leaflet (N)). The root extends from the basal ring to the sinotubular junction as it builds the supporting structure for the leaflets (See Figure 2-5). The leaflets are fixed to the root where they are hinged to open and close on the aortic sinus and can be modeled as semi-lunar pockets (M.-C. Hsu, Kamensky, Bazilevs, Sacks, & Hughes, 2014; Ionasec et al., 2010).

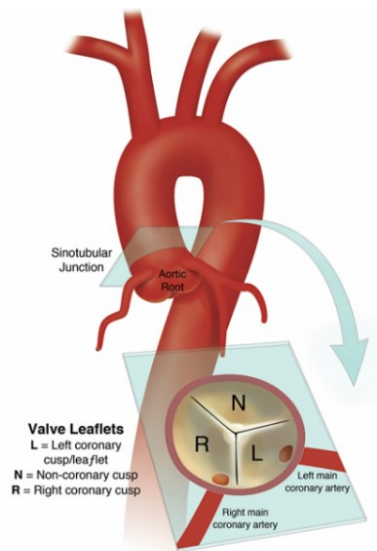


Figure 2-5. Schematic of the aortic arch and aortic valve (AV) anatomy. The AV contains three leaflets/cusps (Left coronary leaflet (L), Right coronary leaflet (R), and None coronary leaflet (N)). (taken from University of Florida's health webpage <https://m.ufhealth.org>)

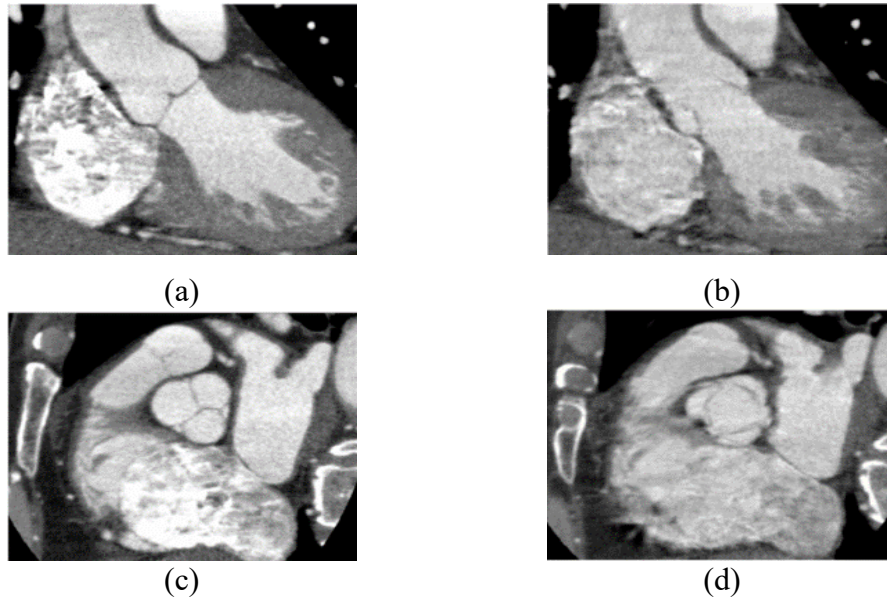


Figure 2-6. Example of plane selection for evaluation of aortic valve morphology in patient with normal aortic valve on ECG-gated multidetector CT. Note normal three cusps and aortic valve in diastolic phase (a, c) and opening in systolic phase (b, d) of double-oblique reconstruction images. (images are taken from Chun et al. 2008)

Modeling and inclusion of valve in the aortic model is essential as it regulates the flow through the aorta and significantly modulated the velocity profile of the systolic jet emanating into the aorta. However, as shown in Figure 2-6 the complete geometry of the open and closed aortic valve cannot be extracted from the CTA images despite its relatively high spatial resolution. The valve modeled in this research is semi-patient-specific as the annulus of the patient is extracted and the open and closed forms of the valve are then created according to the patient's sinus geometry and the existing known shapes in literature. (De Hart, Peters, Schreurs, & Baaijens, 2003; M.-C. Hsu et al., 2014; Wong et al., 2013). Figure 2-7a. illustrates the AV construction in open and closed forms.

In addition, with low temporal resolution of the CTA, the motion of the valve cannot be obtained and it needs to be modeled using a canonical displacement curve or

other imaging modality such as Echo. Since the valves are elastic and deform throughout the cardiac cycle, the valve motion is modeled employing prescribed kinematics without any fluid-structure interaction (FSI). One of the reasons for this is that there is still not a complete understanding of the tissue properties of the valve leaflets and the corresponding constitutive models are yet to be determined precisely. Furthermore, while FSI is best suited for the prediction of the valve motion, it adds substantial additional computational cost to the flow-only simulation. Furthermore, the purpose of this work's computational modeling of the aortic arch is to investigate the contrast dispersion in aorta with realistic patient geometry and adding the FSI feature would not have a strong effect on the results.

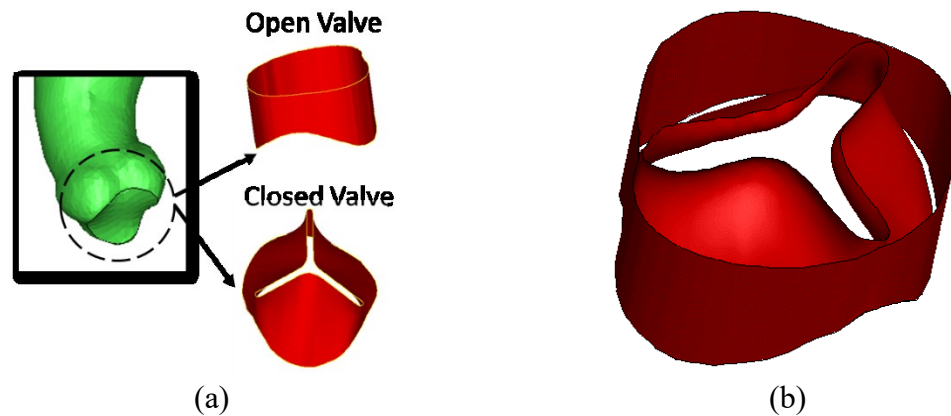


Figure 2-7. (a) Aortic valve model construction from the aortic valve annulus. The open and closed forms are created from the observation of valve shapes in literature (De Hart, Peters, et al., 2003; M.-C. Hsu et al., 2014; Wong et al., 2013). (b) Open and closed forms of the aortic valve super-imposed after performing LDDMM algorithm (Beg, Miller, Troune, & Younes, 2005; Miller, Troune, & Younes, 2002) to register and match surfaces between the two forms.

2.2.1.4. Aortic Valve Kinetics and Prescribed Motion

In the current procedure, the prescribed kinematics of the valves is based on a sinusoidal function where the period and the duration of the peak are determined and synchronized with systolic and diastolic phase taken from the inlet velocity of the flow. The kinematics of the valve are inspired by two previous numerical and experimental (Bellhouse & Talbot, 1969; Swanson & Clark, 1973) and in-vivo (Leyh, Schmidtke, Sievers, & Yacoub, 1999) studies. Based on the observations from the studies, the valve leaflets time variation of velocity and displacement as well as the input velocity for this study is shown in Figure 2-8 where the opening time is chosen based on the time raise to the peak velocity and the closing time is the remaining time from when velocity begins to drop to end of systole. Eq. 2-1a and 2-2b are the mathematical formations of the prescribed velocity (v_{valve}) and displacement (d_{valve}) of the leaflets, respectively:

$$\vec{v}_{valve}(x, t) = a(t) \cdot \vec{b}(\vec{x}) \quad (2-1a)$$

$$\vec{d}_{valve}(x, t) = c(t) \cdot \vec{b}(\vec{x}) \quad (2-1b)$$

where, $a(t)$ and $c(t)$ describe the time variation of the valve velocity and displacement in time defined in Eq. 2-2a and 2-2b and $\vec{b}(\vec{x}) = \vec{x}_{open} - \vec{x}_{close}$ is the valve motion shape function.

$$a(t) = \begin{cases} \frac{\pi}{2T_o} \sin(\frac{\pi t}{T_o}), & t \leq T_o \\ -\frac{\pi}{2T_c} \sin(\frac{\pi(t - T_o)}{T_c}), & T_o \leq t \leq T_c \end{cases} \quad (2-2a)$$

$$c(t) = \int a(t)dt = \begin{cases} \frac{1}{2}(1 - \cos(\frac{\pi t}{T_o})), & t \leq T_o \\ \frac{1}{2}(1 + \cos(\frac{\pi(t - T_o)}{T_c})), & T_o \leq t \leq T_c \end{cases} \quad (2-2b)$$

where $T_o = 0.12$ (s) and $T_c = 0.42$ (s) are the opening and closing times of the valve, respectively defined in Figure 2-8 resulting in the total systolic time of $T_{sys} = 0.54$ (s).

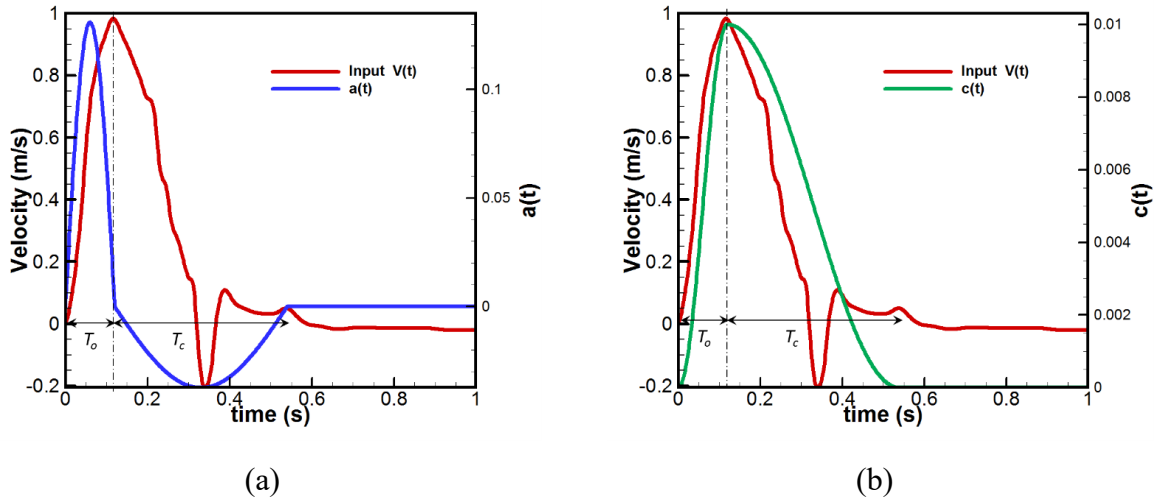


Figure 2-8. Velocity (a) and displacement (b) time variation of the valve compared with the inflow velocity profile. The opening time of the valve is defined as the time it takes to rises to the peak velocity and the closing phase is the time duration from peak velocity until end systole.

2.2.1.5. Surface Registration and Interpolation

The valve geometry for the two stages (open and closed) extracted from the image processing and CAD construction is each represented by a distinct mesh made up of triangular elements. However, since each of these meshes has been processed independently, it is not necessarily guaranteed that the generated triangulated surface maintains the same mesh topology between these two frames. Instead, these surfaces have

different number of nodes, elements and order of connectivity. Therefore, it is required to register the two surfaces from one to another to create a smooth mapping between the two open and closed frames and prescribe this moving surface as a time-dependent kinematic boundary condition to the flow solver. The mapping of the two morphologies can be obtained by variety of surface registration and matching algorithms (Maintz & Viergever, 1998; Mäkelä et al., 2013; McInerney & Terzopoulos, 1995; Salvi, Matabosch, Fofi, & Forest, 2007). Here we employ a diffeomorphic registration algorithm known as Large Deformation Diffeomorphic Metric Mapping (LDDMM, (Beg et al., 2005; Miller et al., 2002)). LDDMM is chosen because it can handle the large local deformations of the valve between the open to closed forms. Methods such as iterative closest point (Besi & McKay, 1992) and elastic non-rigid deformation algorithms (Bajcsy & Kovačič, 1989; Ledesma-Carbayo et al., 2005) are not diffeomorphic and are only appropriate for small local deformations. The LDDMM algorithm performed on the aortic valve is with fully open leaflets before prescribing the kinematic deformation of the leaflets mainly because registering fully opened leaflets results in faster convergence and yields less distortion. The triangulated surfaces of the valves obtained from the LDDMM registration are interpolated in time to ensure one-to-one correspondence between the surface nodes and also preserving the mesh topology. This smooth interpolation allows us to extract the triangulated surface at any time instance during the cardiac cycle and thus, can be prescribed as a moving membrane in the flow solver.

2.3. GOVERNING EQUATIONS AND CFD SOLVERS

2.3.1. ViCar3D

ViCar3D is an in-house, immersed boundary based flow solver that is employed for the simulations of aortic flow in the current research.

2.3.1.1. Immersed Boundary Method

Although blood is strictly a non-Newtonian fluid and exhibits shear-thinning behavior, in large vessels such as the primary coronary arteries and the aorta, where the shear rate is high, it can be treated as a Newtonian fluid. In the studies presented in this work, the blood flow is modeled by the Navier-Stokes equations for a Newtonian, viscous, and incompressible flow (Eq. 2-3a and 2-3b):

$$\frac{\partial u_j}{\partial x_j} = 0; \quad (2-3a)$$

$$\frac{\partial u_i}{\partial t} + \frac{\partial(u_i u_j)}{\partial x_j} = \frac{1}{\rho} \frac{\partial p}{\partial x_i} + \nu \frac{\partial}{\partial x_j} \frac{\partial u_i}{\partial x_j} \quad (2-3b)$$

where $i, j = 1, 2, 3$ are the coordinate directions, u_i are the flow velocity components, p is the static pressure of the fluid, ρ is the fluid density and ν is the fluid kinematic viscosity. The flow is solved via a previously implemented immersed boundary solver ViCar3D and the key components are explained here. The Navier-Stokes equations (Eq. (2-3a and b)) are discretized using a second-order, cell-centered, collocated grid arrangement of two main variables of u_i and p . The viscous terms ($\nu \frac{\partial}{\partial x_j} \frac{\partial u_i}{\partial x_j}$) is implemented using a central-difference scheme while the convection terms ($\frac{\partial(u_i u_j)}{\partial x_j}$) is

discretized using a linear combination of an upwind and second-order central schemes (Ghias, Mittal, & Dong, 2007). The two terms are both treated implicitly in time utilizing a second-order Crank-Nicolson method for unconditional stability and this eliminates the viscous stability constraint. The time advancement used here is a second-order fractional-step method proposed by Zang et al. (Zang, Street, & Koseff, 1994). In summary, this method includes three steps where first, the solution is advanced to an intermediate step by solving the advection-diffusion equation (Eq. 2-4) to solve for an intermediary velocity field (u_i^*). Subsequently, to solve for the pressure correction (p') Poisson equation (PPE, Eq. 2-5) is solved using a bi-directional conjugate gradient based (BiCGSTAB) method (Van Der Vorst, 1992) with a Jacobi pre-conditioner. The last step consists of updating the velocity field using the corrected pressure where the face-centered velocity (U_i) and cell-centered velocity (u_i) are updated separated in equations Eq.2-6 and 2-7 (R. Mittal et al., 2008; Zang et al., 1994).

$$\frac{u_i^* - u_i^n}{\Delta t} = \frac{1}{2} \left(-\frac{\delta(U_j u_i)}{\delta x_j} + \nu \frac{\delta}{\delta x_j} \frac{\delta u_i}{\delta x_j} \right)^* + \frac{1}{2} \left(-\frac{\delta(U_j u_i)}{\delta x_j} + \nu \frac{\delta}{\delta x_j} \frac{\delta u_i}{\delta x_j} \right)^n \quad (2-4)$$

$$\frac{1}{\rho} \frac{\delta}{\delta x_j} \frac{\delta p'}{\delta x_j} = -\frac{1}{\Delta t} \left(\frac{\delta U_i^*}{\delta x_j} \right) \quad (2-5)$$

$$u_i^{n+1} = u_i^* - \frac{\Delta t}{\rho} \left(\frac{\delta p'}{\delta x_j} \right)_{cc} \quad (2-6)$$

$$U_i^{n+1} = U_i^* - \frac{\Delta t}{\rho} \left(\frac{\delta p'}{\delta x_j} \right)_{fc} \quad (2-7)$$

where δ , denotes the central difference operator. The separate update of cell-centered (cc) and face-centered (fc) values of velocity has shown to obey the mass conservation by Zang et al. (Zang et al., 1994). The present simulations were employed using a 50% second-order up-winding to better control the numerical dispersion errors as described in Ghias et

al. (Ghias et al., 2007). The flow solver used in this study employs a sharp interface immersed boundary method based on stair-step method (SSM) where the ghost point is defined by the closest image point normal to the boundary and has the face value of closest cell to the body (See Figure 2-9). Given the errors involved in segmentation of the lumen and the finite resolution of the imaging, a stair-step representation of the boundary is acceptable for the current work. Immersed boundaries are represented by surface meshes with triangular elements and are placed in a Cartesian grid that covers a 3D domain (See Figure 2-9a). Since, the vascular wall is assumed to be rigid, the walls boundaries are set to have zero velocity with Neumann boundary condition for pressure.

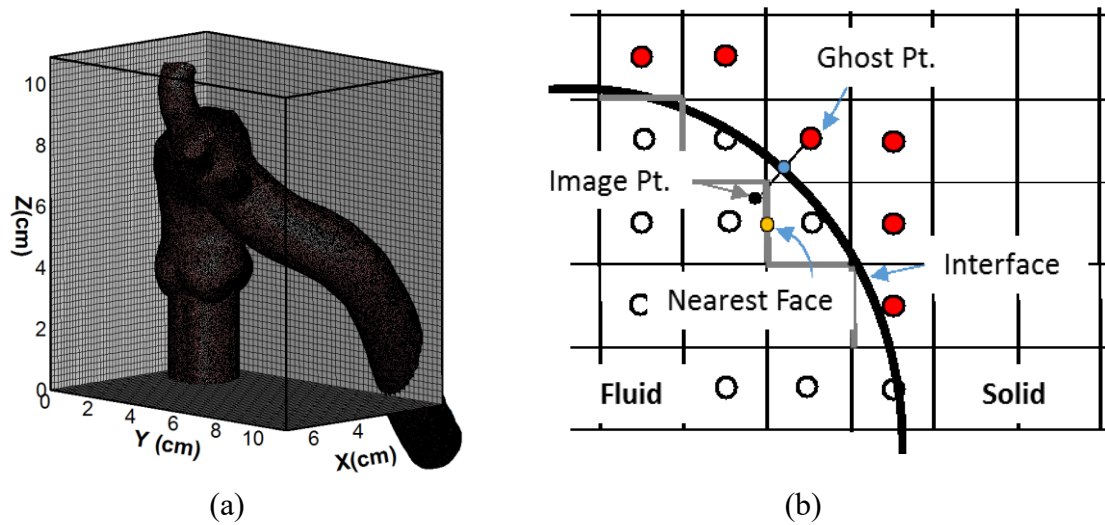


Figure 2-9. (a) Triangulated surface of an aorta immersed into the background Cartesian volume grid. The model includes the coronary sinus, aortic valve and three arch branches at the top. (b) Schematic of the stair step method for the immersed boundary treatment.

2.3.1.2. Scalar Addition for Contrast Dispersion

In ViCar3D, the contrast concentration is treated as a scalar dispersing through the flow and is modeled as an unsteady convection-diffusion equation with now source or sink of the contrast from the walls (Eq. 2-8):

$$\frac{\partial C}{\partial t} + \frac{\partial}{\partial x_j}(u_i C) = \frac{\partial}{\partial x_j} \left(D \frac{\partial C}{\partial x_j} \right) \quad (2-8)$$

where D is the molecular diffusivity coefficient and is assumed to be constant and C is the contrast concentration. The advection-diffusion is then solved implicitly in time using the Crank-Nicolson scheme for both the convective and diffusion term and a central-finite difference scheme is used in space resulting in second order accuracy in both time and space (Eq. 2-9). It is noted however that the convection term is solved after the N-S equations are solved and employs the available cell-centered velocity for calculation. The semi-discrete version of the equation therefore is:

$$\begin{aligned} \frac{C^{n+1} - C^n}{\Delta t} = & \frac{1}{2} \left[\left(D \frac{\delta}{\delta x_j} \frac{\delta C}{\delta x_j} - \frac{\delta(u_i C)}{\delta x_j} \right) \right]^{n+1} \\ & + \frac{1}{2} \left[\left(D \frac{\delta}{\delta x_j} \frac{\delta C}{\delta x_j} - \frac{\nabla(u_i C)}{\nabla x_j} \right) \right]^n \end{aligned} \quad (2-9)$$

where, δ , is the central difference operator, ∇ denotes the second order upwind operator and u_i is the cell centered solved velocity by the N-S equations.

The non-dimensional numbers that are relevant to cardiac flows and contrast dispersion also need to be defined. The flow Reynold's number, $Re = \frac{2V_{mean}R_{AO}}{\nu}$, is defined based on the mean velocity of inflow at the aortic root (V_{mean}), diameter of the aortic annulus ($2R_{AO}$) and kinetic viscosity of blood (ν). In cardiac flows, since the flow is pulsatile, another important non-dimensional number is the Womersely number, =

$R\sqrt{\nu/T}$, where T is the cardiac cycle period (or duration of the cardiac cycle). In addition, when studying contrast dispersion, the effect of molecular diffusivity over convection becomes important and the Schmidt number, $Sc = \frac{\nu}{D}$, where D is the molecular diffusivity coefficient is defined to study such effect.

2.3.2. ANSYS CFX

In parallel with the previously developed flow solver -ViCar3D- for simulations of the aortic flow, the commercial software, ANSYSTM Workbench 14.5, was used to solve for flow in coronary arteries and artery models where there were no moving boundaries. ANSYS CFX uses a finite volume method where the finite volume is constructed via a discretized spatial domain. ANSYS CFX uses a co-located (non-staggered) grid layout such that the control volumes are identical for each transport equation. Each finite volume element is used as a control volume to conserve relevant quantities such as mass, momentum and energy. For example, the mass conservation and momentum equations of the forms Eq. 2-10 and 2-11, respectively, are integrated over each control volume.

$$\frac{\partial \rho}{\partial t} + \frac{\partial}{\partial x_j}(\rho u_j) = 0 \quad (2-10)$$

$$\frac{\partial}{\partial t}(\rho u_j) + \frac{\partial}{\partial x_j}(\rho u_j u_i) = -\frac{\partial p}{\partial x_i} + \frac{\partial}{\partial x_j} \left(\mu_{eff} \left(\frac{\partial u_i}{\partial x_j} + \frac{\partial u_j}{\partial x_i} \right) \right) \quad (2-11)$$

With the Gauss' Divergence Theorem applied to the volume integrals with divergence and gradient operators to surface integrals, the two latter equations become:

$$\frac{d}{dt} \int_V \rho dV = \int_V \rho u_j dn_j = 0 \quad (2-12)$$

$$\begin{aligned}
& \frac{d}{dt} \int_V \rho u_i dV + \int_S \rho u_j u_i dn_j \\
& = \int_S p dn_j + \int_S \mu_{eff} \left(\frac{\partial u_i}{\partial x_j} + \frac{\partial u_j}{\partial x_i} \right) dn_j + \int_V S_{u_i} dV
\end{aligned} \tag{2-13}$$

where, V and S respectively denote volume and surface regions of integration, and dn_j are the differential Cartesian components of the outward normal surface vector. The volume integrals represent source or accumulation terms, and the surface integrals represent the summation of the fluxes. The advection term in Eq. 2-13 is discretized via a “High Resolution” scheme which is explained in Barth et al (Barth, T.J, Jespersen, 1989) where the transient terms are solved using second order backward Euler scheme.

CHAPTER 3: HEMODYNAMICS OF LARGE VESSELS VIA DISPERSION OF CONTRAST AGENT IN CTA

3.1. INTRODUCTION

Despite the advancement in contrast-enhanced CT imaging, no group to our knowledge has been able to estimate the coronary blood flow (CBF) velocity, an important clinical factor, through the arteries via CT imaging contrast information and fluid dynamics. In contrary, instead of velocity, pressure drop measurements across the stenosis both invasively (Pijls et al., 1996) and non-invasively via computational fluid dynamics (C. A. Taylor et al., 2013) have been studied to calculate the fractional flow reserve (FFR) quantity to determine the severity of the disease.

In current work, we introduce a novel method to non-invasively estimate CBF and via contrast dispersion in coronary arteries and measurement of transluminal contrast gradient (TCG) (See Figure 3-1). It is important to note that to the best of our knowledge, while a number of studies have attempted to correlate TCG with measures of stenotic severity (Choi et al., 2011, 2012; Chow et al., 2011; Steigner et al., 2010; Stuijzand et al., 2014), none of these studies have attempted to put forth a physics-based mechanism for the generation of TCG or have obtained a strong quantitative correlation between TCG and the other hemodynamic parameters. Therefore, the significance of the present work is that we propose and validate a physical (causal) mechanism for TCG and provide a quantitative relationship between TCG and the coronary flow using computational modeling.

The implications of the findings of the current study on the diagnosis of coronary artery disease (CAD) are potentially significant. Diagnosis of CAD typically begins with a cardiac stress test which is ultimately used to help determine which patients should be referred to invasive coronary catheterization and possible coronary revascularization (Lloyd-Jones et al., 2010; San Román et al., 1998). Although a normal cardiac stress test indicates an excellent prognosis and a low incidence of major adverse cardiovascular events, stress testing has not been an adequate “gatekeeper” to the catheterization lab, as it leads to a significant number of unnecessary invasive procedures (Patel et al., 2010) at a staggering healthcare cost and patient risk exposure. Invasive tests such as fractional flow reserve (FFR) predict those who can benefit from stents, but carry the inherent expense and risks of catheterization (Lange & Hillis, 2003). New diagnostic assays that combine CCTA with computational fluid dynamics (CFD) are promising (Nakazato et al., 2013) but involve a high degree of complexity and cost. The ability to rapidly and accurately quantify coronary hemodynamics from a standard CCTA exam, could serve as a highly potent alternative to these existing CAD diagnoses, and enable appropriate and cost-effective health care to be deployed. Such a diagnostic method could also serve as a “gatekeeper” for these invasive therapies and lead to a significant reduction in unnecessary invasive catheterization; this would not only generate significant savings in direct healthcare costs, it will also reduce the indirect costs and patient risks associated with these invasive procedure including heart attack, stroke, and death.

In this Chapter, we use computational fluid dynamics (CFD) modeling to examine the mechanism for TCG generation in stenosed coronary arteries and assess the correlation of TCG established metrics of stenotic significance. Idealized and patient-derived models

of a prototypical coronary artery with stenoses varying in severity from 0% (unstenosed) to 80% (based on area constriction) are employed, and the equations of flow and contrast agent dispersion solved simultaneously in these models. The modeling approach allows a high level of control of all key parameters and variables, and provides data that facilitates the delineation of flow mechanisms from imaging artifacts. The TCG obtained from the simulations is correlated with physiologic and hemodynamic parameters and used to test our primary hypothesis regarding the mechanics for TCG generation – that TCG reflects the convection of a time-varying contrast bolus into the coronary artery, and therefore encodes information about the coronary blood flow velocity.

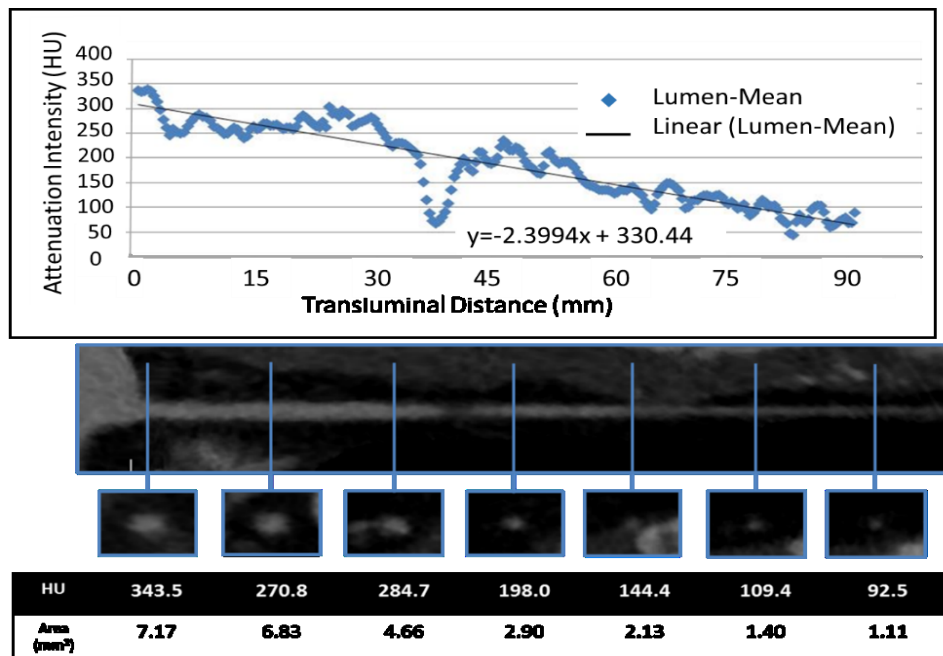


Figure 3-1 Representative example of transluminal contrast gradient for a stenosed artery. Luminal cross sections are sampled every 0.5 mm and plotted over the vessel length to obtain an axial variation of cross-sectional averaged attenuation (HU) (top figure). Bottom figure shows the axial and cross-sectional visualizations of lumen area by contrast agent. HU is the Hounsfield unit for the attenuation level. The lesion section is shown with an arrow. CT

imaging is acquired using a 320-row detector CT scanner (AquilionTMOne -Toshiba Medical Systems Corporation, Otawara, Japan).

3.2. METHODS

3.2.1. Governing Equations

In Chapter 2, we provide a computational framework for which the current simulations have been employed. Briefly, the blood flow inside the modeled coronary artery is assumed to be Newtonian and the hemodynamics is simulated by solving the incompressible Navier-Stokes equations,

$$\frac{\partial \vec{U}}{\partial t} + (\vec{U} \cdot \vec{\nabla}) \vec{U} + \frac{\vec{\nabla} P}{\rho} = \nu \nabla^2 \vec{U}; \quad \vec{\nabla} \cdot \vec{U} = 0 \quad (3-1)$$

where \vec{U} is the flow velocity, P is pressure, ρ and ν are the density and kinematic viscosity of the blood respectively. The flow in any artery is driven by the simplified transarterial pulsatile pressure drop (ΔP) and we prescribe this as an input in our both diseased and normal model as;

$$\Delta P = P_A + P_B \sin(2\pi \cdot HR / 60 \cdot t) \quad (3-2)$$

where HR is the heart rate in beats per minute (BPM). A Neumann type boundary condition is applied for the velocity at the inlet and exit, and a no-slip boundary condition is used on the vessel wall.

Since the volume fraction of the contrast agent is extremely low for CTA, the contrast agent can be modeled as a passive scalar (Durant, Waechter, Hermans, Weese, &

Aach, 2008). The governing equation for the contrast agent concentration, C (mg/ml) is then given by;

$$\frac{\partial C}{\partial t} + (\vec{U} \cdot \vec{\nabla})C = D\nabla^2 C \quad (3-3)$$

where \vec{U} is the flow velocity obtained from the solution of Eq. (3-1), D is the molecular diffusivity of the contrast agent in the blood. This model has been used for the simulation of contrast agent dispersion in many previous studies (Lloyd-Jones et al., 2010; Patel et al., 2010; San Román et al., 1998). Interestingly, the diffusivity of the contrast agent in the blood is not well characterized and past studies have employed Schmidt numbers ($Sc = \nu/D$) ranging from 1 to 1000 (Durant et al., 2008; Kim, Cheer, & Dwyer, 2004). In the present study, we use $Sc=1$ and the effect of Sc on the TCG will be discussed in the later section. Given that contrast is excluded from the intracellular space and thus should not cross the coronary endothelium, a zero wall flux boundary condition for the contrast agent is applied as an approximation to the actual physics on the lumen boundary. This is also consistent with previous computational models of contrast transport in arteries (Lloyd-Jones et al., 2010). Furthermore, we employ a convective outflow boundary condition at the downstream ends of the arteries. The boundary condition at the inlet is more complex and is described in the following section.

3.2.2. Arterial Input Function (AIF)

The time-variation of the contrast agent concentration at the coronary ostium, referred to here as the “arterial input function,” (AIF) is a key factor that effects contrast agent gradients, and needs to be prescribed as an input in the model. In the automated bolus triggering method typically employed in CCTA, the attenuation level is tracked at a

reference position in the aorta, and the final image acquisition scan triggered at some prescribed HU level (300 HU in Figure 3-2a) which is usually at or near the peak of the bolus. This data is typically discarded in a standard CTA acquisition but as has been shown recently, the AIF can be used to improve myocardial CT perfusion measurements (George, Richard T; Ichihara, Takashi; Lima, Jaoa A.C.; Lardo, 2010). Figure 3-2a shows an AIF captured at the descending aorta in a patient with coronary artery disease undergoing clinical CTA. This shows a smooth rise from a nominal value of about 50 to a peak value of about 350 to 400 HU, at which point the image is acquired. The scanner is triggered at around 300 HU in the current protocol and the volume images are acquired 1-2 heart beat after. Figure 3-2b represents the AIF in a canine model in which a smooth but rapid ride to maximum as the bolus arrives in the aorta similar to human studies, followed by a slow decay reflecting the flushing out of the contrast agent bolus. The typical time-delay between arrival of the bolus and maximum enhancement in human studies ranges from 10 to 15 seconds. Given the fact that the attenuation at the descending aorta is not significantly different from the value at the coronary ostium (aortic root), and the attenuation in Hounsfield units (HU) is directly proportional to the contrast agent concentration C (George, Richard T; Ichihara, Takashi; Lima, Jaoa A.C.; Lardo, 2010), the recorded AIF shown in Figure 3-2a. can be used for the inlet boundary condition of the contrast agent. In order to model this, we prescribe the arterial input function in terms of concentration, C as :

$$C_{ostium}(t) = C_{min} + \frac{1}{2}(C_{max} - C_{min}) \left(1 - \cos \frac{\pi(t - t_s)}{T_d} \right) \quad (3-4)$$

where C_{\max} and C_{\min} are the maximum and minimum concentrations at the ostium, t_s is the arrival time of the bolus, and T_d is the time-delay between the arrival of the bolus and the maximum enhancement. This function provides a reasonable representation of the actual time-variation of attenuation in patients as shown in Figure 3-2a. and we choose $T_d=10-20$ (sec) for our simulations. Note that the modeling of the contrast agent dispersion starts at $t=t_s$ and continues till $t=t_s+T_d$ and the distribution of the contrast agent (and associated attenuation) in the artery examined at $t=t_s+T_d$. We also note here that other functions (such as for instance, linear with time) could also be used to represent the AIF; this would not change the essential features of the mechanism proposed here but would change the precise form of the mathematical formulae that are derived in later sections.

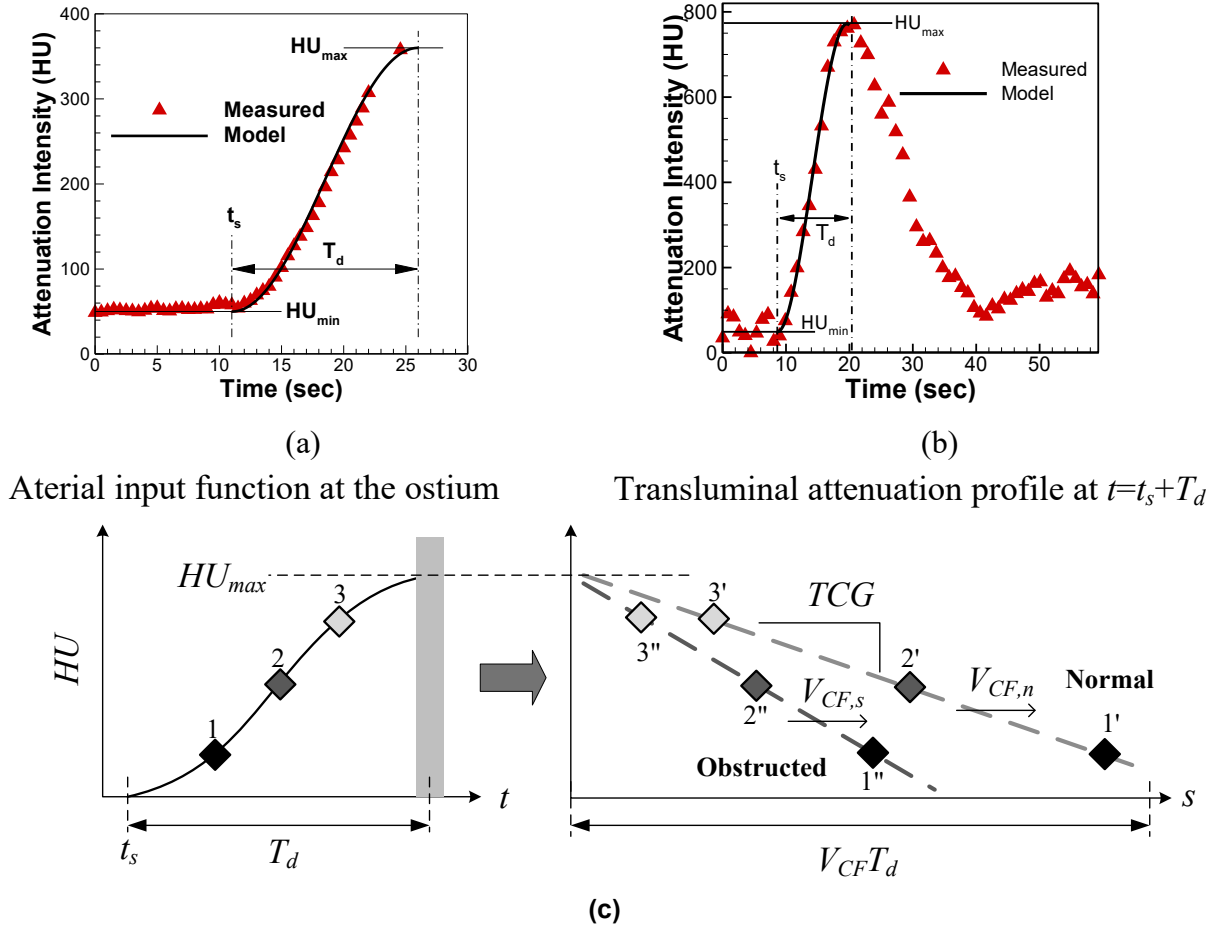


Figure 3-2 Representative Arterial input function (AIF) measured in actual CCTA as well as the fitted function that is employed in the simulations in a human studies (A) and a canonical study (B). Part C is a schematic to illustrate the mechanism described in the paper: TCG is the transluminal (spatial) projection of the time profile of the concentration of the contrast agent and hence is driven by the coronary blood flow velocity (VCF).

3.2.3. Arterial Attenuation and TCG Calculation

As shown in Figure 3-1., TCG is derived from the axial variation of cross-sectional averaged attenuation. The attenuation averaged over the cross sectional lumen area at a given axial location, s (mm) (see Figure 3-3), at any given time instance normalized by the maximum attenuation increase at the coronary ostium is given by:

$$HU^*(s) = \frac{HU(s)}{HU_{\max} - HU_{\min}} = \frac{\bar{C}(s)}{C_{\max} - C_{\min}}; \quad \bar{C}(s) = \frac{1}{A(s)} \int_{A(s)} C dA \quad (3-5)$$

where $A(s)$ is the cross-sectional area. Note that in the above, we denote the attenuation in terms of the Hounsfield Units (HU) as is traditionally done in CT imaging (Choi et al., 2011). The assumption here is that the attenuation is linearly proportional to the contrast agent concentration (WD & M., 2003). The contrast agent attenuation is computed at 2 mm intervals along the artery and the normalized transluminal contrast gradient (TCG*) is estimated as the slope of the linear regression fit to this normalized transluminal attenuation profile. For example, if the profile is fit to the linear function as $HU^*(s) = a*s + b$, then TCG* is given by the slope a , and its unit is (mm^{-1}) . The spatial resolution chosen does not affect the results since a linear regression has employed and is the resolution is chosen to be close to the value of 5 mm which is typical for new scanners.

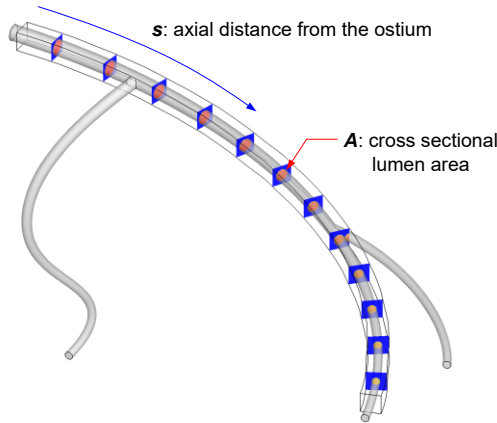


Figure 3-3. Extraction of cross-sectional lumen area along the axial direction from the CFD simulation for the calculation of transluminal contrast gradients.

3.2.4. Fractional Flow Reserve

While there are a number of metrics/indices proposed for evaluating the functional significance of arterial lesions, fractional flow reserve (FFR) has emerged as the gold

standard for the assessment of the functional significance of arterial stenoses (Bishop & Samady, 2004). As such, some recent studies have attempted to correlate TCG with FFR (Choi et al., 2012; Yoon et al., 2012). In the current study, we use the fractional flow reserve based on the flow rate (FFR_Q) as a functional measure of the severity of coronary stenosis (Bishop & Samady, 2004). The flow-rate based FFR is defined by $FFR_Q = Q_s / Q_n$, where Q_s is the flow rate in the stenosed artery at the hyperemic condition, and Q_n is the hyperemic flow rate in the same artery without the stenosis. FFR_Q is readily available from our computational model since we simulate the flow in both the stenosed and unstenosed arteries. We note that FFR is in practice measured at hyperemic conditions to minimize the myocardial resistance and distinguish the effect of the stenosis resistance. However in our models (which is an idealized coronary artery segment) since we are not modeling the resistance of the myocardial capillary network, we cannot model the induction of hyperemia. Thus, our approach might not reproduce the numerical values of FFR typically measured in clinical settings; however it is expected that the trends in FFR with stenotic severity and correlation with TCG should be recovered reasonably well.

3.2.5. Analytical Investigation of Mechanism for TCG

The dispersion of contrast agent is governed by the convection-diffusion equation, Eq. (3-3). For a simple pipe flow, the equation for axial gradients of the cross-sectional area-averaged concentration, \bar{C} (which is directly connected with TCG, see Eq. 3-5) can be written as:

$$\frac{\partial \bar{C}}{\partial s} = -\frac{1}{\bar{U}} \frac{\partial \bar{C}}{\partial t} + \frac{1}{\bar{U}} \left(D + \frac{d^2 \bar{U}^2}{B \cdot D} \right) \frac{\partial^2 \bar{C}}{\partial s^2} \quad (3-6)$$

where $\bar{U} = Q / A$, s is the axial distance, d is the diameter of the pipe. The first term on the right hand side of Eq. (3-6) is the advection of the input bolus (i.e. AIF) and the other terms are the axial molecular diffusion and the Taylor dispersion effects (G. Taylor, 1953) which is caused by the non-uniform cross-sectional velocity profile. For a parabolic velocity profile, the constant B in the Taylor dispersion term can be evaluated analytically and is equal to 192.

Now we apply scaling analysis to each term on the right hand side of Eq. (3-6). From Eq. (3-4), since the concentration varies by $\Delta C = C_{\max} - C_{\min}$ over T_d , the order of magnitude of the first term on the right-hand-side is $O(\Delta C / (T_d \bar{U}))$, and if we take $(T_d \bar{U})$ as the axial length scale, the orders of magnitude for molecular diffusion and Taylor dispersion are given by $O(\Delta C \cdot D / (T_d^2 \bar{U}^3))$ and $O(\Delta C \cdot d^2 / (T_d^2 \bar{U} \cdot BD))$, respectively. If the typical values for the LAD coronary flow ($\bar{U} = 10$ cm/sec (Hozumi et al., 1998) $T_d = 10$ sec, $d = 3$ mm (Funabashi, Kobayashi, Perlroth, & Rubin, 2003)) are substituted, the ratio of molecular diffusion and Taylor dispersion effects to the bolus propagation effect are $4 \times 10^{-5} / Sc$ and $10^{-3} \times Sc$, respectively (Sc is the Schmidt number, $Sc = \nu / D$). Thus, molecular diffusion effects are negligible compared to the advective effect even for small ($O(1)$) values of the Schmidt number. Taylor dispersion effect would be comparable to advective effects for $Sc = O(10^3)$, but for this regime, the assumption for the Taylor dispersion formulation (radial variation of C is much smaller than \bar{C}) will not hold. Actual CCTA data (Figure 3-1) suggests that the Schmidt number for the contrast agent may not have such a high magnitude since the contrast shows a rather weak variation in the radial direction. Thus we hypothesize here that advection effects are dominant and TCG is therefore a reflection of the advection of the contrast bolus at coronary ostium.

By assuming that the contrast agent dispersion in axial direction is dominated by the advection, and considering axial variation of cross-sectional area, $A(s)$, the equation for \bar{C} can be written as:

$$\frac{\partial \bar{C}}{\partial t} + \frac{Q}{A(s)} \frac{\partial \bar{C}}{\partial s} = \frac{\partial \bar{C}}{\partial t} + Q \frac{\partial \bar{C}}{\partial \eta} \approx 0, \quad (3-7)$$

where $\eta = \int A(s) ds$. The solution of Eq. (3-7) is given by

$$\bar{C}(t, s) \approx C_{ostium}(t - V(s)/Q), \quad (3-8)$$

where $V(s) = \int_0^s A(s) ds$ and C_{ostium} is the time variation of concentration at $s=0$, i.e the arterial input function (AIF). The normalized TCG (TCG*) can be given by the slope of linear regression line for $\bar{C}(t, s)/\Delta C$, where $\Delta C = C_{max} - C_{min}$. Based on the mean value theorem, the slope is given by

$$TCG^* = \frac{1}{\Delta C} \frac{\bar{C}(s_b) - \bar{C}(s_a)}{s_b - s_a} = \frac{1}{\Delta C} \frac{\partial \bar{C}}{\partial s}(\hat{s}) \quad (3-9)$$

where s_a and s_b are the axial locations where $\bar{C}(t, s)/\Delta C$ intersects with the linear regression line, and $s_a \leq \hat{s} \leq s_b$ and is the local axial direction along the vessel which is located at the section of interest where TCG is measured (i.e. TCG* is represented by the linear slope between the proximal (s_a) and distal (s_b) points.)

From Eqs. (3-7) and (3-8), we get:

$$TCG^* \approx -\frac{1}{\Delta C} \frac{A(\hat{s})}{Q} \frac{\partial \bar{C}}{\partial t}(\hat{s}) \approx -\frac{1}{\Delta C} \frac{A(\hat{s})}{Q} \frac{\partial}{\partial t} C_{ostium}(t - V(\hat{s})/Q) \quad (3-10)$$

Thus, TCG^* is inversely proportional to the flow rate, Q , but also related with the arterial input function, $C_{ostium}(t)$. Substituting in the AIF used in the present study (Eq. 3-4) into Eq. (3-10), the TCG^* at $t=t_s+T_d$ is estimated as:

$$TCG^* \sim -\frac{1}{2} \frac{A(\hat{s})}{Q} \frac{\pi}{T_d} \sin\left(\frac{\pi V(\hat{s})}{T_d Q}\right) \approx -\frac{1}{2} \left(\frac{1}{Q^2}\right) \left(\frac{1}{T_d^2}\right) \pi^2 A(\hat{s}) V(\hat{s}). \quad (3-11)$$

For the typical values for the coronary flow, the term inside the sine function in Eq. (3-11) is $\sim O(0.1)$ and thus it can be approximated as shown above. Most interestingly, this expression clearly suggests the correlation between the TCG and a key hemodynamic variable; the coronary flow rate Q as $TCG^* \sim 1/Q^2$. The expression, Eq. (3-11) and the present hypothesis will be verified by the simulation for the model coronary artery. Figure 3-2c. is a schematic that illustrates the analytical mechanism described: TCG is the transluminal (spatial) projection of the time profile of the contrast agent and hence is driven by the coronary blood flow velocity (V_{CF}). Therefore, comparing to the stenosed vessel, the higher flowrate (and velocity) in the normal vessel will have a lower TCG values and vice versa (Eq. 3-11).

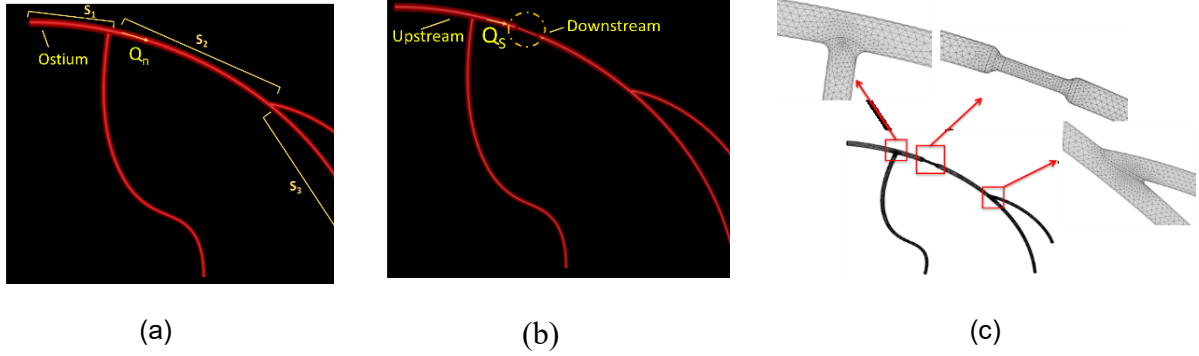


Figure 3-4 (a) An idealized 3-D model of the coronary artery for the normal (unstenosed) case where Q_n is referred to the normal (no stenosis) flow rate. (b) Model of the artery with a stenosis where Q_s is referred to the flow rate in the vessel with stenosis. (d) Computational meshes employed in the various segments of the model.

3.2.6. Quantitative Flow rate Estimation using TCG

Equation (3-11) provides the basis for the non-invasive estimation of coronary blood flow rate using the contrast agent gradients, since all other variables in the equations are known from the CCTA. To estimate the blood flow rate through the vessel, Q , Eq. (3-11) can be re-written as:

$$Q_{TAFE} \approx \frac{\pi}{T_d} \sqrt{\frac{A(\hat{s})V(\hat{s})}{-2 \cdot TCG^*}} \quad (3-12)$$

And, we refer to the above method of determining the flow rate as Transluminal Attenuation Flow Encoding (TAFE). The vessel cross-sectional area, A , volume V , and normalized TCG are all available on the CCTA data, and T_d can be obtained from the AIF. The above equation is derived for a single vessel, while the real coronary artery has many branches. The above method can however be extended for a branched arterial network. Consider a branched artery network shown schematically in Figure 3-4a. If we apply the convection equation, Eq. (3-7) to the main branch connecting segments S_1, S_2 , and S_3 , the

solution for the contrast agent profile at the axial location on the segment 3, for example, will be:

$$\bar{C}(t, s) \approx C_{ostium} \left(t - \frac{V_3(\hat{s})}{Q_3} - \sum_{j=1}^2 \frac{V_j}{Q_j} \right), \quad (3-13)$$

where Q_j and V_j are the flow rate and volume for the segment j , respectively. Basically, Eq. (3-13) is a modification of Eq. (3-8) based on the fact that the flow rate through the each segment is different. Thus, the normalized TCG measured on the each arterial segment is related to the AIF by:

$$TAG_n^* \approx -\frac{1}{\Delta C} \frac{A_n(\hat{s})}{Q_n} \cdot \frac{\partial}{\partial t} C_{ostium} \left(t - \frac{V_n(\hat{s})}{Q_n} - \sum_{upstream} \frac{V_j}{Q_j} \right) \quad (3-14)$$

where the summation on the last term is for the all the upstream segments back to the coronary ostium. For example, if $n=3$, the summation for the upstream should include the segments 1 and 2. Using Eq. (3-14), the flow rate through the segment n , Q_n can be estimated using TCG_n^* as;

$$Q_n = \frac{\tau + \sqrt{\tau^2 + 4 \cdot TCG_n'' \cdot V_n(s)}}{2 \cdot TCG_n''} \quad (3-15)$$

where

$$TCG_n'' = \frac{-2 \cdot TCG_n^* T_d^2}{A_n(\hat{s}) \pi^2} \text{ and } \tau = \sum_{upstream} \frac{V_j}{Q_j} \quad (3-16)$$

where TCG'' is the regulated TCG and τ is the branch retarded time which is the time delay between the coronary ostium and the proximal branching point of the vessel segment. Note that to evaluate τ , the flow rate through all the upstream vessel segments should be known. Thus, Eq. (3-15) should be applied from the most upstream segment to estimate the flow rate sequentially.

Idealized Model

The simulations are conducted using COMSOL™ 4.3 which is an unstructured, finite-volume-based solver. The coronary artery model is discretized with a total of about 2.5×10^5 tetrahedral elements (Figure 3-4c) based on a mesh refinement study. In particular, simulations on a significantly finer mesh with 6×10^5 elements produces at most a 6% difference in the mean flow-rate and 3% in the peak flow rate through the main artery indicating effective grid convergence. The time solver was set to use the Generalized-Alpha Method which is second order accurate (Chung & Hulbert, 1993) and the time-step is chosen according to the physical geometry and not to exceed 0.01 seconds. The solver uses V-cycle second order multigrid for the advection scheme.

Physiological Model

The patient derived model simulations are conducted using ANSYS™ Workbench 14.5. The left coronary artery model is discretized with an unstructured mesh with total of approximately $\approx 4.55 \times 10^5$ tetrahedral elements (Figure 3-9c). Figure 3-5a illustrates the velocity magnitude profile taken at the same cross sectional line (Figure 3-5b) for 4 different grid levels of 'Coarse' with $\approx 2 \times 10^5$, 'Normal' with $\approx 3 \times 10^5$, 'Fine' with $\approx 4.55 \times 10^5$ and 'FineR' with $\approx 9.25 \times 10^5$ tetrahedral elements. This figure illustrates a minimal difference in the peak velocity profile between the Fine and FineR grids; hence all the simulations have been conducted using the 'Fine' grid. The time solver chosen employed a second order backward Euler scheme with a step size of $\Delta t = 0.01$ sec and the high resolution scheme described by Barth et al. (Barth, T.J, Jespersen, 1989) was used to solve the spatial partial derivatives.

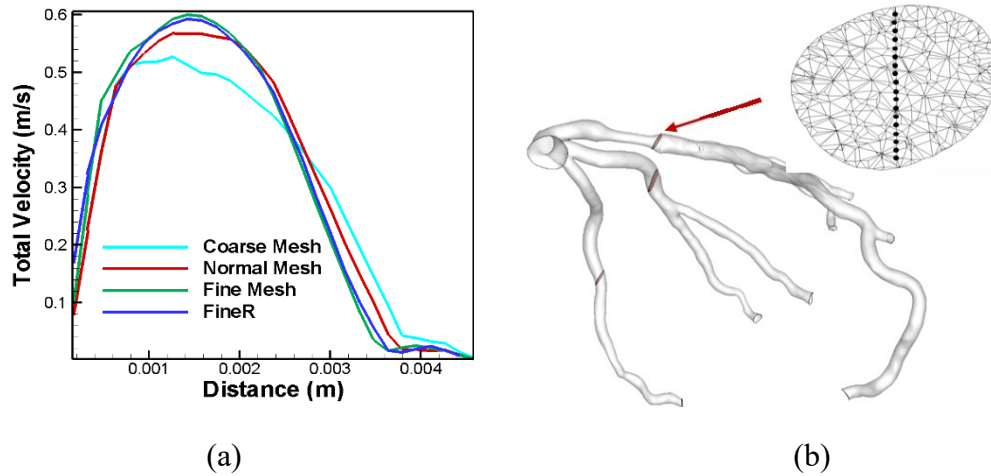


Figure 3-5. (A) Patient Specific velocity magnitude profile comparison between different grid levels for the cross sections shown in (B) in red planes in the main LAD after the stenosis. (B) Cross section plane used in (A). The 4 different grid levels are ‘Coarse’ with $\approx 2 \times 10^5$, ‘Normal’ with $\approx 3 \times 10^5$, ‘Fine’ with $\approx 4.55 \times 10^5$ and ‘FineR’ with $\approx 9.25 \times 10^5$ tetrahedral elements.

3.3. RESULTS

3.3.1. Idealized Model

The first objective here is to understand the fundamental mechanism for TCG generation as well as the effect of features such as flow velocity, bolus duration and arterial bifurcations, which are expected to have a bearing on flow, contrast agent dispersion, and therefore TCG. This is best accomplished with a simple and idealized model of a coronary artery used in this component of the computational study as shown in Figure 3-4. The length of the main artery in this model is 20 cm; the proximal and distal diameter of this artery are 4mm and 2 mm respectively and a linear taper with angle equal to 0.29 degrees is employed. In order to mimic the effect of branching on flow and contrast gradients, we have included two branches from the main vessel; these are located at 16% and 57.5% of

the length of the main vessel. The proximal diameters of these vessels are approximately 3.2 mm and 2.3 mm and the taper angles are 0.16 and 0.10 degrees respectively. We note at the outset that while the topology and dimensions of the model are based generally on a typical left coronary artery, the model is not derived from any patient-specific data and is not anatomically-exact. For the cases with stenosis, axi-symmetric stenoses are created on the main artery segment between the two bifurcations (Figure 3-4). The stenosis extends about 10 mm in the axial direction and the severity (based on area reduction) varies from 50 to 80%.

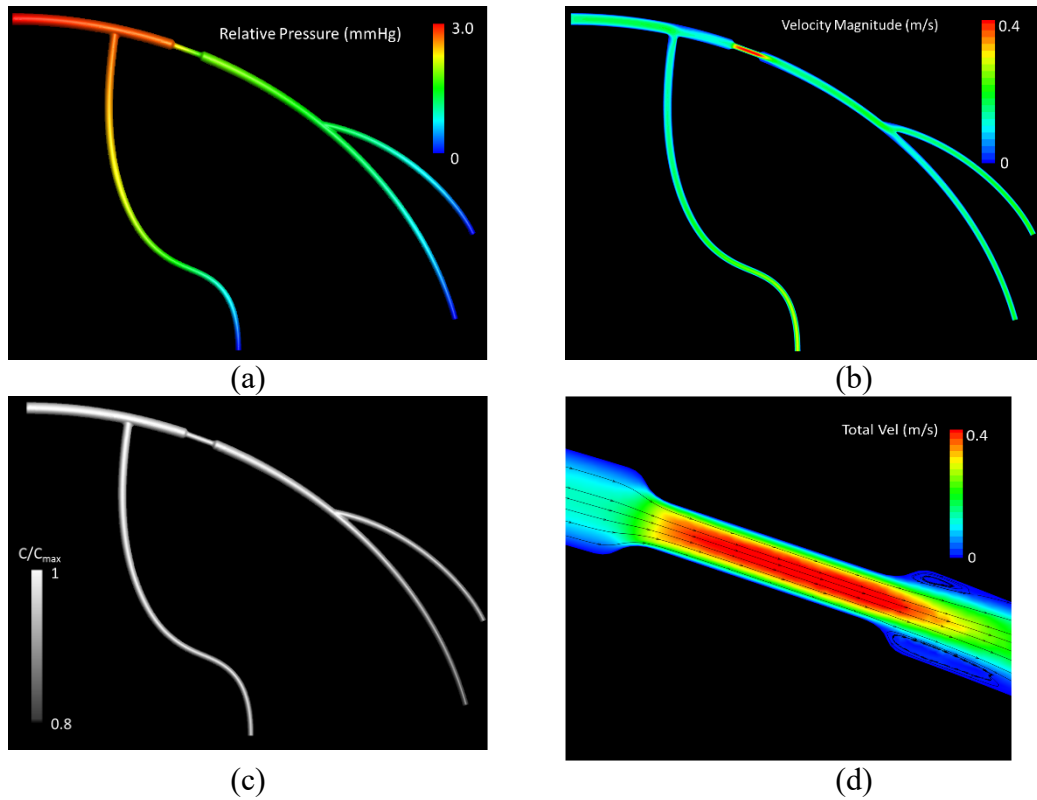


Figure 3-6 Pressure (a), velocity magnitude (b) and normalized contrast agent concentration (c) (C/C_{max}) for the $Q_n=50\text{ml/min}$ case with a 70% area constriction. (d) Velocity magnitude and streamlines in the stenosed region in idealized model.

In order to understand the effect of flow rate on TCG, two different mean flow rate conditions are modeled by choosing $P_A = 3.0$ and 4.5 mmHg and $P_B = 0$ for both flow cases. For the pulsatile flow conditions $HR = 60$ BPM and $P_B = 2.85$ and 4.35 mmHg are chosen for $P_A = 3$ and 4.5 mmHg, respectively. Consistent with the focus on basic mechanisms, the temporal variation of pressure is chosen to be a simple sinusoid that does not mimic the precise variation for coronary arteries. For the normal (unstenosed) artery model, the mean pressure drops of 3 and 4.5 mmHg result in mean flow rates through the main artery of $Q_n = 50$ and 69 (ml/min) respectively. The mean flow velocities are $\bar{U} = 11.8$ and 16.3 (cm/sec), respectively, and these are in the range of measured values for the left anterior descending (LAD) coronary arteries in rest conditions (Hozumi et al., 1998). These flow conditions correspond to a mean Reynolds number ($Re = \bar{U}d/\nu$) of 88 and 122 , respectively, and Womersley number ($\alpha = d\sqrt{\omega/\nu}/2$) $= 1.88$, where $\omega = 2\pi HR/60$ is the angular frequency of the pulsatile flow and d is the artery diameter.

The results of grid refinement for both the idealized and physiological models are described in the Appendix. For the idealized model, simulations are performed for both steady and pulsatile flows with two normal mean flow rate conditions, $Q_n = 50$ and 69 (ml/min), and area stenosis 50 , 60 , 70 and 80% . The simulations provide the pressure, velocity, and contrast agent concentration distributions for the modeled coronary arteries. The concentration in the artery is measured at the end of simulation time (10 second) when the AIF reaches its peak and this mimics the typical CCTA acquisition protocol. For example, these fields are shown in Figure 3-6. for the case of steady flow, $Q_n = 50$ ml/min and area constriction 70% . One can see a significant pressure drop across the stenosis and high velocity magnitudes through the stenosis.

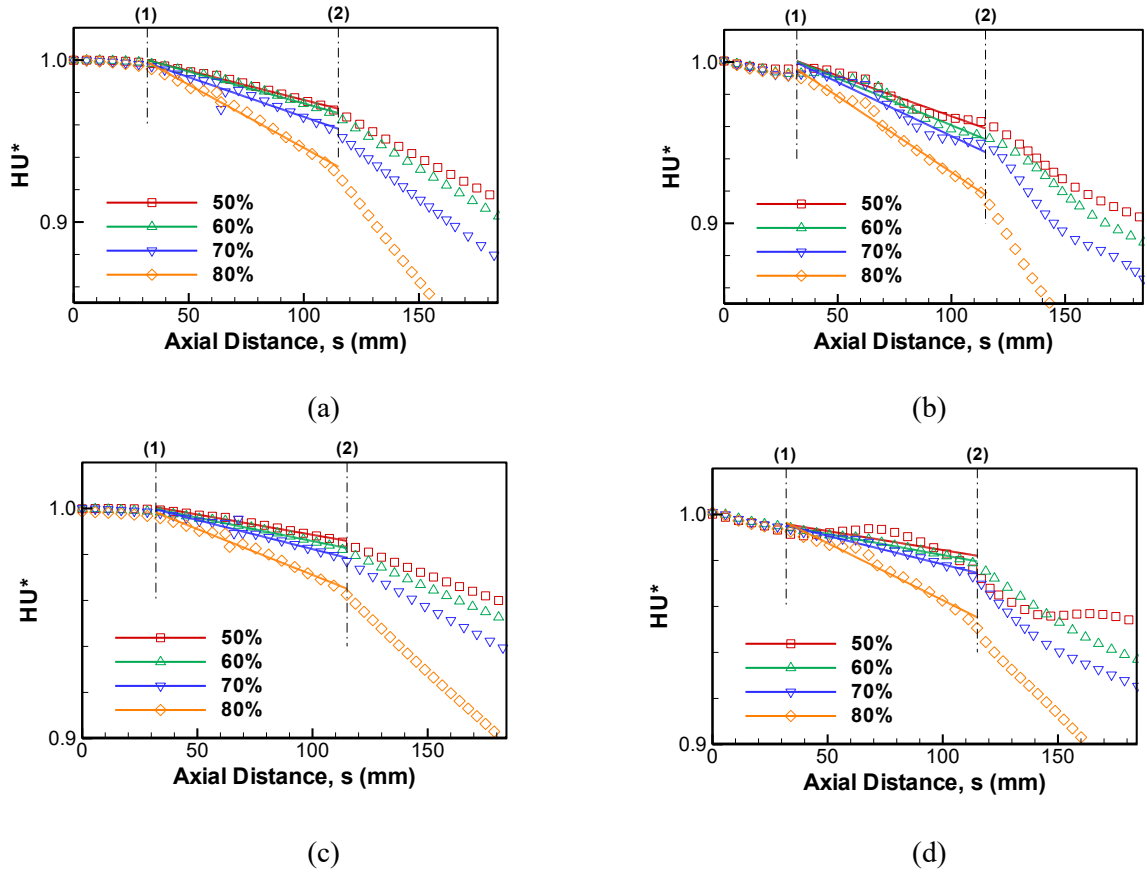
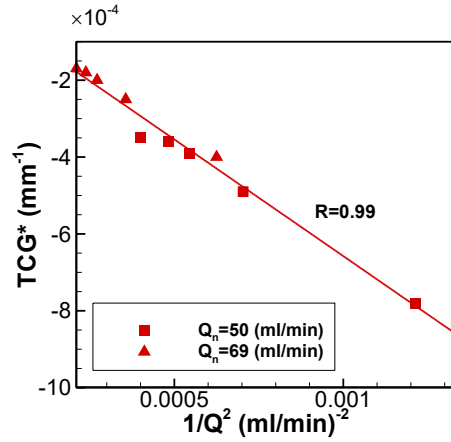


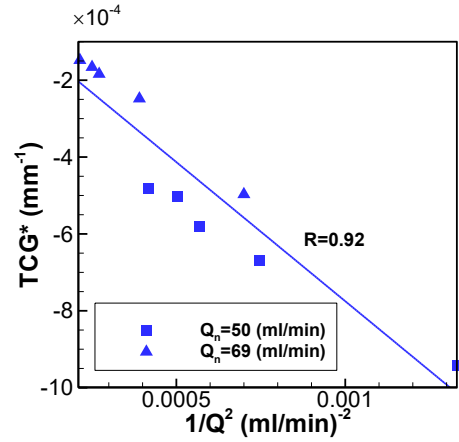
Figure 3-7. Normalized transluminal attenuation profiles along the axial direction of main arterial segment for (a) steady flow with $Q_n=50$ (ml/min) ($P_A = 3$, $P_B=0$ mmHg), (b) pulsatile flow with $Q_n=50$ (ml/min) ($P_A = 3$, $P_B=2.7$ mmHg), (c) steady flow with $Q_n=69$ (ml/min) ($P_A=4.5$, $P_B=0$ mmHg), and (d) pulsatile flow with $Q_n=69$ (ml/min) ($P_A=4.5$, $P_B=4.05$ mmHg). (1) and (2) indicate the locations of bifurcations shown in Fig 3. The attenuation profiles along the stenosed section (between (1)-(2)) are fitted by the linear function; $a \cdot s + b$ and the slope a represents the normalized TCG (TCG*). All the results are for the idealized model at the peak of AIF and the percentage refers to different area stenosis levels.

Figure 3-7 shows the transluminal variation of HU^* for steady and pulsatile flow cases with normal mean flow rates, $Q_n=50$ and $Q_n=69$ (ml/min). All these simulations are performed with $T_d=10$ (sec). In these plots section (1) and (2) indicate the location of arterial bifurcations and this divides the main artery into three segments (proximal to first bifurcation, distal to first bifurcation and distal to downstream bifurcation) and results with steady flow show a characteristic piecewise linear attenuation in each of these three

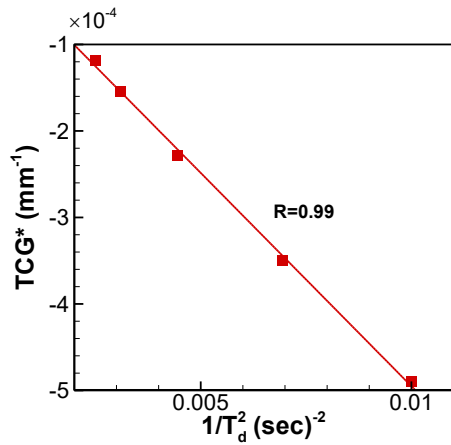
segments of the artery. For the pulsatile flow results, a wave-like variation is superposed on the linear distribution of attenuation. It is observed, however, that the magnitude of the attenuation gradient increases constriction size in all segments of the artery.



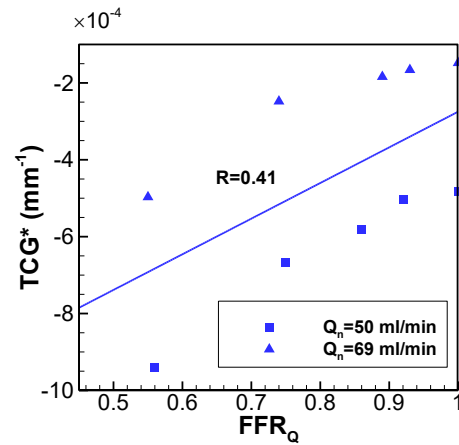
(a)



(b)



(c)



(d)

Figure 3-8. Correlation between (a) TCG and the inverse square of flow rate ($1/Q^2$) for steady flow, (b) for pulsatile flow, (b) TCG and the inverse square of bolus time, ($1/T_d^2$) for 70% stenosis and $Q_n=50$ ml/min, steady flow (d) TCG* and FFR_Q for pulsatile flow for the idealized model.

Values of TCG^* are estimated for the intermediate segment of the artery (segment that lies between points (1) and (2) denoted in Figure 3-7 by linear regression as described in the methods section, and Figures 6A and 6B show the variation of TCG^* with area constriction for the steady and pulsatile flows with two different mean flow rate conditions. We note that while the magnitude of TCG^* does increase with increasing constriction, the value of TCG^* also depends on the flow rate conditions and decreases in magnitude as the flow rate increases.

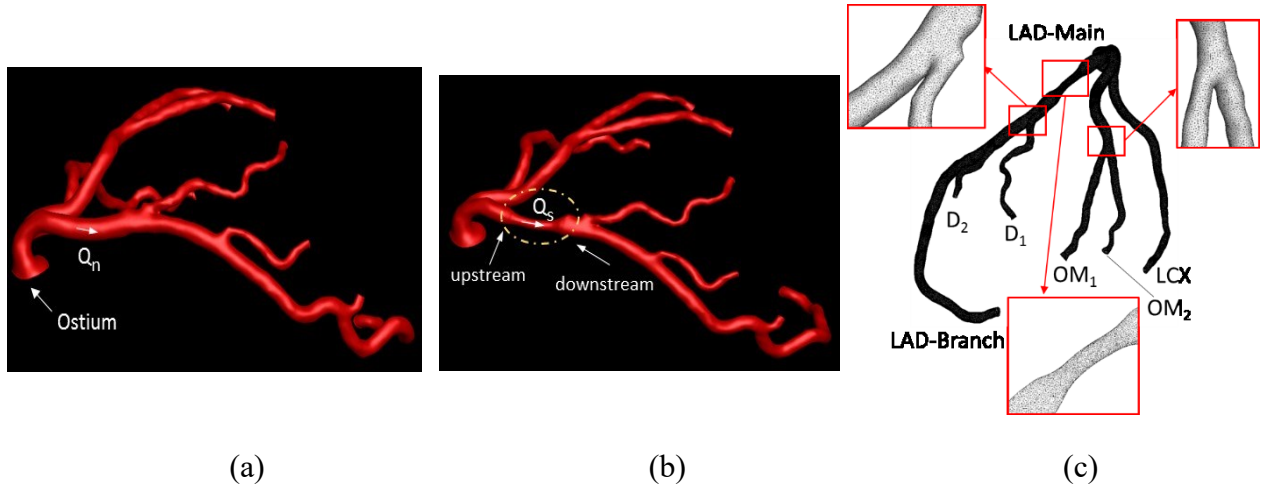


Figure 3-9. (a) 3-D model of a patient specific coronary artery for the normal (unstenosed) case. (b) Model of the artery with 70% stenosis. (c) Computational meshes employed in the various segments of the model.

Analytical investigation of TCG formation in Eq. (3-11) suggests the relations; $TCG^* \sim 1/Q^2$ and $TCG^* \sim 1/T_d^2$. These correlations are examined in Figure 3-8 for the current simulation results. Figure 3-8a. and Figure 3-8b show that TCG^* has a strong ($R > 0.92$) linear relationship with $1/Q^2$ for both steady and pulsatile flows. In order to assess the effect of T_d , we performed additional simulations for 70% stenosis, $Q_n = 50$ ml/min with T_d varying from 10 to 20 (sec) in the steady flow case. The results are plotted in Figure 3-8c, which indicates a clear linear relationship between TCG^* and $1/T_d^2$ ($R = 0.99$). Thus, the results

shown in Figure 3-8 seem to verify our hypothesis on the mechanism of TCG generation and the expression, Eq. (3-11). It is interesting to note that though Eq. (3-11) has been derived for the idealized steady pipe flow, the correlation between TCG and the coronary flow rate, Q still holds for the unsteady pulsatile flow through a relatively complex model of a coronary arteries. Figure 3-8d show plots of TCG^* versus FFR_Q for both flow rate conditions and it is noted that the magnitude of TCG^* decreases with increasing FFR_Q . However, the correlation between TCG^* and FFR_Q is significantly affected by the flow rate condition and is relatively poor ($R=0.41$).

3.3.2. Physiological Model Based on Coronary CT Angiography

From the previous section, the correlation between the inverse of flow rate squared and TCG^* is clear. To prove that the same mechanism holds for a more realistic model, the same steady computation has been performed for the normal case and 70% stenosis. The normal case geometry (Figure 3-9) has been generated from a patient specific data from CTA images and a 70% stenosis (Figure 3-9b) has been created manually using the normal geometry to compare the two cases. There were no regions of calcification in the artery of interest for this subject, thereby enabling acquisition of a high-quality image throughout the vessel of interest. The study has been modeled such that the mean flow rate through LCA matches the stress condition in clinical measurements. Therefore by choosing $PA=3.0$ mmHg, the mean flow rate in LCA will be $Q_n=375$ (ml/min) which is within the range of measured values of left coronary arteries (Hozumi et al., 1998). The mean flow velocity is $\bar{U}=25.1$ (cm/sec) which would correspond to the mean Reynolds number $Re = \bar{U}d / \nu = 454$.

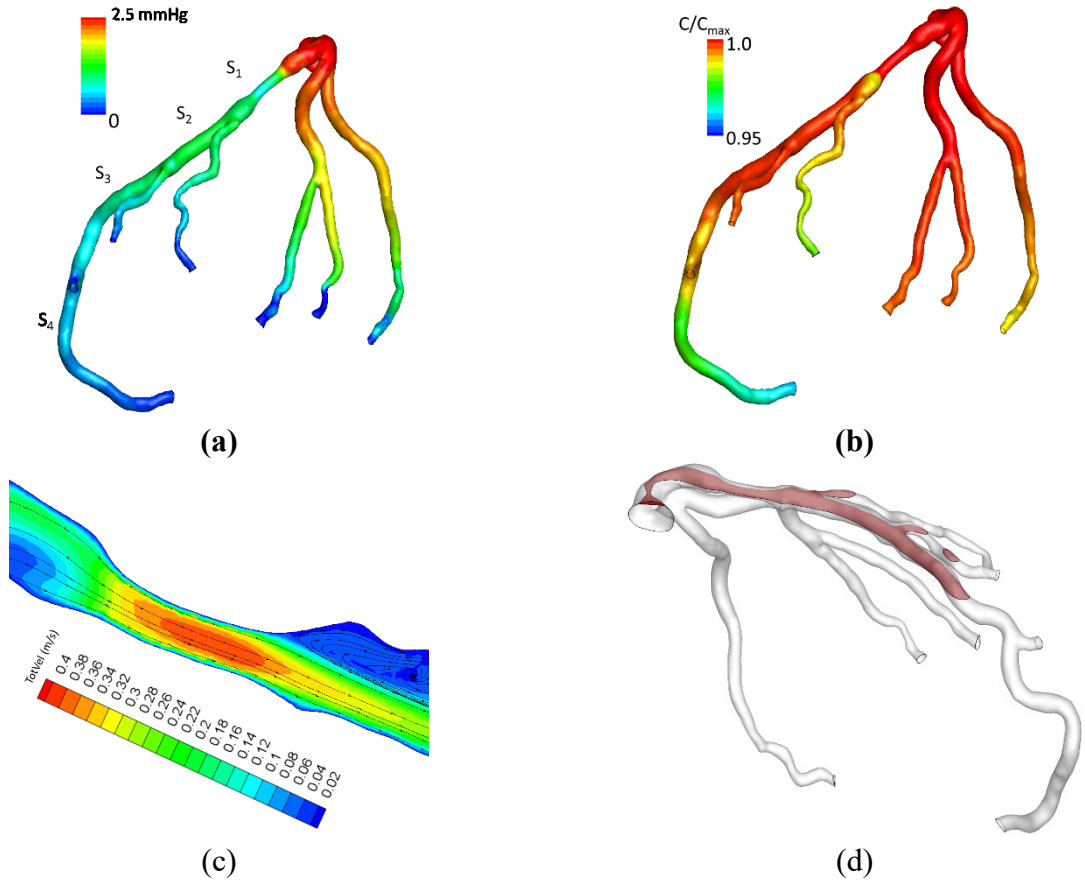


Figure 3-10. Patient specific computational results: Pressure (a), normalized contrast agent concentration (C/C_{max}) for the $Q_n=375$ ml/min case with a 70% area constriction. (b) and Velocity magnitude and streamlines in the stenosed region (c) cross sectional plane in which velocity contour in (d) is shown. The segmentations S1-S4 are segments of the main LAD before each branch.

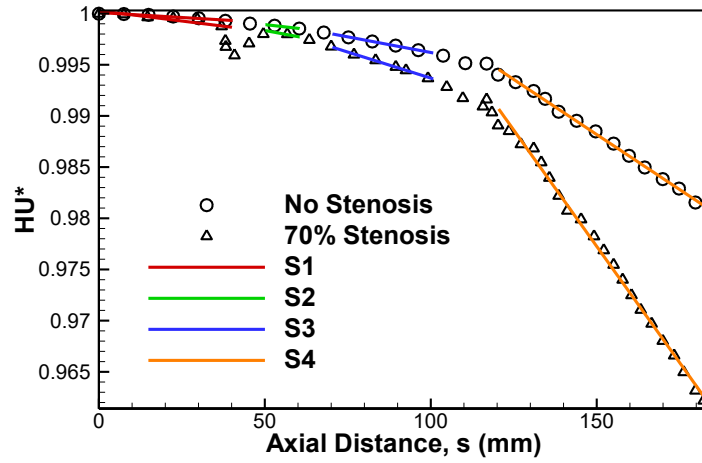
Figure 3-10 provides the simulation results for the pressure, velocity, and contrast agent concentration distribution for the mentioned flow rate of $Q_n=375$ (ml/min) and the area constriction of 70%. As expected, a pattern similar to the idealized case can be observed in the patient derived model which includes a significant pressure drop across the stenosis along with high velocity magnitudes through the stenosis. Figure 3-11a shows the transluminal contrast agent concentration HU^* for both the no-stenosis and 70% stenosis cases where the section S1-S4 has been defined along the main LAD before each branch point (Figure 3-10a). The values of TCG* are estimated as described earlier in the paper.

Based on the analytical relation between TCG* and the flow rate Q_{TAFE} , Eq. (3-12), the flow rates were estimated. Figure 3-11b demonstrates a strong correlation with an $R^2=0.98$ between the flow rate estimate by TAFE and the one obtained in the CFD calculation, for both the normal and 70% area stenosis cases for different sections of S_1 to S_4 .

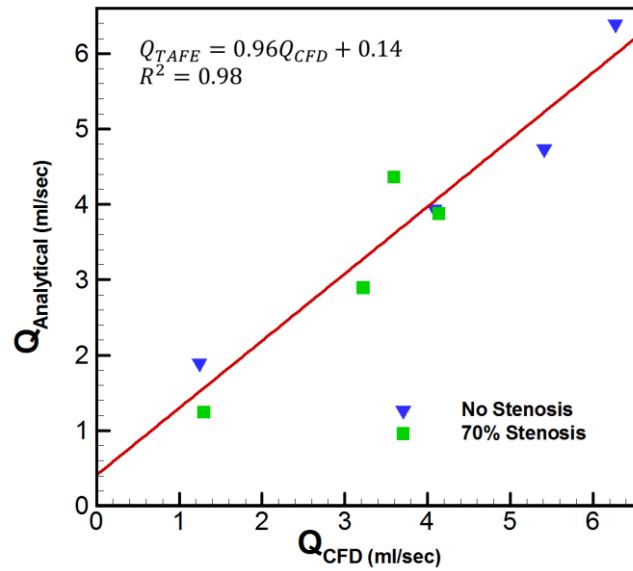
3.4. DISCUSSION

In this paper, the mechanism for the generation of contrast agent gradients in coronary arteries observed in cardiac CT has been investigated via computational fluid dynamics simulation and the analysis of the convection-diffusion equation. The current simulations of blood flow and contrast agent dispersion in models of stenosed coronary arteries show that TCG is measurably higher in arteries with a constriction and that TCG is correlated with coronary flow velocity, which in these models, is associated with different stenotic severities.

Although CFD has its own limitation associated with modeling and discretization errors, the exclusion of imaging artifacts and the capability to precisely control the boundary conditions and other features (e.g., arterial geometry, trans-arterial pressure drop and arterial input function) in the current modeling study allows us to suggest that TCG does indeed encode information that is intrinsically related to coronary flow. The analysis of the convection-diffusion equation for the contrast agent also provides insight into the mechanism responsible for TCG.



(a)



(b)

Figure 3-11. Patient specific normalized transluminal attenuation profiles along the axial direction of main arterial segment in LAD (steady flow) with PA=3 and PB=0 mmHg. (a) Correlation between CFD calculation of flow rate and TAFE calculation of the flow rate in the no-stenosis (normal) and 70% area stenosis cases (b).

More specifically, axial or transluminal varying contrast agent concentration is induced by the advection of the time-varying contrast agent bolus that enters at the coronary ostium. Given the typical temporal profile of the arterial input function and the acquisition of the image at or near the time corresponding to maximum enhancement at the

ostium, this necessarily implies that the contrast agent concentration imaged at this time-instance will show a decrease from the ostium to the distal segment of the artery.

The analysis also suggests that the flow velocity in the artery will clearly affect the overall gradient in the contrast agent concentration; a higher velocity will tend to “stretch” (and therefore decrease) the contrast agent gradient whereas a lower flow velocity will tend to steepen (and increase) the gradient. Similarly, for longer T_d , the contrast agent gradient is stretched further, thus TCG decreases. This is confirmed quantitatively by the strong correlation between TCG and the coronary flow rate ($TCG^* \propto 1/Q^2$) as well as between TCG and the bolus duration ($TCG^* \propto 1/T_d^2$) that are suggested in Eq. (3-11). We reiterate here that a different fit to the bolus (such as for instance, linear with time) would lead to a different correlation but not change the fundamental physical mechanisms hypothesized here.

The higher TCG* magnitude for higher area-stenosis is therefore due to the fact that for a given axial pressure drop, increase in constriction size increases flow resistance, and reduces the flow rate, which is correlated with a higher gradient. This issue will be discussed later in this section when describing the correlation between TCG* and FFR. The mechanism also explains the increase in the gradient at the two bifurcations evident in Figure 3-7; each bifurcation siphons flow away, thereby reducing the flow rate through the main branch and this leads to a steepening of the attenuation gradient distal to the bifurcation.

It is noted that since the model adopted here does not account for the microvascular resistance, which is dominant during physiologic rest conditions, the velocity drop associated with the area reduction for a given stenosis is significantly exaggerated here. It

is well known that significant reductions in resting coronary flow rates only occur for very severe ($> 95\%$ area) stenoses and that for less severe lesions, the reductions in rate-of-flow are quite small (Gould, Lipscomb, & Hamilton, 1974). Thus, the current results should not be taken to imply that TCG or related contrast information could be used to identify and/or stratify the reductions in flow-rates associated with intermediate stenoses. Rather, the current results primarily point to the causal relationship between TCG and flow rates.

The dependency of the measured TCG on the arterial input function has significant implications for *in-vivo* measurement of TCG. In most studies to date (Choi et al., 2011, 2012; Chow et al., 2011; Steigner et al., 2010) no particular attention has been given to controlling (or for that matter, even recording) the arterial input function. It is clear from our simulations that the value of TCG is very much dependent on the duration of bolus buildup in the coronary ostium ($TCG^* \sim 1/T_d^2$), and analysis also indicates that it is also dependent on the AIF profile (see Eq. 3-10). Thus, a raw value of TCG that does not account for (or compensate for) the duration of the arterial input function is expected to have relatively low prognostic value. Equation (3-11) also indicates that the precise value of TCG is affected by the cross-sectional area, A and the volume of arterial segment up to the position where the measurements are made. Lack of compensation for these additional factors is likely to further decrease the correlation between TCG and coronary flow measured in-vivo. It is important to note that as per Eq. (3-11), the axial variation of cross-sectional area (i.e. area gradient, $dA(s)/ds$) does not play a role in the TCG formation.

The data obtained from the current simulation show that while TCG is monotonically correlated with FFR_Q the overall correlation between the two is low ($R=0.41$). However, even with a high degree of control of the AIF and the absence of

imaging artifacts, the correlation between TCG and FFR is confounded by the baseline flow conditions in the artery. Note that there are a wide variety of factors that can affect the baseline flow rate through the coronary arteries of a patient which include (but are not limited to) overall cardiac health and medication (such as adenosine). All of these differences will be reflected in the TCG value (which encoded for flow velocity) but not in the FFR. All of the above analysis underscores the difficulty of correlating TCG to functional measures of stenoses such as FFR, and might explain the moderate to poor correlation ($R=0.39-0.43$) between the attenuation gradient and FFR reported in the previous in-vivo studies(Wong et al., 2013). In addition to the confounding effects of the arterial input function and imaging artifacts, this correlation is highly affected by the flow rate conditions, which may vary significantly from patient to patient.

The coronary artery models used in the current study are well suited for the fundamental analysis carried out here but they have a number of potential limitations. First, the use of a prescribed pressure drop across the vessel and with no capillary resistance introduced at the vessel outlet is not a precise representation of the physiological situation. In particular, this tends to amplify the effect of the stenosis on the flow rate and FFR, and this is something that is observed in the data (see Figure 3-8). However, this should not affect the primary objective and observation of the study, which is that TCG is inversely related with the effect that vessel stenosis has on the flow rate. Second, the shape of the stenoses are generated via a parametric formula and do not correspond to a naturally occurring lesions. Third, the arterial input function applied at the coronary ostium of the current model (see Figure 3-9) is actually based on measurements in the mid descending aorta. While there will be some differences in the contrast agent buildup at the two

locations, we do however expect that the two profile shapes and trends would be quite similar. Nevertheless, this issue needs to be investigated in a future study. Fourth, in the cases of presence of any imaging artifacts such as temporal and spatial resolutions and calcification or stents inside the diseased vessel, TCG will get affected and hence the estimated flow rate as well. One way to eliminate this artifact is to eliminate the segment with calcification or stent from TCG measurements; this is the subject of ongoing studies. Finally, the effect of a physiological coronary flow waveform and the prescribed pressure on the attenuation function and TCG is currently being studied and these results will be reported in the future.

It is also useful to discuss a seeming discrepancy between our simulation results and the TCG measured in-vivo: our simulations show only a 2-15% drop of the normalized HU (HU^*) over the entire length of the vessel, whereas the clinical example (Fig. 1) shows about a 75% drop. As indicated in Eqs. (3-9) and (3-10), the overall drop of HU^* over the vessel depends directly on the temporal change of HU in the AIF (or dC/dt), which can vary significantly with the precise shape of the AIF as well as the time-point in the AIF when the CT image is acquired. For example, in the AIF shown in Figure 3-2a, the rate of change near the AIF maximum (where the current analysis is done) is about 5 HU/sec while the maximum (in the middle of AIF) is about 30 HU/sec. Thus, a change in the timing of the acquisition could create a six-fold or more increase in the magnitude of the measured TCG. In this regard, it is noted that past studies have not appreciated this connection between AIF and TCG, and the current analysis provides a physical, as well as mathematical basis for such insights into TCG. In addition to the above factors, imaging artifacts in CT imaging (which are not included in the current computational model),

particularly partial-volume averaging (PVA) effects, also contribute significantly to the measured TCG in the vessels. The relative contribution of PVA to TCG depends on a number of factors including scanner resolution (pixels per diameter), the coronary flow velocity and vessel taper, and in some cases, might provide a dominant contribution to TCG. However, we have recently developed mathematical formulation to correct TCG for PVA effects, and the application of this formulation to CCTA data will be presented in a future paper.

In summary, while all of the above simplifications and assumptions are expected to affect the precise numerical value of TCG, we do not expect them to alter the basic mechanism that has been put forth by the current study: that transluminal contrast gradients exhibit the effects of the advection of the AIF into the artery and they encode the coronary flow velocity. This basic mechanism has been discussed and confirmed in recent clinical and preclinical studies (George et al., 2014; Lardo, Rahsepar, Seo, Eslami, Korley, George, et al., 2015; Richard T. George, Amir Ali Rahsepar, Jung-Hee Seo, Parastou Eslami & Rajat Mittal, 2014).

3.5. SUMMARY

Computational modeling of flow and contrast dispersion has been used to explore the hypothesis that transluminal contrast gradients are formed due to the advection of the time-varying contrast bolus that arrives at the coronary ostium. According to this hypothesis, a higher velocity in the coronary vessel will tend to “stretch” (and therefore decrease) the contrast agent gradient whereas a lower flow velocity will tend to steepen (and increase) the gradient. Simulations for both an idealized model as well as a physiologically realistic coronary artery model confirm the above hypothesis and show that these contrast gradients

encode for the coronary flow velocity. All other conditions being the same, our mathematical analysis and simulations show that a larger stenotic blockage reduces flow velocity which increases the gradient, and might explain the correlations between stenotic severity and TCG observed in previous studies. The mathematical analysis of dispersion also reveals that the bolus duration is a key parameter that relates these gradients to the flow velocity. The mathematical formulae connecting TCG to flow velocity derived here, represent a novel approach for non-invasive estimation of coronary flow velocity from CT angiography and should also facilitate investigations and analyses of these gradients that are grounded in the physics of flow and dispersion.

CHAPTER 4: ASSESSMENT OF TAFE VIA CARDIAC CT COMPATIBLE PHANTOM EXPERIMENTS

4.1. INTRODUCTION

In Chapter 3, we explained the mechanism of TCG and introduced a new method called Transluminal Attenuation Flow Encoding (TAFE) for quantifying the flow velocity and flow rate in a coronary vessel using information from contrast enhanced cardiac CT imaging. The flow physics underlying this method has been established and validated using computational fluid dynamics (CFD) (Chapter 3 and Eslami et al., 2015). Furthermore, preliminary retrospective estimation of coronary flow rates using TAFE existing cardiac CT images for a cohort of patients has also shown promising results (Lardo, Rahsepar, Seo, Eslami, Korley, Kishi, et al., 2015) with results indicating a high degree of correlation between expected and estimated (via TAFE) flow rates. However, these studies as well as more recent clinical and animal studies (Abd & George, 2015) indicate that the absolute values of flow velocity obtained using TAFE, underestimate (sometimes significantly) the expected values.

Consider Figure 4-1., which shows the results of a preclinical study of the TAFE to predict absolute total coronary blood flow (CBF) in dogs. A total of 9 animals were used (5 cases with 50% stenosis and 4 cases with myocardiac infarction). CTA imaging was conducted using a 256 detector-row CT scanner (Toshiba Medical Systems Corporation, Otawara, Japan). Immediately following CT imaging, radioactive microspheres were injected via the

left atrial catheter in the stenosis model in and via a left ventricular pigtail catheter in the MI model with simultaneous blood sampling from the descending aorta at a rate of 2.1 ml/min. Animals were then transported to the laboratory. Following euthanasia, the heart was removed and myocardial samples from the entire heart were excised and submitted for microsphere counting and absolute myocardial blood flow calculations using methods described in (George et al., 2006)

When TAFE based CBF estimates were compared to microsphere based measurement (Figure 4-1, it was found that while TAFE gave an excellent linear correlation with the microsphere measurements, it underpredicted the absolute value of CBF. Thus, while this linear correlation provides very strong support for the mathematical formulation underlying TAFE, the underprediction in the absolute values indicates corrections needed . Given however that the CFD validation indicated a very accurate prediction of flow velocity from TAFE, it was thought that factors associated with CT image acquisition and processing, which are not accounted for in the CFD model, might be responsible for this under-prediction in the clinical and animals studies.

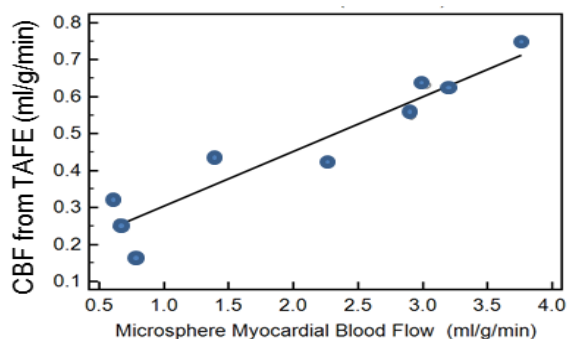


Figure 4-1 Retrospective evaluation of TAFE for nine canine models of ischemic heart disease were prepared and underwent CT imaging and microsphere measurements of myocardial blood flow (MBF). While TAFE correlated very well with CBF, it under-predicts the magnitude of CBF due to partial volume averaging (PVA) effects. (from Lardo et al. 2015)

4.1.1. Partial Volume Averaging

Since, TAFE is based on CT imaging, it is subject to errors associated with imaging artifacts. A key imaging-related artifact that affects TAFE is partial-volume-averaging (PVA). In CT angiography, the spatial resolution of the CT image is limited by the voxel size of the scanner, which for a modern multi-detector CT scanner is about $0.5\text{mm} \times 0.5\text{mm} \times 0.5\text{mm}$ (Hsiao, Rybicki, & Steigner, 2010). This implies for instance that the coronary lumen of a 2 mm diameter section of a coronary artery would be resolved by only about 12 voxels (See Figure 4-2). The voxels at the outer edges of the lumen are partially located outside the lumen leading to errors in the estimation of the average attenuation (HU) factor at any given cross-section; this error is termed as the partial volume-averaging effect.

Thus, for a any vessel in body, because of its natural tapering, the affect of PVA is even more pronouced as the lumen area reductin down the vessel will have lower number of voxels covering the cross-sectional area . Hence, the tapering will generate spurious and artificial gradients that needs to be corrected.

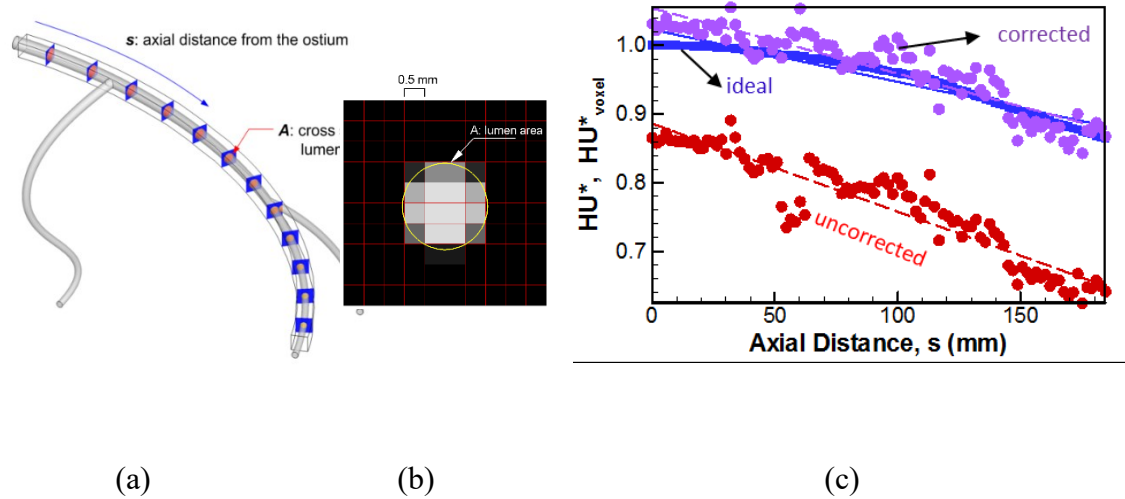


Figure 4-2. (a) Examination of partial volume averaging effects using computational models. A coronary artery model employed and planes of data extracted from model. (b) An example of the cross-sectional view of contrast concentration computed from our simulations where the arterial diameter is about 2 mm. A voxel grid of 0.5 mm is superposed on the plot and plot clearly shows how finite resolution affects the intensity across the lumen. (c) Comparison ideal (infinite resolution), actual (0.5 mm voxel), and corrected (using correction formula) attenuation profile. Note that after the PVA

We have conducted a computational and theoretical study of PVA for a tapering vessel (see Figure 4-2c) and found that PVA leads to an additional increase in the contrast gradient and also produces stochastic spatial variations in the measured contrast distribution. The PVA associated increase in gradient would lead to TAFE underpredicting the flow rate and our analysis indicates that correction for this effect would enable TAFE to more accurately predict absolute flow rates.

The investigation and assessment of PVA and other imaging artifacts on TAFE therefore established the need to additional tests and led to the TAFE experiments with cardiac CT compatible phantoms, which are described in the current Chapter. The objective of these phantom experiments are as follows:

- 1) Assess the accuracy of TAFE based velocity estimates in a controlled experiment that incorporates CT imaging and reconstruction related features.
- 2) Determine the key factors that lead to underestimation of the TAFE-based flow velocity prediction.
- 3) Use experiments to explore corrections for the TAFE-based underestimation of flow velocity.

4.2. MATERIALS & METHODS

4.2.1. Theory

The complete derivation of TAFE for single vessel and branched network is shown in Chapter 3 and Eslami et al., 2015. Briefly, the analytical formulation of TAFE comes from two main equations of Navier-Stokes for incompressible flows (Eq. (4-1)) modeling the blood and convection-diffusion equation (Eq. (4-2)) to model the contrast dispersion.

$$\frac{\partial \mathbf{U}}{\partial t} + (\mathbf{U} \cdot \nabla) \mathbf{U} + \frac{\nabla P}{\rho} = \nu \nabla^2 \mathbf{U}, \quad \nabla \cdot \mathbf{U} = 0 \quad (4-1)$$

$$\frac{\partial C}{\partial t} + (\mathbf{U} \cdot \nabla) C = D \nabla^2 C \quad (4-2)$$

With a few assumptions and simplifications such as unidirectional flow in the tube/vessel and convection dominant nature of the problem, the mean flowrate, Q_{TAFE} , through the vessel can be estimated using the TAFE equation (Eq. (4-3)):

$$Q_{TAFE} = \frac{\partial C / \partial t}{-\partial C / \partial V_{cum}(s)} \quad (4-3)$$

Where V_{cum} , is the cumulative volume of the vessel at the axial location, s , and can be found by $V_{cum}(s) = \sum A(s) \times s$. The numerator, $\frac{\partial C}{\partial t}$, can be found by taking instantaneous derivative of the time-density curve (TDC) or the arterial input function (AIF) of contrast at the ostium of the tube with the unites of [HU/s] (see Figure 4-3a). $\frac{\partial C}{\partial V_{cum}}$ is the same as volumetric TCG (TCG_V [HU/cm³]) and can be calculated by taking the derivative of contrast with respect to the cumulative volume down the vessel of interest corresponding to the same time point the time derivative is taken (see Figure 4-3b).

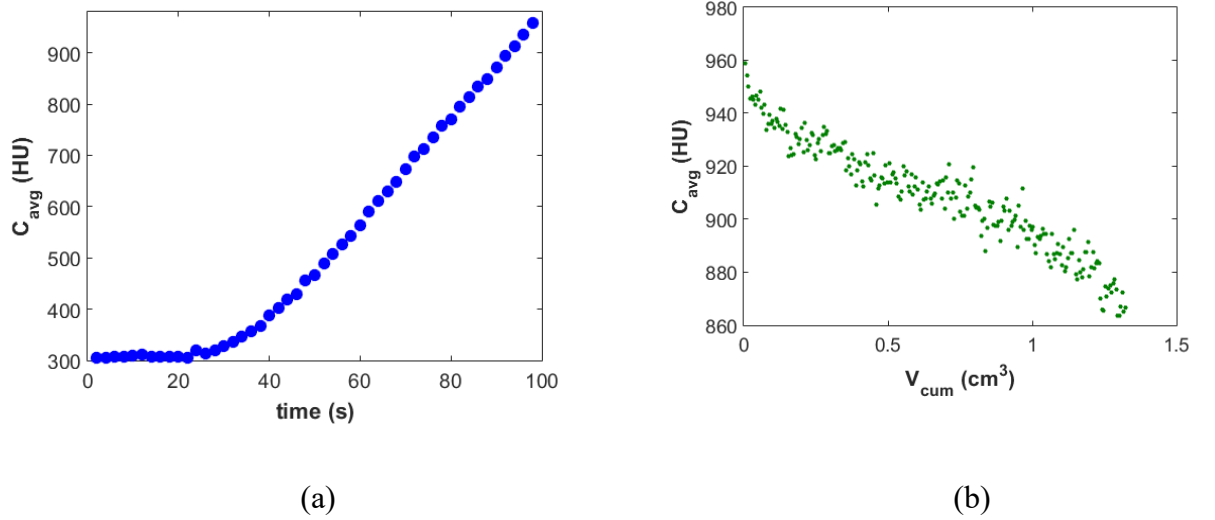


Figure 4-3. Examples of arterial input function (AIF) at the ostium of the phantom sampled at every 2 seconds (a) and contrast concentration vs. the cumulative volume (b) the slope of this figure is known to be volumetric transluminal contrast gradient (TCG).

4.2.2. Experimental Setup

To validate the analytical formulation described in section 4.2.1 and demonstrate that it is feasible to measure blood flowrate and velocity using TAFE, phantom measurements were performed with a custom-built CT-compatible phantom set-up. Figure 4-4 presents

the schematic of the experimental set-up with the components labeled. The pump used in the experiments is a steady Harvard Apparatus PHD 2000 Programmable Syringe Pump with a range of 0.0001 $\mu\text{l/hr}$ to 112 ml/min with an accuracy of 1% of the flowrate specified. Fluid is pushed out by the syringe goes through a mixing chamber which has a volume of 250 ml. This mixing chamber mimics the volume of the left and right ventricles where the contrast gets mixed with blood before entering the aortic root and coronary sinus. The mixing chamber is placed on top of a heated magnetic stirrer (kept at 37° C) and an “X” shape magnetic propeller mixes the incoming contrast with the G-W solution. The fully mixed solution then enters the coronary artery phantom (Figure 4-5b). Since, the phantom set-up is a closed system (without any outlets or leaking before flow enters the phantom) and there are no branches to the phantom, based on the law of mass conservation, the pump’s infusion rate (true pump flowrate) is the same as the flowrate through the phantom.

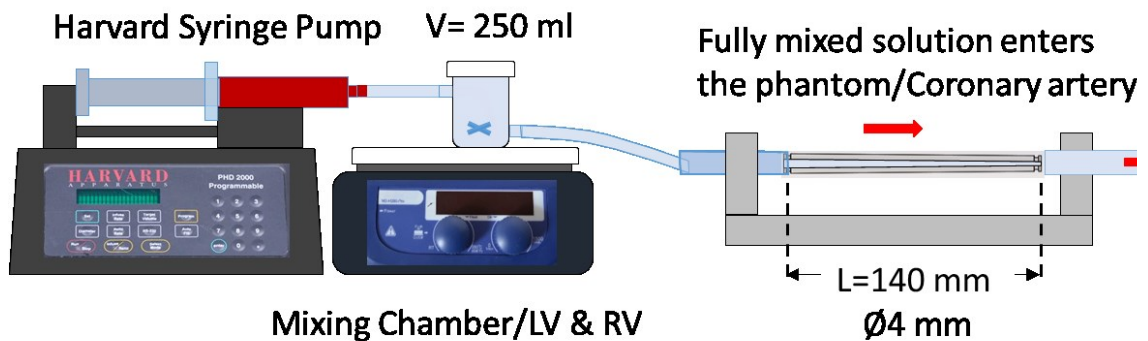


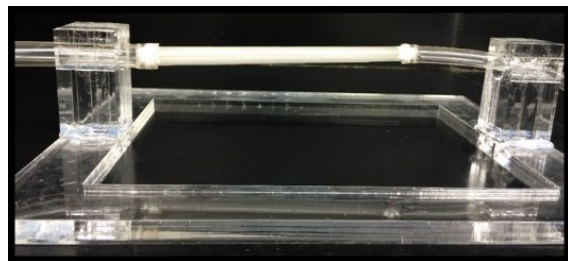
Figure 4-4. Illustrative overview of the phantom experiment set up. The contrast is infused into the system by first flowing through the mixing chamber located on a magnetic stirrer to mimic the chambers of left and right ventricle (LV and RV) and the fully mixed solution enters the phantom

The phantom set up is then placed in a 320-detector-row, Aquilion® ONE, a dynamic volume CT system scanner (Toshiba Medical Systems Corporation, Otawara, Japan) (Figure 4-5a) with a gantry rotation speed ranging from 350-375 micro seconds. Dynamic imaging was performed using the following parameters: gantry rotation time = 300 ms, detector collimation = 0.5 mm \times 320, tube voltage = 120 kV, tube current = 100 mA and scan time= 99 seconds.

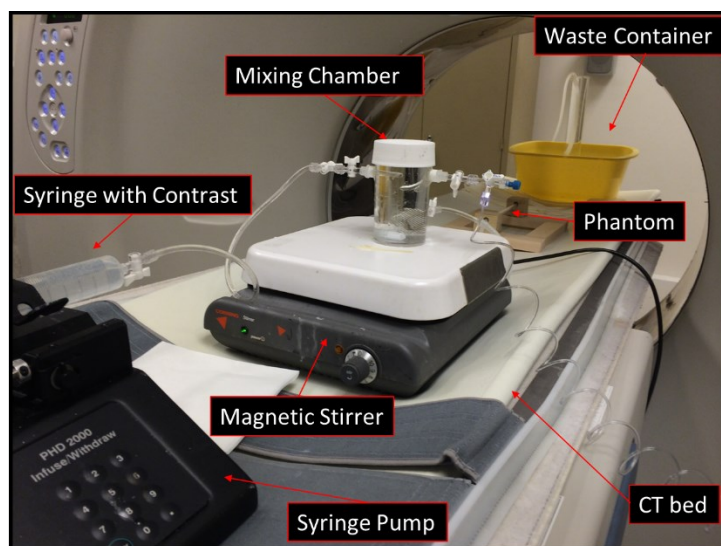
We used Omnipaque 240 mg (GE Healthcare) as the contrast agent for these experiments and this is a commonly used contrast agent for CT imaging. The choice of the fluid in the phantom is based on two the contrast is roughly equal to the density of blood and therefore the fluid used in considerations: the density of the phantom should match the density of the contrast; and the viscosity of the fluid should match the viscosity of blood in order to produce a flow state in the phantom that is, to the degree possible, dynamically similar to coronary vessels. To match the dynamic viscosity of blood at 37° C (4×10^{-3} [Pa.s]), a mixture of water and glycerin with the ratio of 70 to 30, respectively, was prepared. In addition to match the density of the contrast agent (~ 1.2 kg/m³), sea salt was added to the glycerin-water (G-W) solution. Both the contrast and G-W solution are kept in a warmer at 37° C prior to the experiment.



(a)



(b)



(c)

Figure 4-5 (a) Toshiba Aquilion One, 320 detector CT scanner used in the current study. (b): 3-D printed tapered phantom placed in the custom-built laser-cut holder. (c) Set up for flow phantom studies showing syringe pump, mixing chamber and magnetic stirrer and phantom.

To be able to custom build the phantom with specific size and shape, we used a 3-D printing machine with ABS (Acrylonitrile butadiene styrene) as the material and a mean wall attenuation of -40 HU. Two distinct but simple phantom were employed in the current study: a straight, single vessel phantom with an internal diameter of 0.4 cm and a length of 14 cm, and a tapered phantom of the same length and same inlet diameter but with a lumen taper of 8.1 degrees and an exit diameter of 0.2 cm. The diameter, length and tapering angle of the phantoms are chosen to have similar dimensions as the main branches in coronary arteries. The advantage of choosing to have a 3-D printed phantom was the material used no considerable attenuation and had minimal effect on the attenuation of G-W solution with contrast as they enter the phantom. In addition, 3-D printing is a fast and cost-effective way of creating a phantom for our use. However, the 3D printing machine available to us

did not have the desirable plate accuracy and resolution which resulted in thin plane resolution of 0.5 mm – approximately the CT resolution. The experiment is then performed in the following steps:

- Mixing chamber is filled with the G-W solution and carefully capped to avoid any air bubbles in the chamber while the 60 ml syringe is filled with the contrast.
- The phantom with the tubing get flushed out with the G-W solution to drive any residue of contrast from the previous experiment and any existing bubbles out of the system.
- CT table axial laser centerline is approximately set to be aligned with the phantom's centerline while the orthogonal laser centerlines are aligned with the edge of phantom holder
- The phantom is scanned in the sure-start process to ensure the alignment and adjusting the field of view
- All the connecting valves are set to be open, mixing chamber is turned on and the syringe pump is started
- The CT machine starts scanning while the contrast infuses the mixing chamber from the inlet and mixes with the G-W solution and enters the tubing at the outlet
- The contrast then enters the phantom after a few seconds and creates a bolus at the ostium.
- The scanning continues until either the maximum scanning time (99 s) reaches or the syringe runs out of contrast. The procedure is repeated for all the flow rates of interest.

4.2.3. Image Reconstruction

Dynamic volume images were reconstructed using temporal resolution of 500 ms and slice thickness of 0.5 mm with no overlap. The convolution kernel used for the image reconstructions was FC05 with sharper edge enhancement. It is well known that CT scanners use a variety of filtering kernels to refine and de-noise the raw image data that emerges from the scan. This filtering process can introduce imaging artifacts, reduce effective resolution and create errors in the TAFE-based flow velocity estimation. Our studies suggest that these filtering kernels might increase the effective pixel size by many folds and we did a series of studies to examine this effect. The FOV employed here generates a pixel size of 0.327mm and we therefore have approximately 18x18 pixels across the lumen of the 6mm, non-tapered silicon phantom. These series of experiments were performed for express understanding of the effect of different filtering kernels. Figure 4-6a and Figure 4-6b show the application of 6 different filter kernels to image reconstruction and it clear that despite a seemingly high pixel resolution of 18 pixels, the contrast concentration through the lumen is highly affected by the image reconstruction process. Based on this data, it was decided that the FC05 AIDR3D reconstruction kernel provides the best delineation of the lumen with the least noise artifact and the phantom flow studies employed this kernel.

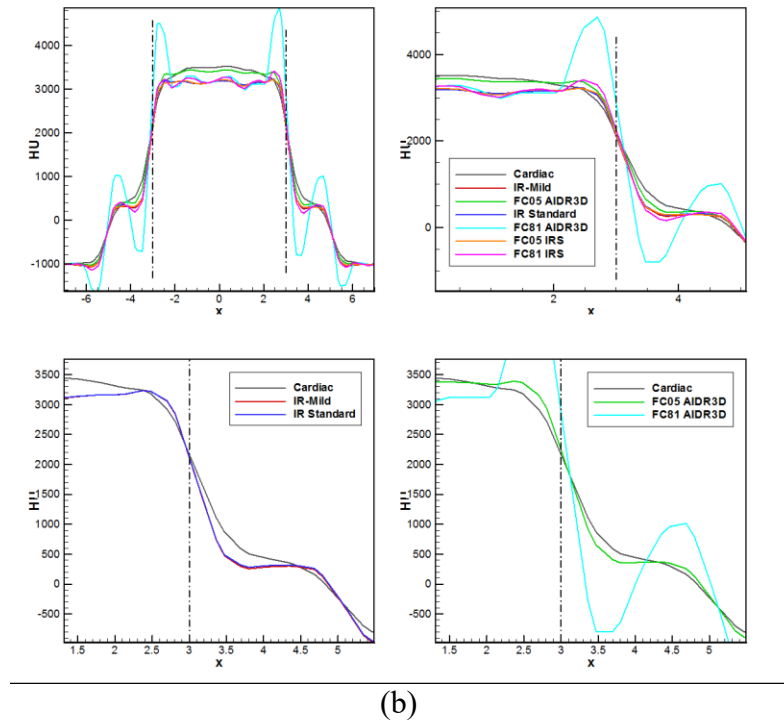
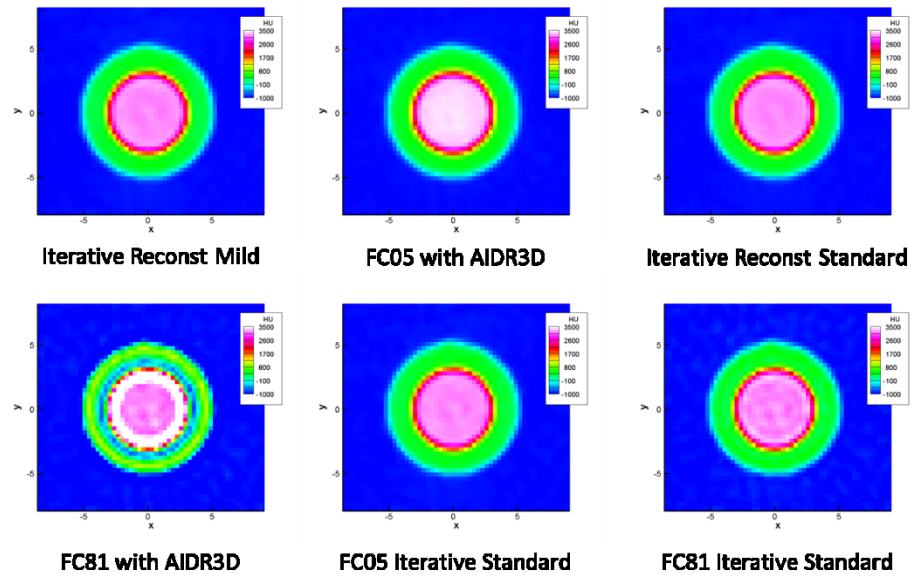


Figure 4-6. Effect of filter kernel on attenuation. (a) Sectional images for 6 different filter kernels. (b) Sectional profiles for 6 different filter kernels. C. HU values for various kernels. D. Gaussian filter model for the kernel.

4.2.4. Image Analysis and Phantom Segmentation

The dynamic volume images analysis was done using a custom written script (Matlab R2015a) and consisted of two steps: first was to extract the contrast attenuation at each cross section of the phantom in the axial direction for each time point resulting in transluminal contrast gradient curve and second was to extract the contrast attenuation at the ostium of the phantom for each time point resulting in the arterial input function. Initially, we employed a simple thresholding ($C_{thresh} = 0.4 C_{max}$) methodology in image segmentation. Hence, every pixel that has $C < C_{thresh}$ is assigned to have a value of 0 and then the center point of phantom (x_c and y_c) is determined by finding the “center of mass” based on pixel attenuation level by Eq. 4-4 where x_{ij} and y_{ij} are the locations of each pixel in the X- and Y-plane and C_{ij} is the attenuation level of contrast at that location.

$$x_c = \frac{\sum x_{ij} C_{ij}}{\sum C_{ij}}, y_c = \frac{\sum y_{ij} C_{ij}}{\sum C_{ij}} \quad (4-4)$$

To better segment the phantom and analyze the image, a more advanced methodology than thresholding was considered. The following flowchart (Figure 4-7) illustrates the steps taken for image segmentation. With the center point determined (Figure 4-8a) via Eq. 4-4, the edges of the lumen in phantom are found after sampling the original image by a new region of interest (ROI) of 60 x 60 pixels via the Canny edge detection methodology (Canny, 1986). This method uses two different thresholds (strong and weak) and includes the weak edges in the output only if they are connected to strong edges. Since our phantom was 3-D printed, the wall is intrinsically rough with roughness enhanced by formation of small bubbles during the curing process. The use of the Canny method was therefore appropriate to not confuse imaging noise with actual model

roughness. Subsequently, every pixel inside the detected edge is filled (assigned to have the value 1) by a simplified 1-D ray tracing method-a computer graphic technique for generating an image by tracing the path of light through pixels in an image plane (Appel, 1968). Next, the lumen area is corrected using the built-in function *activecontour* in Matlab with a predefined mask and 50 iterations. The active contour method used for segmentation is Chan and Vese's region-based energy model described in (Chan & Vese, 2001). Figure 4-8 represent a sample step by step cross sectional segmentation of a straight phantom where a sequential correction is demonstrated.

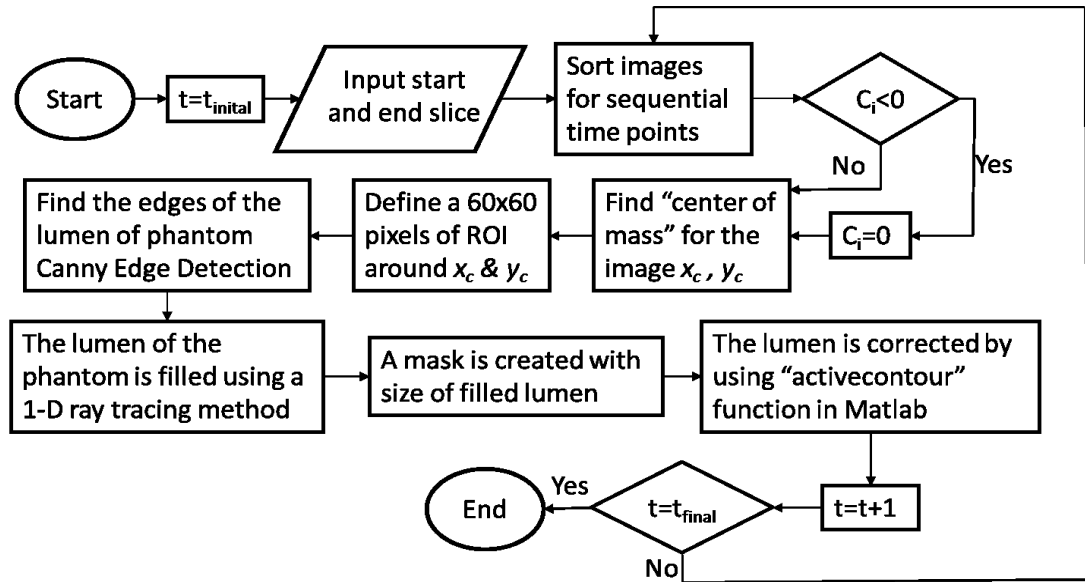


Figure 4-7. Flowchart of custom-written algorithm for segmentation of the phantom for each cross section of the phantom in a dynamic scan.

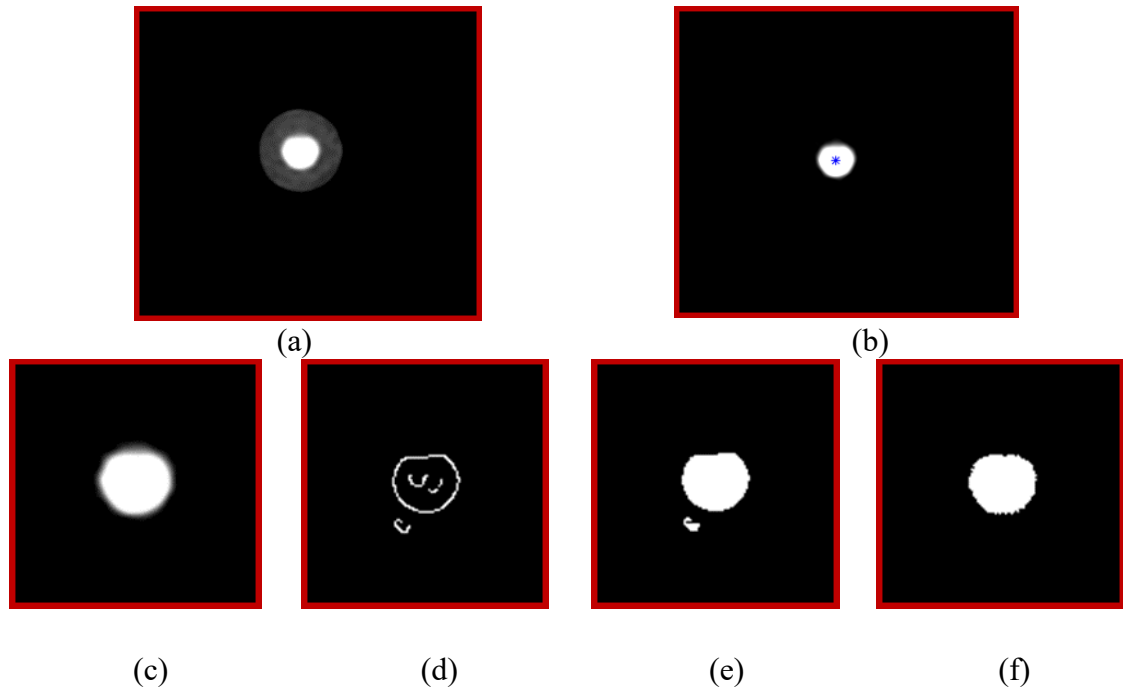


Figure 4-8 . Illustration view of segmentation of straight phantom. Original phantom cross-section with the wall included (a). Background and wall level sets are assigned to have zero value and the center point is calculated shown with the blue star (b). ROI is chosen to be a 60 x 60 pixel from the center point (c). Edge of the lumen is defined using the Canny edge-detection method (d). The lumen of phantom is filled based on the edge detected (e). The filled area is corrected using active contour method (f).

4.2.5. *TAFE* Analysis

With the phantom cross-sections segmented, the AIF can be extracted by estimating the mean attenuation level of the segmented cross-section at the ostium of the phantom at each time point. Figure 4-3a is a representative AIF measured at the ostium after segmentation.

Correspondingly, the volumetric transluminal contrast gradient can be extracted by plotting the mean concentration (attenuation level) of contrast at each cross section down the length of the phantom against the cumulative volume, V_{cum} . The instantaneous

derivative of contrast with respect to time, $\frac{\partial C}{\partial t}$, can be calculated by employing backward Euler finite difference method. However, since the data is noisy, $\frac{\partial C}{\partial t}$ is determined by finding piecewise linear regression of the AIF curve at every 5 seconds. Similarly, TCG_V is obtained by the linear fit (least squares) through the entire length of the phantom. As can be seen in Figure 4-9, the mean concentration of contrast is fairly noisy and the outliers are removed for the data points greater than 1.5 times the standard deviation ($C_{ij} > 1.5\sigma$). Transluminal contrast gradient curves of 5 time points for inlet flow rate of $Q_{inlet}=30$ ml/min in straight phantom is shown in Figure Figure 4-9 The contrast concentration level increases as time progresses due to the incoming bolus of contrast.

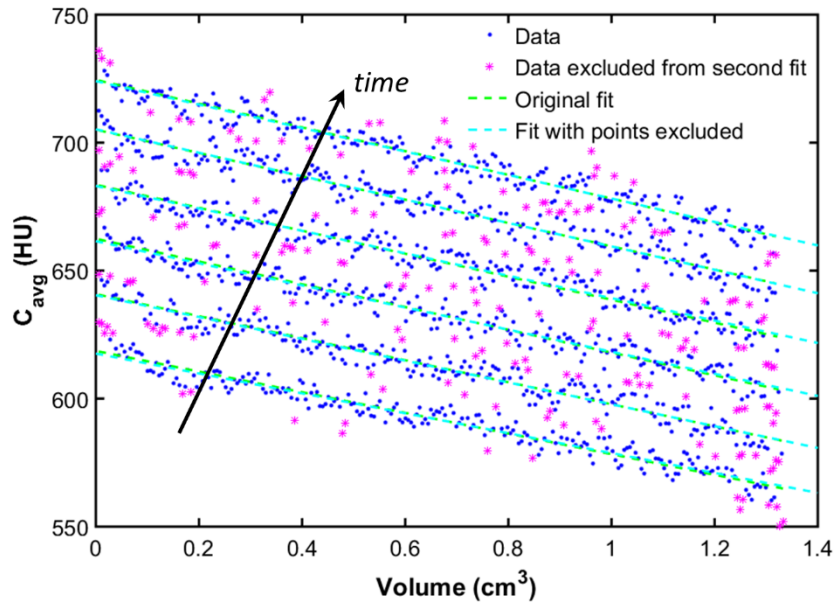


Figure 4-9. Transluminal contrast gradient curve for 5 consecutive time points where on the linear regression are shown in dashed lines including both original (in green) and the fit excluding the outlier data points shown with star markers (in blue).

4.2.5.1. Errors due to Flow Non-Uniformity

As pointed out before, PVA is expected to be a significant contributor to the under-prediction of flow rate by TAFE. However there are other features and factors that might also contribute to errors in the TAFE based estimates. As discussed in Section 4.2.1, an assumption is made in the TAFE analysis that the radial variation of the contrast at any axial location within the phantom is minimal; i.e. the contrast has a uniform profile across any cross-section. . However, as observed in Figure 4-10a and Figure 4-10b there is an apparent radial variation in the profile. There are two explanations for this observed phenomenon: the first is purely based on imaging artifacts which include PVA as well as any “filtering” of the data inherent in the image reconstruction. The second mechanisms for the appearance of the radial contrast concentration variations may be related to flow physics inherent to the experiment. It is expected that flow from the mixing chamber will develop a parabolic profile as it travels to the phantom. Thus, flow in the center of the phantom will move faster than the flow near the walls. Thus, at any given cross section, the contrast near the wall is associated with an earlier time in the AIF than the contrast in the center of the channel. Since the AIF is increasing over time, the contrast near the wall will therefore have a lower concentration than the contrast near the center. This will lower the average contrast concentration in a given cross-section and modify the TCG in the phantom. This in turn will affect the estimation of flow rate via TAFE. Figure 4-10d is a schematic illustrating the mentioned phenomena.

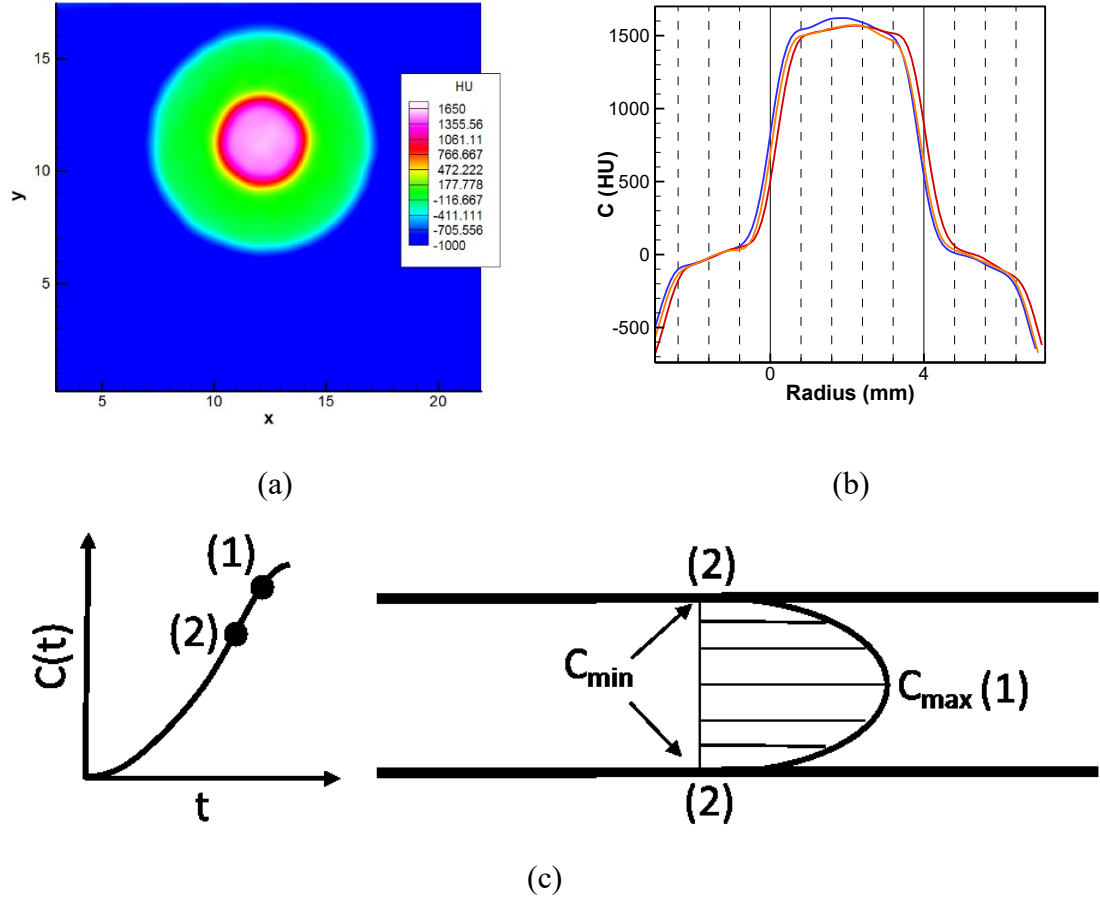


Figure 4-10. Contrast radial contour variation where the phantom wall and the air surrounding it is at 0 or negative (a). Contrast attenuation in HU vs. the radius of the phantom wall for 3 different cross-sections. The lumen radial profile is between radius values of 0 and 4 (b). .

To understand this non-uniform flow effect we consider a simple analysis of flow and contrast through the experiment: let $C_o(r, t) = C_{max}f(r)\frac{t}{T}$ be the concentration of contrast at the ostium of the phantom, where, C_{max} is the maximum concentration level at the cross section, and T is the total run time. Then, assuming a general form of velocity profile of $u(r) = U_{max}g(r)$, the concentration of the contrast at some location, s , downstream of phantom can be found as:

$$C(r, t, s) = C_{max}f(r)\frac{1}{T}\left(t - \frac{s}{u(r)}\right) \quad (4-5)$$

With some mathematical manipulation and substituting for $u(r)$, the cross-sectional averaged concentration is obtained as:

$$\bar{C}(s, t) = \int C(r, s, t) \frac{dA}{A} = \overline{C_{max}} \cdot \left(\frac{t - k \cdot s/\bar{U}}{T}\right) \quad (4-6)$$

where, A is the cross-sectional area, $\overline{C_{max}} = \int C_{max}f(r) \frac{dA}{A}$ and $\bar{U} = \int U_{max}g(r) \frac{dA}{A}$ and the correction factor, k , is defined as:

$$k = \frac{\int g(r)dA}{\int f(r)dA} \cdot \int \left(\frac{f(r)}{g(r)}\right) \frac{dA}{A} \quad (4-7)$$

Thus, TAFE formulation in Eq. 4-3 is modified to have the form of:

$$Q_{TAFE_{k_{corr}}} = k \cdot \frac{\partial C / \partial t}{-\partial C / \partial V_{cum}(s)} \quad (4-8)$$

Since, $f(r)$ is not known, CFD simulations have been employed to solve for k . Assuming a parabolic profile for the velocity with laminar flow entering the phantom, k was calculated for different flow velocity and phantom geometries. The CFD simulations were specifically done to mimic the flow in the phantom with the tubing connecting the mixing chamber to the phantom (Figure 4-11). The tubing here is 20 cm of straight pipe with diameter of 0.4 cm and the phantoms are each 14 cm in length. Similar to the experimental set-up, the phantom's inlet and outlet diameters are 0.4 cm for the straight phantom and with diameter of 0.4 cm at the inlet and a tapering angle of approximately 8.1 degrees, the tapered phantom outlet diameter becomes 0.2 cm.

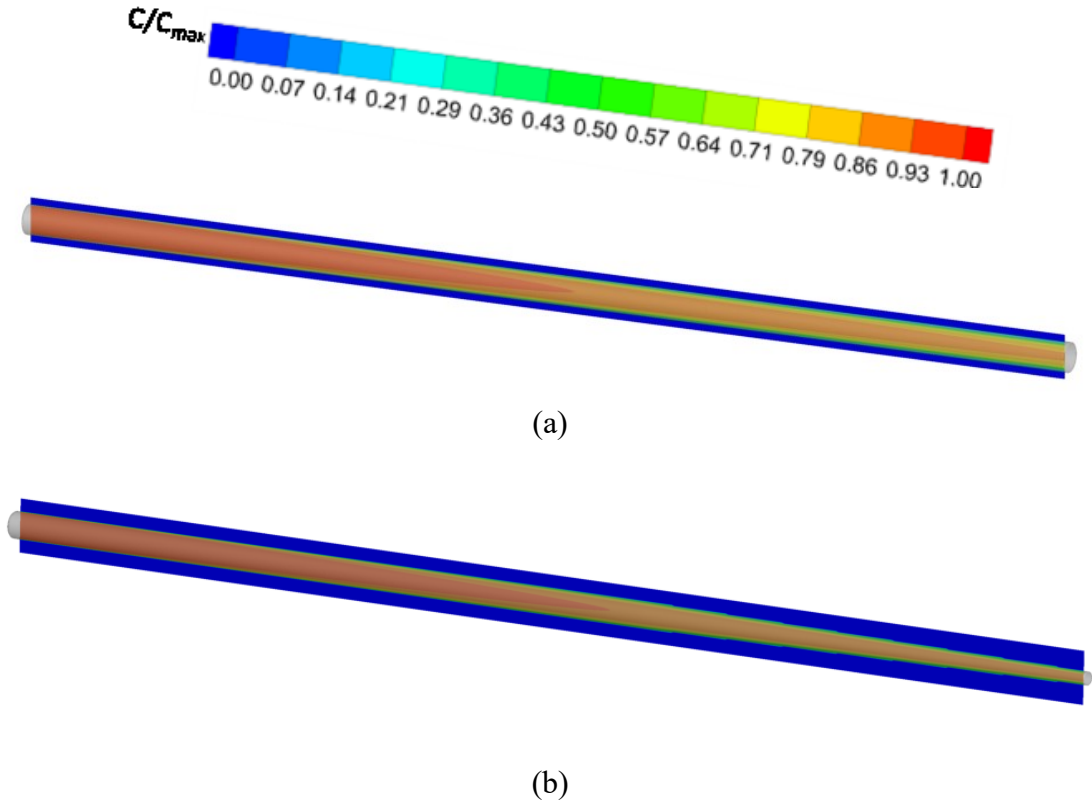


Figure 4-11. Computational models of straight (a) and tapered (b) phantom with the contrast concentration contour along the phantom at the mid y-plane at $t=20$ s.

The driving equation for the G-W flow is Navier-Stokes equations (Eq. 4-1) and the contrast dispersion is solved via convection-diffusion equation (Eq. 4-2). The inlet flow boundary condition (BC) was set to be a parabolic velocity profile in the axial direction of the phantom ($u(r) = U_{avg}(1 - (\frac{r}{R})^2)$) where U_{avg} is set to be the average velocity for the corresponding flow rate and R is the radius of the phantom. The Reynold's number ($Re = \frac{2U_{avg}R}{\nu}$) ranges from 25 to 75 where $\nu \sim 4 \times 10^{-6} \frac{m^2}{s}$ is the kinematic viscosity for blood (and in this case G-W solution). Outlet flow BC is set to be Neumann with pressure and velocity and, the wall boundaries are set as no-slip condition. Contrast BC at inlet is defined as a linear AIF ($C(t) = t/T_d$) where T_d is the duration time of infusion of contrast into the system and is set to be 20 seconds. The simulations employ a previously developed in-

house immersed boundary solver ViCar3D with the details described in Chapter 2, section 2.3.1. Since the Schmidt number defined as $Sc = \frac{\nu}{D}$, where D is the molecular diffusivity of contrast, is not exactly known for the iodinated contrast agent (Omnipaque 240 mg) two lower and upper (1 and 1000 respectively) limits of Sc numbers have been investigated. Once the flow and contrast are solved, the average cross-sectional contrast concentration and velocity are calculated in 100 equally spaced cross-sections perpendicular to the axial direction of the flow. TCG_V is then the slope of linearly fit curve to the cross-section averaged concentration versus cumulative volume curve. Further, the correction factor k is calculate as $k = \frac{Q_{sim}}{Q_{TAFE}}$ where Q_{sim} and Q_{TAFE} are the mean flowrate of the phantom calculated in simulation and estimated by TAFE analysis, respectively. Similar to the pattern observed in the experiment and Figure 4-10, Figure 4-12 illustrates the radial variation of contrast in the simulations of tapered and straight phantom at three different locations of $s=22, 27$ and 32 cm for $Sc=1$ and 1000 . The locations are reported with respect to the entrance of the tube and the locations $s=22, 27$ and 32 correspond to locations at $s=2, 7$ and 12 from the entrance of the phantom. As anticipated, the radial profiles with $Sc=1000$, because of the lower molecular diffusivity, show a higher radial variation compared to that of the cases with $Sc=1$.

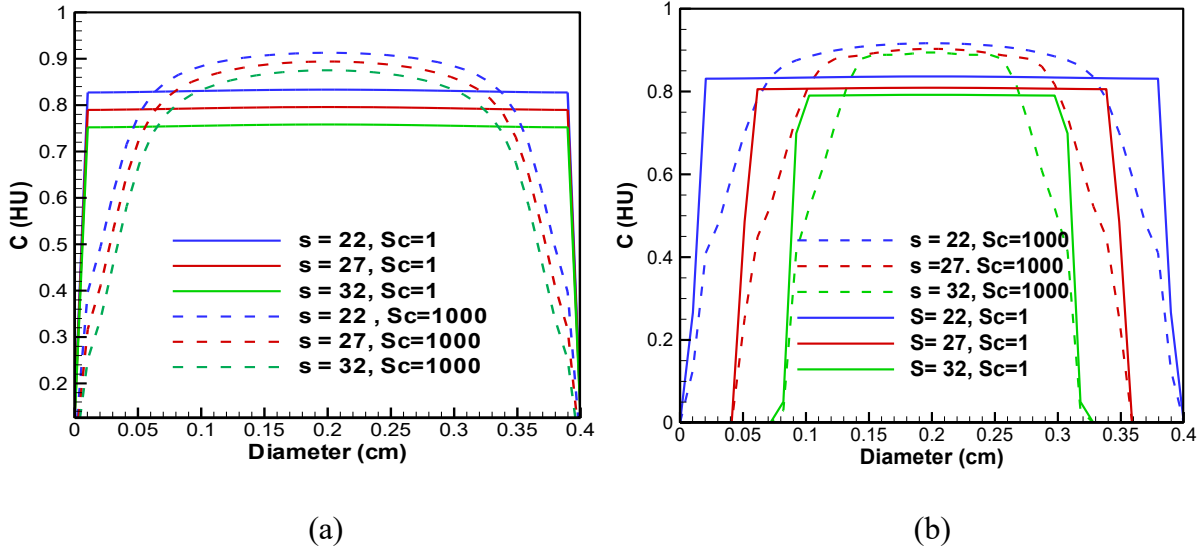


Figure 4-12. Radial profile of the mean contrast concentration for straight (a) and tapered (b) phantom with two values of $Sc=1$ and 1000.

4.2.5.2. Errors due to Imaging Resolution

Computed tomography images are inherently more prone to artifacts than other conventional radiographs because the images are reconstructed from a large number of independent detectors assuming that all these measurements are consistent (Barrett & Keat, 2004). These artifacts can vary from errors in X-ray attenuation measurements to partial-volume averaging (PVA) effects to malfunction of the detectors caused by errors in detector calibration (Al-Shakhrah & Al-Obaidi, 2003). Errors connected with the finite resolution of the imaging such as PVA and filtering are particularly important here and the focus of this section. Since separation and differentiation between these artifacts is not trivial, a general correction factor is calculated here to account for these imaging artifacts. To improve upon our estimation and correct for the imaging artifacts, a pre-mixed solution with contrast with ratio of 1 to 10 is prepared and inserted into the tapered phantom with the two ends affixed. With this set up, there is no flow in and out the phantom and

theoretically, there should be no TCG along the vessel. However, as illustrated in Figure 4-13a and Figure 4-13b, there is an apparent drop in the contrast attenuation along the vessel in which can be partly explained by PVA effects. To correct for this drop, the cross-sectional average concentration, C_{CT} , is divided by a “reference” concentration, C_{ref} , called $\alpha(A)$ (Eq. 4-9a) and, is plotted against the area at each cross-section (Figure 4-13c). The resultant data, α_{fit} , is then fitted to a polynomial of the form in Eq. 4-9b where, A is the area and coefficients a , b , c and d are determined to be -0.1500, 0.8578, -0.1455 and 0.0015 respectively.

$$\alpha(A) = \frac{C_{CT}}{C_{ref}} \quad (4-9 a)$$

$$\alpha_{fit}(A) = a + \frac{b}{\sqrt{A}} + \frac{c}{A} + \frac{d}{A^2} \quad (4-9b)$$

The reference concentration is measured with a pre-mixed ratio of 1 to 10 of G-W solution to water in a test tube with a diameter of 3 cm with no known imaging artifacts. Subsequently, the concentration for each cross section is corrected employing Eq. 4-10, where, A_{CT} and C_{corr} are the measured CT area and the corrected concentration, respectively. The corrected concentration is shown with red dots in Figure 4-13a for the pre-mixed tapered phantom where the slope of the corrected data is expectedly very close to zero. Similarly, a sample case with flow has been corrected for the ‘artificial’ TCG introduced by imaging artifact in Figure 4-13b.

$$C_{corr}(A) = \alpha_{fit}(A_{CT}) \times C_{CT} \quad (4-10)$$

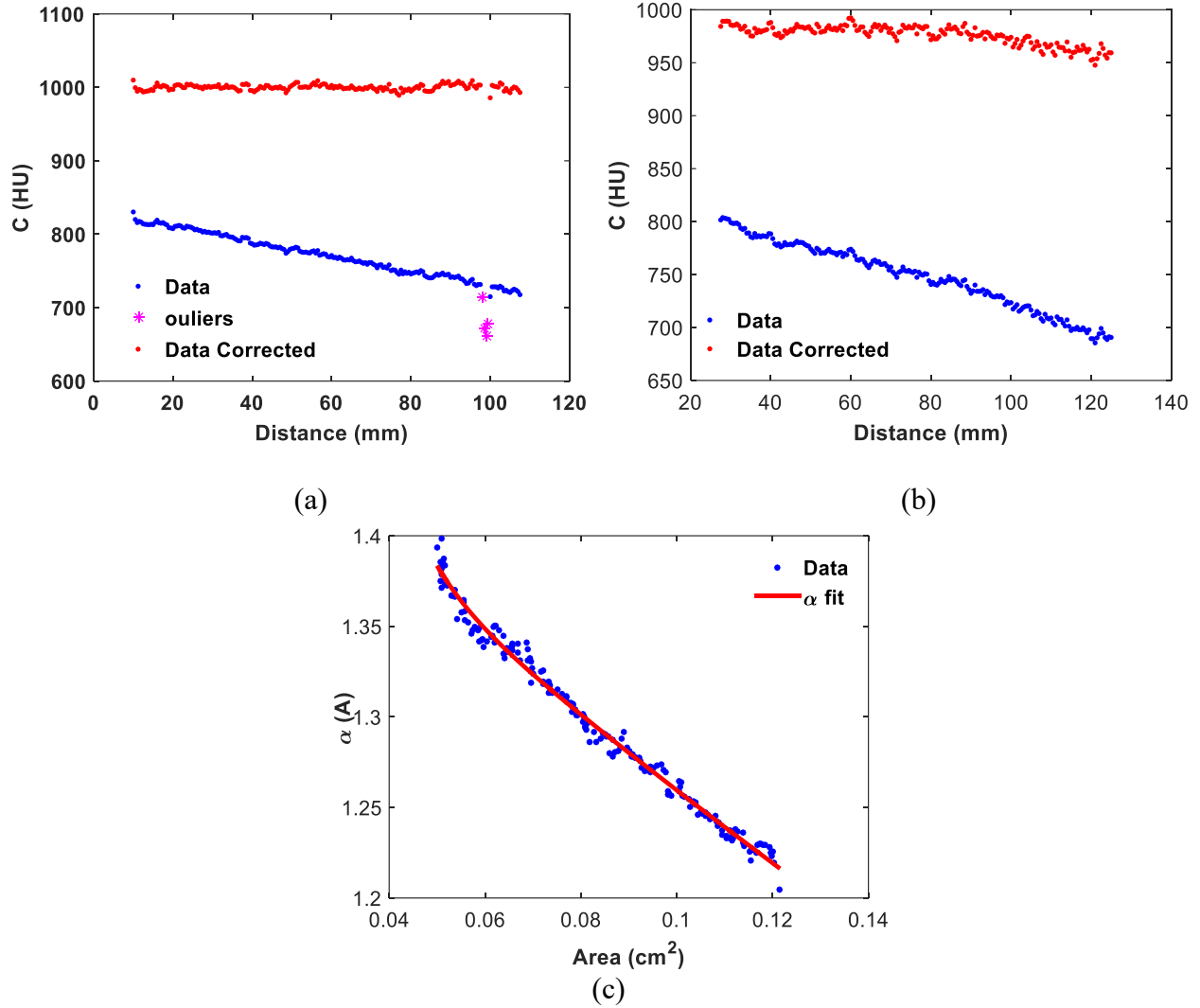


Figure 4-13. Cross-sectional average concentration of contrast agent along the axial direction of a pre-mixed tapered phantom experiment (a) and in a representative phantom experiment with flow (b). The blue dots show a drop in concentration despite the stationary flow in the phantom. The red dots are the corrected using the α correction factor determined from (c) where the red line is the fitted polynomial in Eq. 4-8b.

4.3. RESULTS AND DISCUSSION

Table 4-1 and Table 4-2 lists the original values and the corresponding corrections for the straight and tapered phantom, correspondingly. The results reported here is

analyzed via the simple thresholding segmentation methodology explained in Section 4.2.4. The original results taken from phantom with no corrections compared with the true pump flow rates of $Q = 20, 25, 30, 35$ and 40 ml/min for the straight phantom and $Q = 25, 35, 45$ and 55 ml/min for the tapered phantom are shown in Figure 4-14 by blue diamonds. For the straight phantom, the TAFE prediction shows a linear estimate with true pump velocity but the rate of rise of the estimated pump velocity is only 67% that of the true pump velocity. Consequently, the prediction becomes worse with increasing pump velocity. The estimation for the tapered phantom shows similar trends although the under-prediction is significantly exaggerated. The rate of rise of the estimated flow rate is only about 11% of the true rise and this leads to an estimated flow rate that barely increases with the true flow rate.

We first apply the “k-correction,” i.e. the correction due to non-uniform flow, to this phantom data. Based on our analytical modeling with assuming a parabolic profile for both the flow velocity and contrast, we calculate the k factor to have a range of 1.3-1.6. Here we used an average value of $k = 1.4$ for both straight and tapered phantom through all the flow rates and we use the formula in Eq. 4-8 to correct the TAFE estimation of the flowrate. Interestingly, after the k-correction is applied in Figure 4-14a (shown in red diamonds) the straight phantom results become very close to the dashed 45-degree angle line with the slope of 0.94 and an average under-prediction of 0.2629 ml/min. This implies that the flow development effects are indeed important in the phantom experiment.

For the tapered phantom, the k-correction does lead to an improvement with a resulting slope of 0.74 and an average under-prediction of 6.2 ml/min, but this improvement is clearly not sufficient for an accurate prediction. We have subsequently

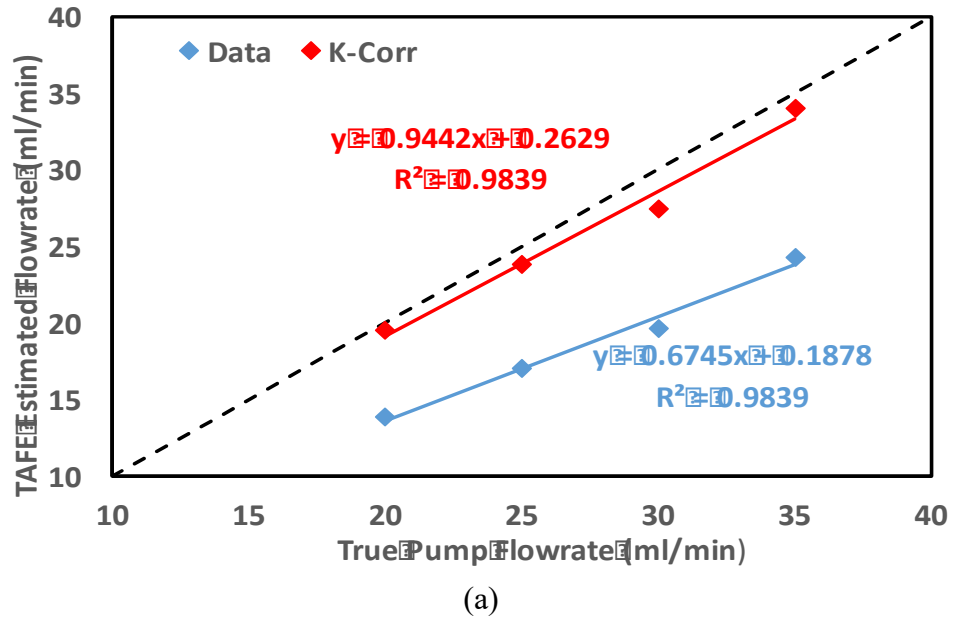
applied the “ α -correction” to the tapered phantom. It should be noted that the α -correction does not apply to the straight phantom since PVA and filtering is not expected to change the measured TCG in a straight phantom. When the α -correction is applied to the k-corrected TAFE prediction for the tapered phantom (Figure 4-14b), there is a significant improvement in the accuracy of the prediction: the predicted slope is now 1.04 which is very close to unity and the mean error in the prediction 8.71 ml/min. We note here that the tapered phantom does not show the strong linear correlation with true pump rate (R^2 value of 0.74) as the straight phantom (R^2 value of 0.98) and this points to other errors/uncertainties in the experiment. However, overall, within the limitations of the experimental setup, the current experiments and analysis demonstrate that there are systematic errors in the TAFE prediction due to inherent flow physics and imaging artifacts, and that there is a possibility of correcting for these errors.

Table 4-1. List of flowrates estimated by TAFE and the corresponding corrections for the straight phantom.

$Q_{pump} (ml/min)$	$Q_{TAFE}(ml/min)$	$Q_{TAFEk-corr}$
20	13.95	19.52
25	17.03	23.84
30	19.65	27.51
35	24.31	34.04
40	33.37	46.71

Table 4-2. List of flowrates estimated by TAFE and the corresponding corrections for the tapered phantom.

$Q_{pump} (ml/min)$	$Q_{TAFE} (ml/min)$	$Q_{TAFE\alpha-corr}$	$Q_{TAFE_{k+\alpha-corr}}$
25	4.28	17.12	23.95
35	4.15	15.86	22.24
45	4.86	21.90	30.66
55	7.83	40.08	56.11



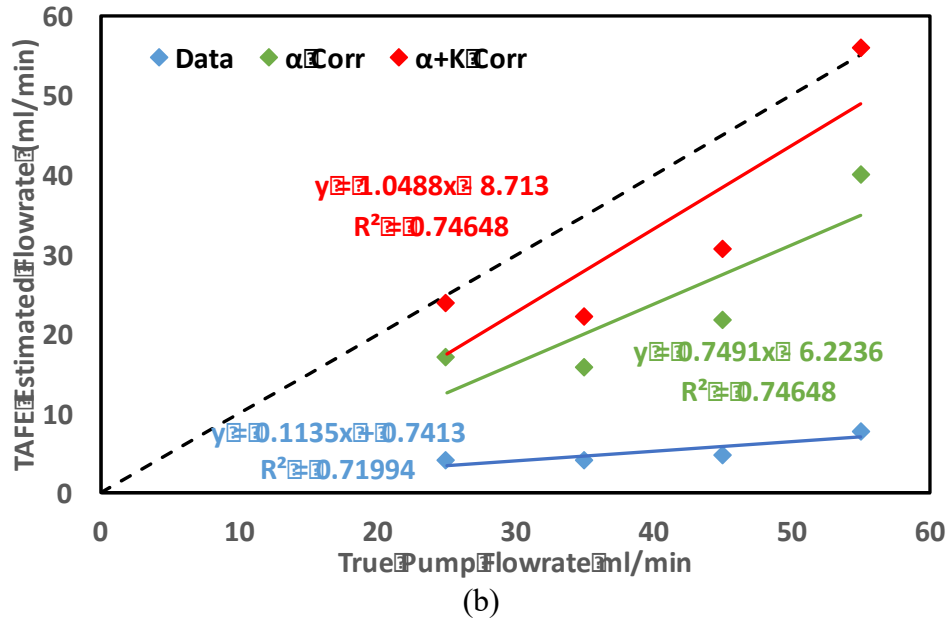


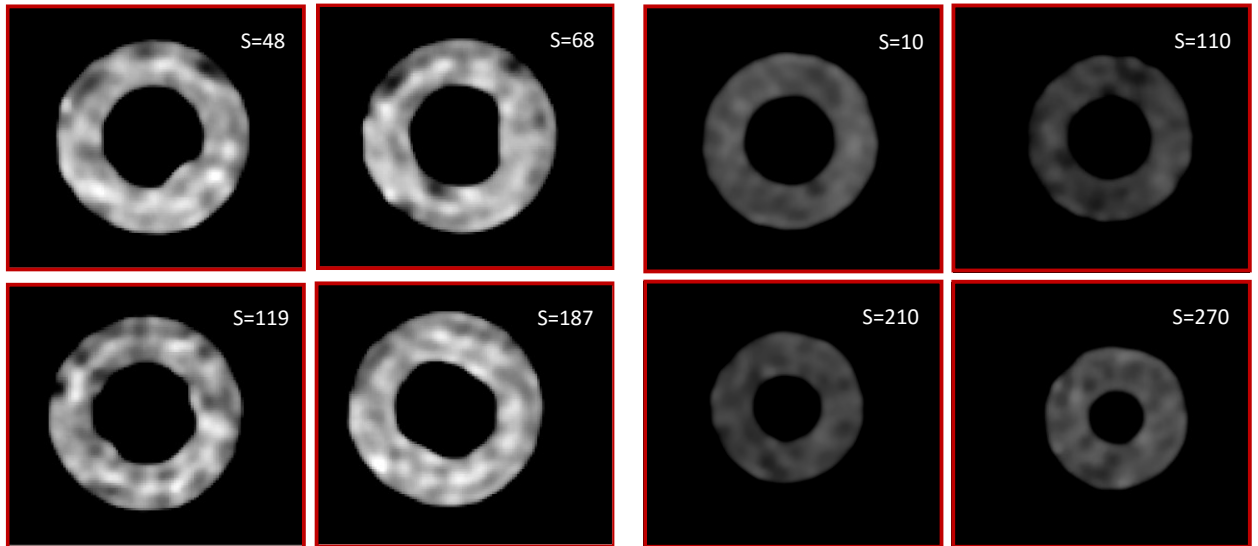
Figure 4-14. Comparison of TAFE Estimated flowrate with the true pump flow rate for straight (a) and tapered (b) phantoms. The result significantly improve after the corrections are applied.

4.3.1.1. Limitations and Caveats

There are a number of limitations of the experiments and other sources of errors in the experiments that are worth discussing. First and foremost, we employ steady flow rates through the phantom whereas physiological flow through the artery is pulsatile. Computational modeling (see Chapter 3) has shown that TAFE might be applied to pulsatile flow with reduced accuracy but this was not examined in the experiments due to the complexity of setting up a CT compatible pulsatile flow loop. The phantom also does not include motion artifacts that appear in CCT imaging of patients. Since the coronary vessels are embedded in the moving myocardium, the finite temporal resolution of the scanning procedure can introduce motion artifacts that are not modeled here. In addition, when the k-correction is applied, we take a universal k value of 1.4 for all flow rates and

tapered phantom. However, k factor depends on the flow rate as well as the geometry. The TAFE formulation assumes no radial component of velocity in the vessel, whereas with the introduction of tapering to the system, the velocity will inherently have radial components and is no longer unidirectional.

In terms of the phantoms, we also found that that in the 3-D printing process, even with the subsequent etching of the surfaces, the inner walls of the straight and tapered phantoms are not smooth and have a high degree of roughness (Figure 4-15). This roughness extends into the body of the phantom and this would introduce additional artifacts into the CT image. Finally, the phantom geometry is very simple with no curvature or branching; both of these features could also affect the image quality and TAFE prediction.



(a) (b)
Figure 4-15. Examples of 'rough' and non-uniform surfaces of the inner wall for different locations along the phantom for (a) straight phantom and (b) tapered phantom.

4.4. SUMMARY

A CT compatible experimental phantom study has been conducted to validate the analytical TAFE formulation. Several assumptions were made in the TAFE formulation and in this study, the TAFE formulation was modified for the radial variation of the contrast in the phantom. In addition, a general correction has been applied for the net total of imaging artifacts. The corrected estimations are in good agreement compared with the actual pump values. However, the phantom does not currently address other important features such as flow pulsatility, motion artifacts and vessel curvature and branching.

CHAPTER 5: CONTRAST DISPERSION IN AORTIC ARCH AND EFFECT OF FLOW PATTERN ON ARTERIAL INPUT FUNCTION

5.1. INTRODCUTION

The aorta is the largest artery in the human body and it carries oxygenated blood from the LV to the systemic circulation. The aorta consists of the ascending aorta, the aortic arch and the descending aorta. The ascending aorta originates from the aortic root which connects the left ventricle to the aorta, and the key anatomical features of the aortic root are the aortic valve annulus, the valve leaflets, the sinuses of Valsalva and the sinotubular junction. Following the ascending aorta, the aortic arch bends to connect with the descending aorta and three large vessels originate from the aortic arch: the brachiocephalic artery (BA), the left common carotid (LCC) artery and left subclavian (LSC) artery, which supply blood to the upper limbs, head and neck and posterior cerebral circulation, respectively (See Figure 5-1).

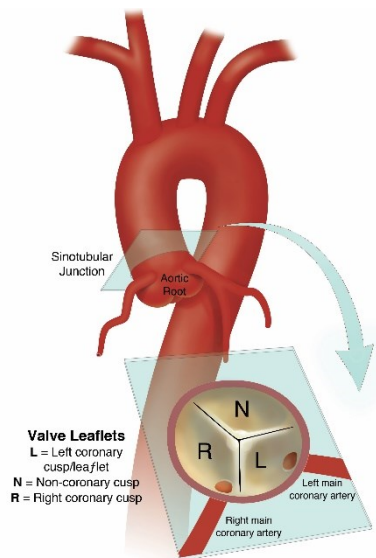


Figure 5-1. Schematic of the Aortic root with the coronary sinus, aortic valve leaflets and sinotubular junction defined. This schematic is taken from University of Florida's health webpage at: <https://m.ufhealth.org>

The focus of the current work is on the implication of aortic flow on the contrast dispersion patterns and gradients generated in the coronary arteries. Given this emphasis, it is useful to describe the anatomical relationship between the aorta and the coronary arteries. The coronary arteries originate from the sinuses: the LCA from the left coronary cusp (LCC), the RCA from the right coronary cusp (RCC) and the third cusp is the non-coronary cusp (NCC). Thus, the coronary ostia are located in the sinuses and the contrast that enters into the coronary ostia is associated with the pool of blood that accumulates in the sinuses during the cardiac cycles.

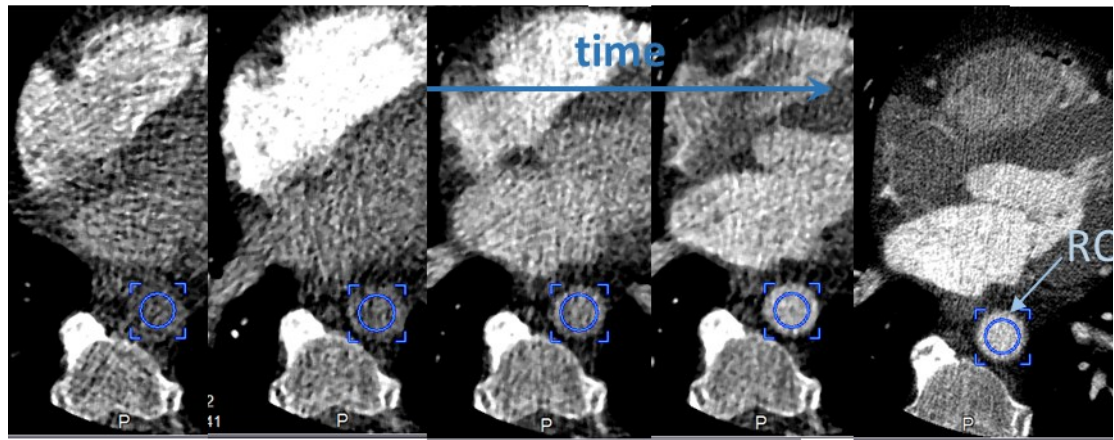
A second focus of the current work vis-à-vis the aorta is behavior of the flow and contrast not only in the ascending aorta but also the initial portion of the descending aorta. As explained in earlier chapters, the contrast concentration in the descending aorta is used as an estimate of the corresponding attenuation at the coronary ostia (i.e. in the AIF) and analysis of this feature in cardiac CT, especially with respect to its implication for TAFE, requires the simulation and analysis of the flow and contrast in the ascending as well as the initial portion of the descending aorta.

Due to its significant role in distributing oxygenated blood throughout the body, blood flow pattern in the aorta and its relationship with various disease conditions has been investigated in many previous studies experimentally (Angelsen & Brubakk, 1976; Kupari et al., 1995; Seed & Wood, 1971; Segadal & Matre, 1987) and non-invasively via imaging (Ahmed & Giddens, 1984; Bogren & Buonocore, 1994; Kilner et al., 1993; Morbiducci et al., 2009; Wentland, Grist, & Wieben, 2014) and numerically (Karmonik et al., 2008; Kim et al., 2004; Shahcheraghi et al., 2002; Svensson et al., 2006). However, these studies have neither included the coronary sinus nor the aortic valves in their models and can therefore

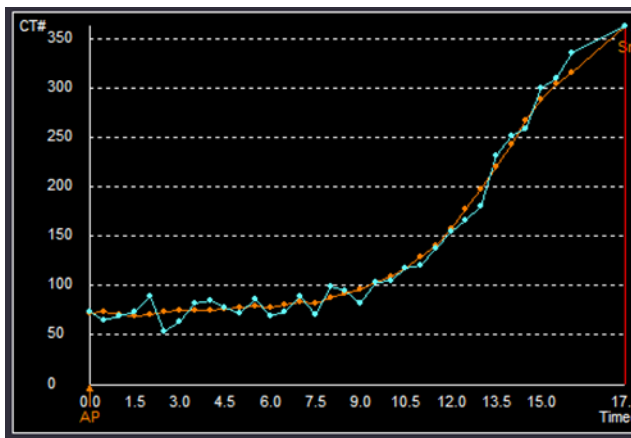
provide limited insights into the issue of interest here. While some recent studies have included valves (mostly bioprosthetic valves), the models typically do not include the aortic arch and the proximal descending aorta (De Hart, Baaijens, Peters, & Schreurs, 2003; Kamensky et al., 2015; Long et al., 2012). In addition, in most of these studies, the model of the aorta that is considered is canonical and is missing features associated with actual, subject-specific conditions.

In addition to the above limitations of prior studies with regard to the issues of interest here, none of these prior studies have reported information or analysis of contrast dispersion through the aortic arch. Contrast dispersion in arteries has many fundamental clinical implications and is of an importance for many imaging modalities that address coronary function/perfusion such as MR perfusion in detecting myocardial infarction (Akbulak & Conturo, 1996; Gatehouse et al., 2004), Helical (George, Ichihara, Lima, & Lardo, 2010) and multi-detector CT (George et al., 2007; Young, Noon, & Marincek, 1980) for myocardial perfusion and coronary artery disease (CAD) as well as other diagnosis beyond coronary function, such as dynamic CT for assessing vascular lung lesions and contrast-enhanced MR in analysis of tumor microvasculature (Parker et al., 2006) and tumor kinetics (Port, Knopp, & Brix, 2001). In the studies mentioned, contrast dispersion in the aorta becomes significant when assessing Arterial Input Function (AIF) or Time-Density Curve (TDC) - a time variation of contrast agent at one spatial location. In coronary CTA, the contrast is injected into the patients' body over a predetermined time-scale and since it mixes with blood through the four chambers of the heart and through the intervening circulation, the 'shape' of the AIF's becomes different depending on the location of acquirement.

In the particular context of the TAFE method the following issue comes to fore: TAFE assumes that the time-density curve of the attenuation function (the AIF) at the coronary ostia is available from the cardiac CT imaging. However, due to the difficulty of placing the ROI in the coronary ostia (which undergo significant motion), the ROI in conventional cardiac CT exams is placed at a laterally equivalent location in the descending aorta (see Figure 5-2). The time-density curve of contrast (i.e. the AIF) is easily tracked in the descending aorta (via automated or semi-automated procedures) which is well defined and quite stationary. The classical use of the AIF is to determine the arrival of the contrast bolus into the coronary circulation so that the image acquisition may be triggered. This is done by a low-dose dynamic scan where the attenuation in the ROI in the descending aorta is tracked in time. Once this attenuation reaches a predetermined level (300 to 500 HUs depending on the imaging protocol), the cardiac CT image scan is triggered. For this purpose of bolus tracking, the use of the descending aorta for determining the contrast concentration at the coronary ostia is probably acceptable. However, for the purposes of TAFE, using the AIF in the descending aorta to approximate the time-density curve at the aorta might lead to errors on undetermined magnitude. This is because there is a finite time-of-flight (ToF) of contrast between the valve sinuses and the descending aorta ROI, and if this ToF is large, it could add errors in the TAFE calculation.



(a)



(b)



(c)

Figure 5-2. Clinical representative case with (a) Descending aorta ROI cross-sections defined at the sure-start process where 2D images of the heart including the descending aorta is taken. The last image (right most image) is the volume image with the peak contrast value associated. (b) Time profile of contrast or AIF is then created measuring the mean contrast attenuation in HU at the ROI blue regions where the last point belongs to the volume image after the scanner is triggered. (c) Electrocardiogram (ECG) information of the patient while scanning including the HR. The scanning is done through a ECG gated process to prevent motion artifacts where the heart has the least motion in the R-R interval. The yellow bar (or blue shaded region) represents the phase that the image has been acquired.

To summarize the motivation and objective of the study described in the current chapter: in Chapter 3, we introduced a new method called Transluminal Attenuation Flow Encoding (TAFE) for quantifying the flow velocity and flow rate in a coronary vessel using information from contrast enhanced cardiac CT imaging. As explained above, the AIF at the coronary ostium that is employed in TAFE is actually obtained at the descending aorta in CCT imaging. Thus an inherent assumption in TAFE is that the AIF in the descending aorta is an accurate representation of the AIF in the coronary ostia. Examination of this assumption is the primary motivation behind the current research. The particular objective of the current work are:

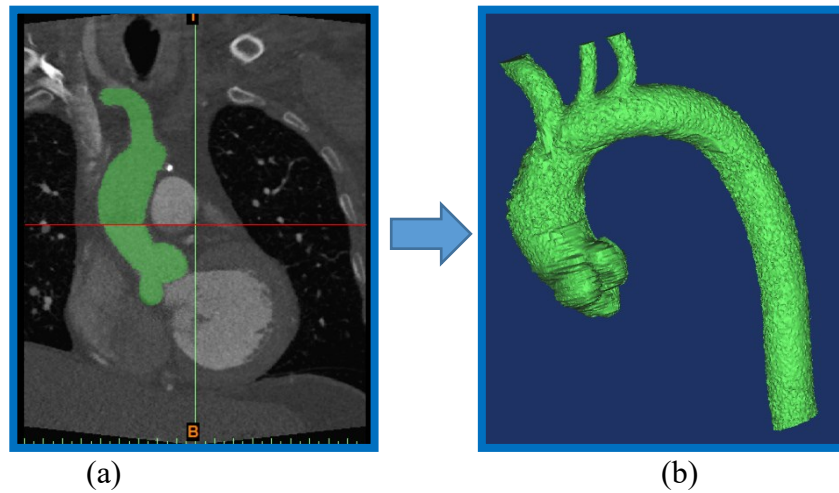
- 1) Compare the AIF's shape and duration in the ascending (at the coronary ostium) and descending aorta, in a highly realistic model of the aorta, and understand the differences within the context of the flow and dispersion patterns in the aorta.
- 2) Investigate the effect of contrast diffusivity (i.e. Schmidt number (Sc) on the AIF) and contrast dispersion patterns through the aortic arch. This is motivated by the fact that contrast diffusivity might vary significantly between different types of contrasts and the effect of this variation on AIF needs to be understood.
- 3) Study the potential correlation of flow pattern and contrast dispersion at different Sc numbers.
- 4) Study the effect of flow pulsatile on the AIF.

Thus, to be able to meet the objectives above and to describe the complex flow, detailed analysis of fluid flow and contrast dispersion in a patient-specific computational model of the complete aorta including the sinus and the aortic valve is performed using the CFD solver with the details discussed in Chapter 2, Section 2.31. In particular, we compare the

flow field by three-dimensional visualization of vortex structures, examine the phase-averaged velocity field, vorticity field and contrast along the orthogonal planes to the centerline of the vessel and compare the contrast profile variation in time. Additionally, cross-correlation time between the AIF profiles at the two locations of coronary ostium and descending aorta is compared with the transient time of flow between these two locations to investigate the effect of molecular diffusivity.

5.2. METHODS

In order to investigate the flow pattern and contrast dispersion in the aortic arch, we employ the framework described in Chapter 2 to develop a computational model of the aorta and the valve using high resolution 3D cardiac CT images. This model includes the aortic root with the two coronary sinuses and non-coronary sinus as well as a physiological derived aortic valve model.



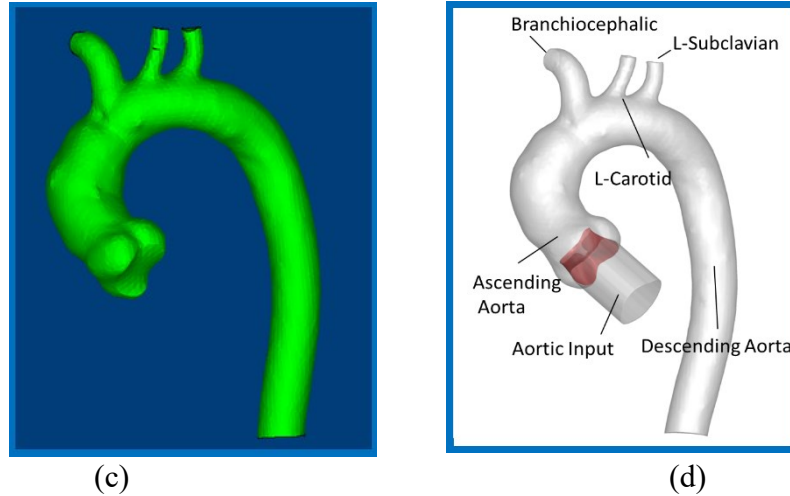


Figure 5-3 Steps involved in segmentation and creation of model-ready geometry. Dynamic region growing methodology was used to segment the aorta (a). The 3D geometry of the segmented artery is constructed using volume rendering (b). The rendered geometry is then smoothed using property preserving smoothing operations (c). The CFD ready model of aorta including the simple inflow tube along with the valve inserted at the aortic orifice. The snapshot is taken at end diastole.

5.2.1. Segmentation and Generation of CFD-Ready Aorta Model

The present 3D model of the aorta as shown in Figure 5-3a along the highlighted ROI is extracted from a high resolution 0.351x0.351x0.5mm voxel resolution, 512x512x440 total voxels) ECG-gated CTA scan (Toshiba 320 Aquilon One) of a patient's aorta with no known aortic or aortic valve diseases who has had a CABG (Coronary Artery Bypass Grafting) procedure done. This data was received a fully anonymized dataset and obtained under a valid IRB protocol. It should be noted that in a typical coronary CTA, the complete aortic geometry is not available but in this particular case, this was available because a full chest scan is performed for patients with CABG procedure to image the bypass section . For this model, the segmentation is performed using dynamic region-

growing algorithm (Rangayyan, 2005) using a thresholding level of 700 HU in Mimics (Mimics, *Materialise Inc.*). The segmented region was then edited manually to ensure correct segmentation of the vessel and inclusion of all the regions of interest. In addition, to remove any skewed or sharp sections, the surface was smoothed using the “smoothing-wrap” tool with the smoothing factor of 0.7 in Mimics. Figure 5-3b and Figure 5-3c are the segmented 3D geometry and the smoothed version of the aortic geometry, respectively. The three arteries at the top of the arch are segmented for the available field of view and were truncated to remove any segmentation fault at the outlets. The aortic root along with the sinus is segmented so that all three are included where the valve cusps meet. Moreover, since the focus here is to understand the effect of flow on contrast dispersion, we follow the conventional approach of using a simple model of the inflow (De Hart, Peters, et al., 2003; M.-C. Hsu et al., 2014; Kamensky et al., 2015) from the left ventricle to the aorta as shown in Figure 5-3d where the simple tube model of the outflow tract is extended to match the aortic orifice geometry at the coronary sinus and the cross-sectional area does not vary throughout the cardiac cycle. In order to see the detailed effects of pulsatility on the flow pattern and contrast dispersion, an inflow velocity profile (shown in Figure 5-4a and Figure 5-4b in blue) is taken from the preclinical canine flow profile reported in (Clark & Schultz, 1973) where the peak velocity of $V_{peak}=0.98$ m/s and the period has been adjusted to match human peak velocity at the aortic root reported in (Gisvold & Brubakk, 1982). This choice of inflow profile is very close to that of human inflow velocity measured in (Segadal & Matre, 1987). With the inflow velocity illustrated in Figure 5-4, the stroke-volume (SV) is calculated to be $SV = \int V dt \cdot A \cdot HR = 118.24$ ml where A is the area of

the aortic orifice and HR is the heart rate. The list of flow parameters can be found in Table 5-1.

5.2.2. Aortic Valve Modeling and Motion

As mentioned in Section 2.2.2, it is essential to include a model of the aortic valves in order to generate realistic flow patterns in the aorta (De Hart, Baaijens, et al., 2003; De Hart, Peters, et al., 2003; Makhijani, Yang, Dionne, & Thubrikat, 1997; Ranga, Bouchot, Mongrain, Ugolini, & Cartier, 2006). However, none of the imaging modalities (Echo, CCTA or CMR) have either the spatial or the temporal resolution required to adequately resolve the motion of the valve leaflets. We therefore choose to employ a kinematic model of the aortic valve with a prescribed sinusoidal canonical motion inspired by two previous numerical and experimental (Bellhouse & Talbot, 1969; Swanson & Clark, 1973) and in-vivo (Leyh et al., 1999) studies. In Bellhouse & Talbot (1969) fluid mechanics around a pipe with sinus and valve in a pulsatile tank was studied and their results compared against the solutions of the inviscid-flow equations, based on a Hill spherical vortex model. The valve velocity chosen in this study in a sinusoidal representation of what is reported in Bellhouse & Talbot (1969) (See Figure 5-5a).

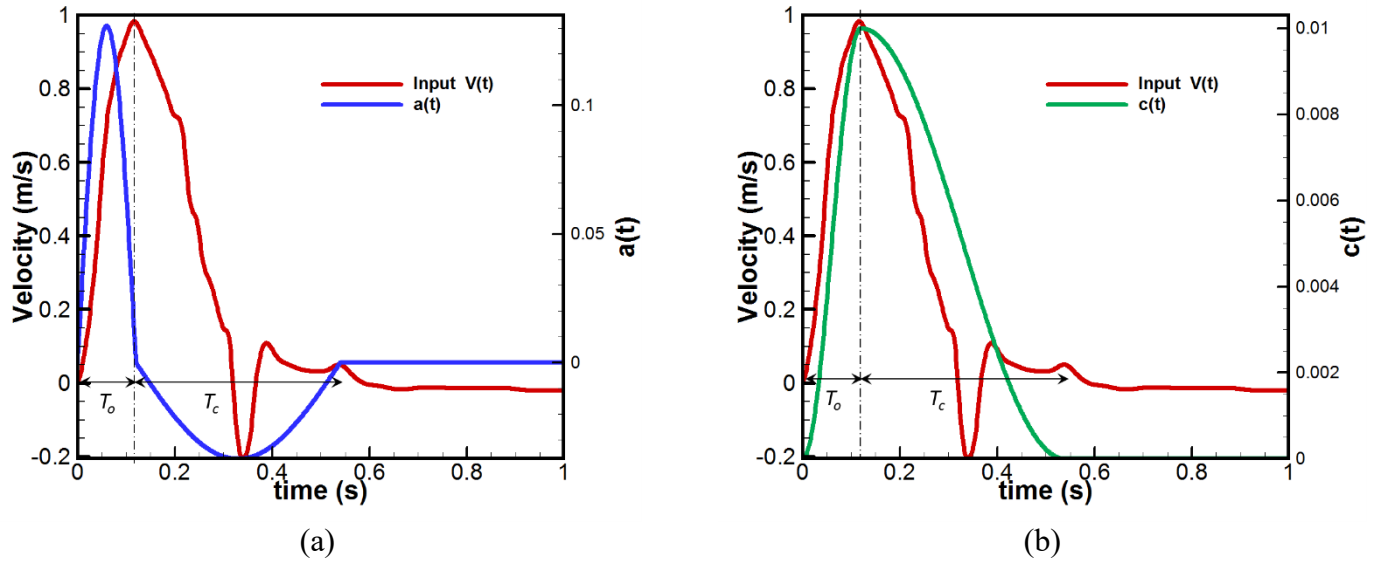


Figure 5-4. Velocity (a) and displacement (b) time variation of the valve compared with the velocity inflow profile. The opening time of the valve is defined as the time it takes to raise to the peak velocity and the closing phase is the time duration where the velocity drop begins in the inflow velocity until end systole.

In addition, the general motion of the valve prescribed in this study matches those reported in *Leyh et al.* (Leyh et al., 1999) in their in vivo study of valve motion via echocardiographic imaging in systole where faster opening and slower systolic closure was observed in the three groups of patients A, B and C (See Figure 5-3b).

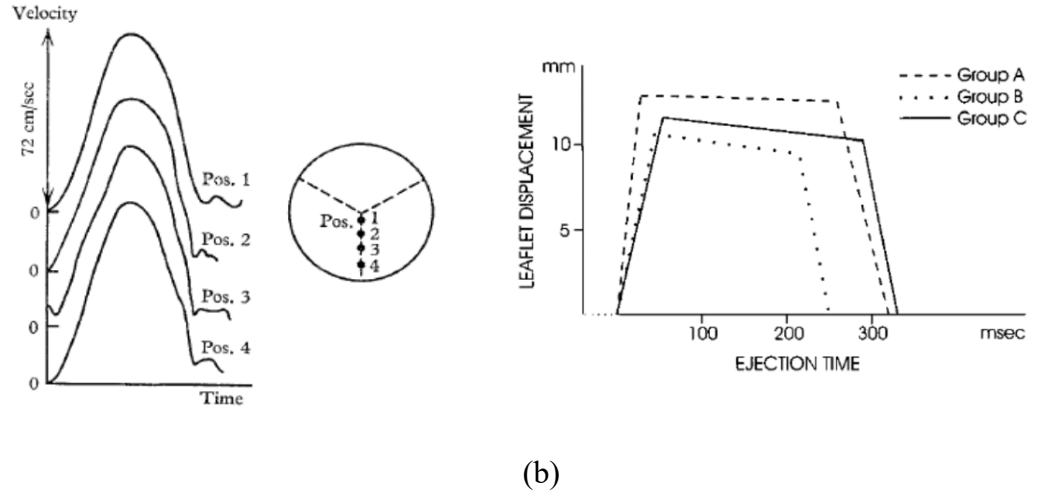


Figure 5-5. (a) *In-vitro* measurements of valve leaflet velocity at 4 different positions on the sinus cusp. Similar trend of opening and closing time is observed. (Bellhouse & Talbot, 1969) (b) *In-vivo* measurements of the aortic valve measurements in systole via echocardiographic imaging in 3 groups of patients with valve dysfunction after surgical valve preservations. Each group's valve displacement includes a faster raise in opening time and a slower closing time interval. (Leyh et al., 1999)

Based on the observations from the studies above, the valve leaflets time component of velocity and displacement as well as the input velocity for this study is shown in Figure 5-4 where opening time is chosen based on the time raise to the peak velocity and the closing time is the remaining time from when velocity begins to drop to end of systole. Eq. 5-1a and 5-2b are the mathematical formations of the prescribed velocity and displacement of the leaflets, respectively:

$$v_{valve}(x, t) = a(t) \cdot \vec{b}(\vec{x}) \quad (5-1a)$$

$$d_{valve}(x, t) = c(t) \cdot \vec{b}(\vec{x}) \quad (5-1b)$$

where, $a(t)$ and $c(t)$ describes the time variation of valve velocity and displacement in time are defined in Eq. 5-2b and 5-2b and $\vec{b}(\vec{x}) = \vec{x}_{open} - \vec{x}_{close}$ is the valve motion described in space.

$$a(t) = \begin{cases} \frac{\pi}{2T_o} \sin(\frac{\pi t}{T_o}), & t \leq T_o \\ -\frac{\pi}{2T_c} \sin(\frac{\pi(t - T_o)}{T_c}), & T_o \leq t \leq T_c \end{cases} \quad (5-2a)$$

$$c(t) = \int a(t)dt = \begin{cases} \frac{1}{2}(1 - \cos(\frac{\pi t}{T_o})), & t \leq T_o \\ \frac{1}{2}(1 + \cos(\frac{\pi(t - T_o)}{T_c})), & T_o \leq t \leq T_c \end{cases} \quad (5-3b)$$

where T_o and T_c are opening and closing time of the valve respectively defined in Figure 5-2 and listed in Table 5-1.

Table 5-1. List of flow and contrast concentration parameter

Opening Time (T_o)	0.12 (s)
Closing Time (T_c)	0.42 (s)
Peak Velocity (V_{peak})	0.98 (m/s)
Stroke volume (SV)	118.24 (ml)
Heart Rate (HR)	60 (beats/min)
Reynolds No. (Re)	2960
Schmidt No. (Sc)	1 and 1000
Womersely No. (Wo)	14.39
Bolus Duration Time (T_d)	5 (s)
Bolus Starting Time (T_s)	0 (s)

As described in Section 2.2.2 the valve model is a ‘semi-patient-specific’ model where the annulus of the aortic valve is extracted from the patient-specific geometry and the open and closed configurations are created as one continuous model based on the available literature. Detailed description of the valve geometry can be found in Section 2.2.2. In addition, since the open and closed form of the valves do not have the same mesh topology, we perform a template-based surface registration as described in Section 2.2.3 using the Large Deformation Diffeomorphic Metric Mapping (LDDMM) method (Figure 5-6).

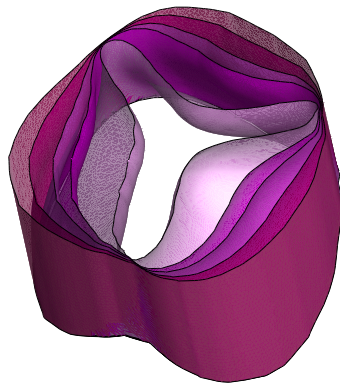


Figure 5-6. The open formed of the valve is morphed to the closed form using LDDMM. The valve motion is then prescribed between these two reference configurations. A sample of sequence of valve movement is shown here.

5.2.3. CFD Model and Non-Dimensional Parameters

The aortic arch model used in the current study is discretized with 223,990 triangular elements while the aortic valve is discretized with 14,734 elements. The entire model surface is immersed in a Cartesian grid of size 7.0cm x 11.0cm x 10.9cm with a 256x256x256 number of grid points in each direction (total of ~16.8 million). The immersed aortic model is shown in Figure 5-7a. The non-dimensional time step chosen is 1×10^{-2} which results in about 10,000 time steps per cardiac cycle. All the simulations were performed on MARCC (Maryland Advanced Research Computing Center) high performance computing cluster with 256 CPU cores for 5 cardiac cycles and the

computation for one cardiac cycle takes about 1 day for this grid resolution. In the current study because the compliance of the aortic arch is neglected, the only moving boundaries are the valve leaflets, which are modeled as membranes. Hence, the CFD solver has been modified to calculate the moving boundaries only on the membrane structure. Phase-averaging was performed across 2nd to 5th cardiac cycles allowing the system to stabilize with the fluid flow solution. The cross-sectional planes in which the cross-sectional averaged contrast time profiles are compared are defined in Figure 5-7b whereas the normal-to-the centerline planes are shown in Figure 5-7c for subsequent analysis of projected hemodynamic data is implemented.

The key non-dimensional numbers that define the hemodynamics inside the aortic arch (see Section 2.3) are listed in Table 5-1. In particular the Reynolds number (Re) for the present model is approximately $Re = \frac{2U_{mean}R}{\nu} = 2960$ while the Womersely number $\alpha = R\sqrt{\frac{\omega}{\nu}} = 14.39$ and Schmidt number $Sc = \frac{\nu}{D}$ has two values 1 and 1000. In the above parameters, $U_{mean} = 20.57 \text{ cm/s}$ is the mean flow velocity at the aortic orifice and $R = 2.87 \text{ cm}$ is the radius of the aortic orifice. The kinematic viscosity of blood is chosen to be $\nu = 4 \times 10^{-6} \frac{m^2}{s}$ while the cardiac duration is $T=1 \text{ (s)}$ ($\omega = 1 \text{ Hz}$) resulting in HR=60 bpm. The flow inlet boundary condition at the aortic valve is applied as a Dirichlet BC with the inlet flow velocity defined in Figure 5-4 while the contrast concentration BC is modeled as a half cosine function (Eq. 5-4) as have been utilized in (Eslami et al., 2015) and suggested in (Lardo, Rahsepar, Seo, Eslami, Korley, George, et al., 2015):

$$C_{ositum}(t) = C_{min} + \frac{1}{2}(C_{max} - C_{min}) \left(1 - \cos\left(\frac{\pi(t - T_s)}{T_d}\right) \right) \quad (5-4)$$

where, C_{min} and C_{max} are the minimum and maximum concentration at the ostium, T_s is the arrival time of the bolus and T_d is the time delay between the arrival time of bolus and the time the volumetric image is scanned. The starting and delay time are set to be $T_s = 0$ (s) and $T_d = 5$ (s). While the typical delay time between injection and arrival of contrast in patients are $T_d = 9-10$ (s), the delay time here has no particular meaning and is chosen as per modeling convenience. The boundary conditions applied at all the exits (downstream aorta and arteries coming off the aortic arch) are Neumann for velocity.

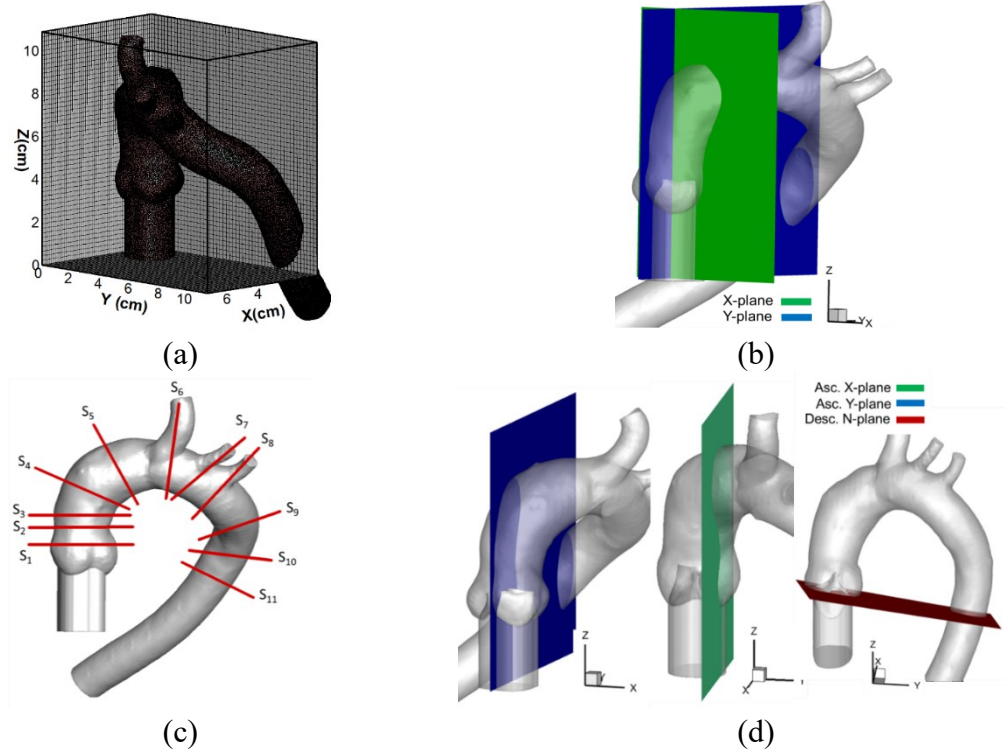


Figure 5-7. (a) Immersed computational model and (b) reference planes defined for presenting velocity vectors and contrast contour at the inlet and (c) time-averaged normal projected velocity, vorticity and contrast concentration and (d) Arterial Input Function planes at the coronary ostium/ascending aorta in the X-plane (green) and Y-Plane (blue) and the normal to the descending aorta (red).

5.3. RESULTS

5.3.1. Flow Patterns

In this section, we present the simulation results for the flow field in terms of the the velocity vectors and vortex structures. Figure 5-8 shows velocity vectors, colored by the magnitude of velocity in the ascending aorta for $t = T_o/2$, $t = T_o$, end systole at $t = T_o + T_c$, $t = (T_o + T_c) / 2$ and at end diastole $t = T$ (period) in the two reference planes shown in Figure 5-7b. In the ascending aorta, because of the existence of valve leaflets and coronary sinuses, the flow have significantly different patterns at each time point of the systole. At $t = T_o/2$, the valve is half way open and as seen in Figure 5-8a, a strong jet of flow starts to form. Subsequently, at $t = T_o$, when the valve opens completely, a strong flow jet forms and this reaches nearly unchanged to the arch. Interestingly there is very little flow generated in the sinuses at this time due to the sheltering effect of the valve leaflets. As the valve starts to decelerate and close at $t = (T_o + T_c) / 2$, the flow recirculation in the aortic root and sinus becomes visible. As the valve reaches end-systole and nears closure, the last bolus of flow is observed exiting the valve into the aorta.

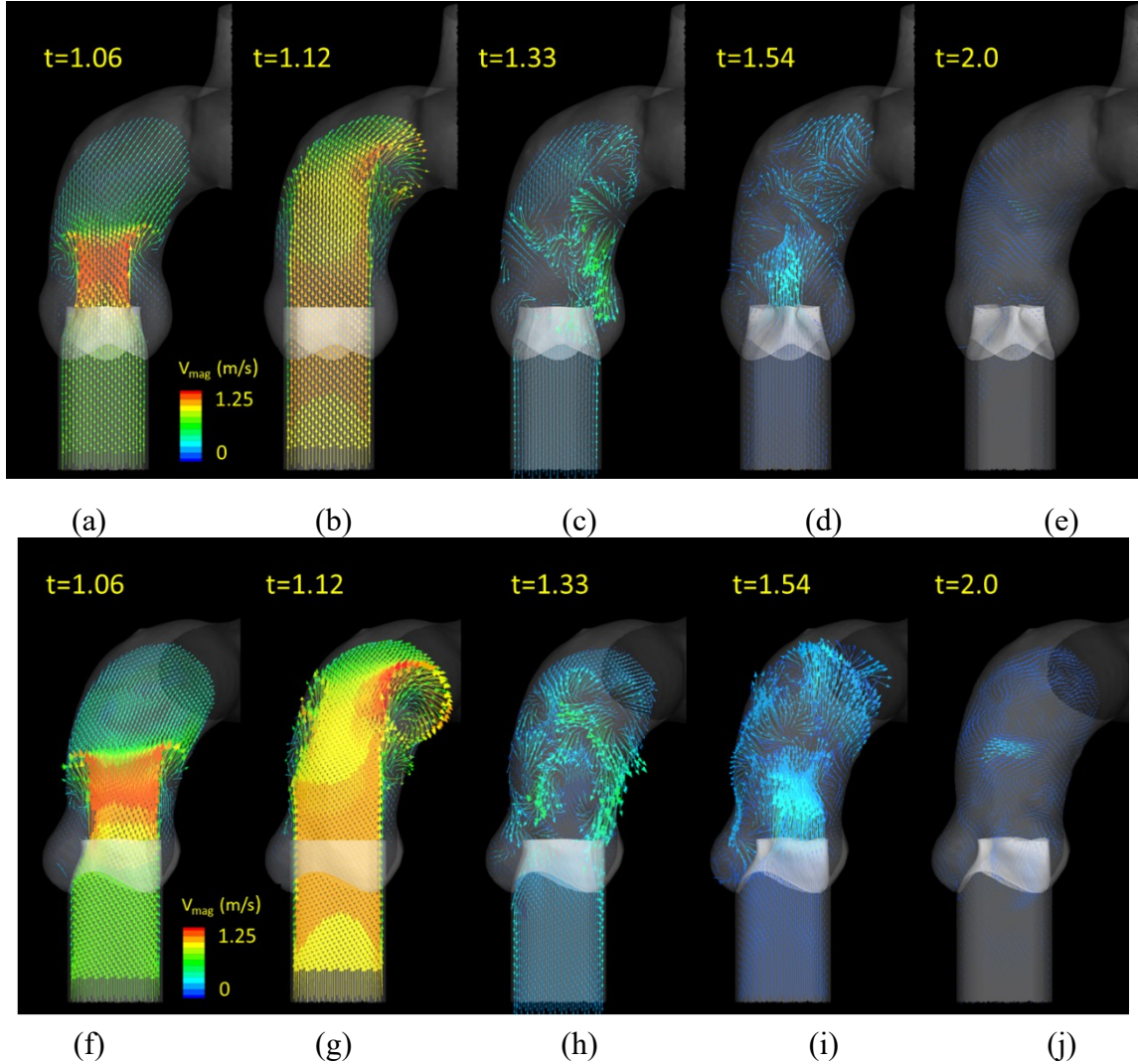


Figure 5-8 Velocity vectors colored with magnitude of velocity in the second cardiac cycle shown at the ascending aorta at two different reference planes of X-plane (a-e) and Y-plane(f-j) for 5 different time points of $t = T_o/2 = 1.06$ s, completely opened valve ($t = T_o = 1.12$ s), $t = (T_o + T_c)/2 = 1.33$ s, end systole ($t = T_o + T_c = 1.54$ s) and end diastole at $t = T = 2$ s).

Furthermore, at end diastole ($t = 2$ s), the flow in the ascending aorta is nearly static with some recirculation patterns near the valve tips and at the coronary sinuses. The vector field observed in our computational model are in good qualitative agreement when compared with other studies (Markl et al., 2005) where similar recirculation pattern forms behind the valve cusps and a strong flow jet ejects through the valve as it opens in a normal patient with no aortic disease.

Figure 5-9 shows the vortex structure inside the aortic arch, visualized by the Q criterion (where the second invariant of vorticity tensor is greater than zero i.e. $Q > 0$ (Haller, 2005; Wu, Xiong, & Yang, 2005) and colored by the magnitude of velocity, during the cardiac systole when the aortic valve is open. As the valve opens a small vortex ring is ejected from the aortic root (Figure 5-9a) and it continues to grow until the valve is half-open (Figure 5-9b-d). This vortex ring propagates to the aortic arch's outer wall and eventually breaks up resulting in large number of smaller vortex structures that dissipate rapidly (Figure 5-9e-i) over the next phase of the cycle. Finally, by the time the valve closes completely (Figure 5-9j) all the vortex structure have broken down and dissipated through the arch.

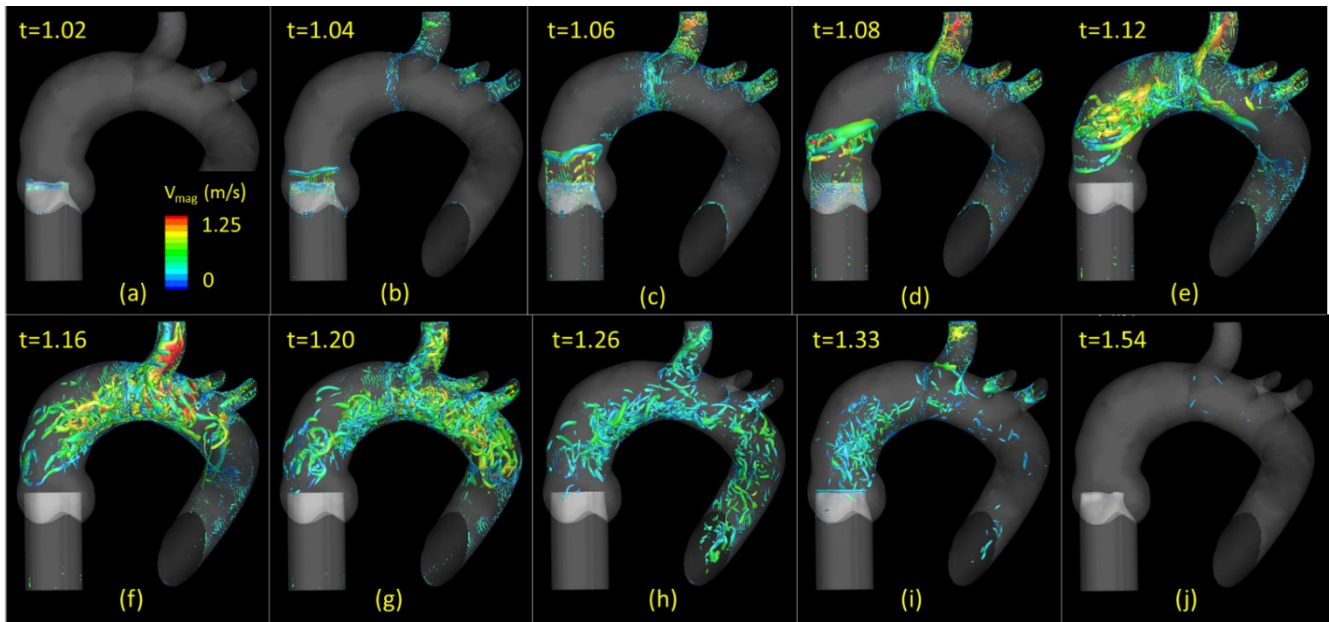
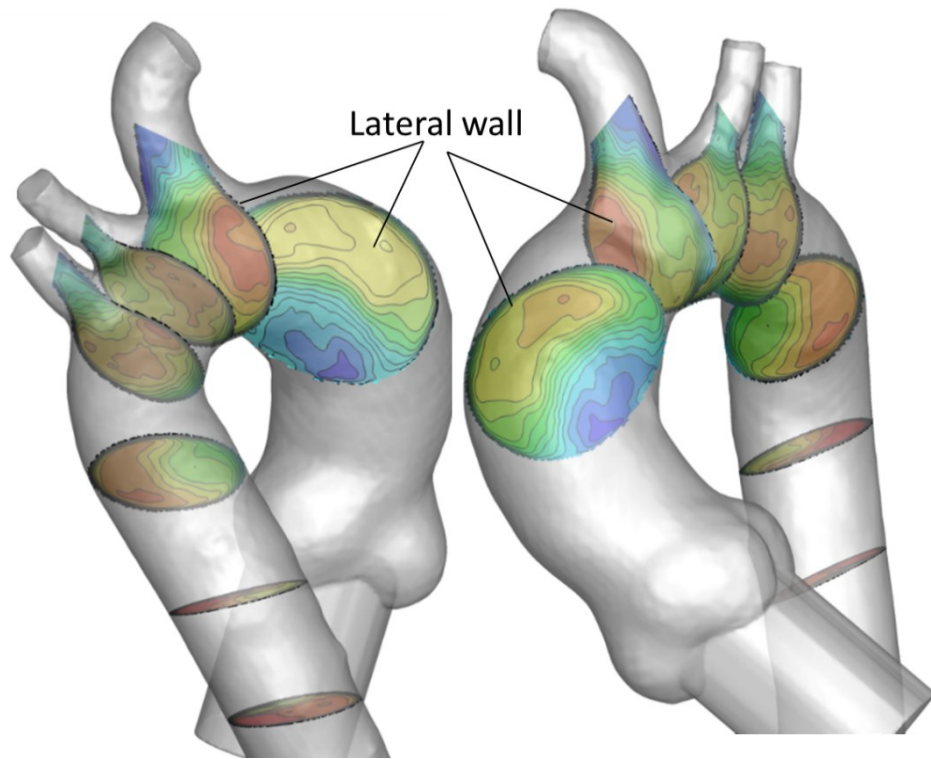


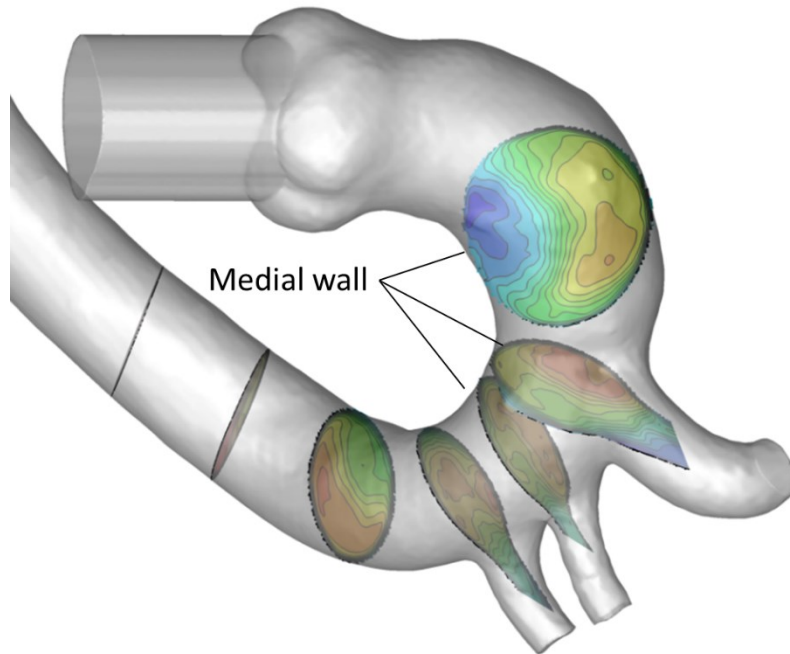
Figure 5-9 Aortic vortex dynamics and breakdown during the cardiac systole. Vortex structures are visualized by the Q criterion (where the second invariant of vorticity tensor is greater than zero i.e. $Q > 0$ (Haller, 2005; Wu et al., 2005)) colored by velocity magnitude and the numbers indicate non-dimensional times.

To investigate the flow characteristics and their relationship with contrast dispersion over time, time-averaged cross-sectional velocity contours projected normal to

the aortic cross sections are plotted in the aortic arch at three different orientations at selected reference planes (see Figure 5-10) shown in Figure 5-7c. In addition, all slices labeled as S₁-S₁₁, are shown with the contours of time-averaged velocity where in can be observed that the flow peak velocity is generally concentrated in the middle of cross section (S₁-S₃), however, upon hitting the arch wall, the time-averaged peak flow rotates towards the lateral (outer) wall. The time-averaged peak velocity maintains its location toward the outer wall until the arch has another twist after the left subclavian branch and it shifts towards the medial (inner) wall of the descending aorta. Figure 5-10 demonstrates the definition of lateral and medial wall used in this study.



(a)



(b)

Figure 5-10. Time-averaged contours of velocity at selected cross sections at different orientation of the aortic arch. Medial and Lateral walls are defined to demonstrate the tortuous nature of the aortic arch anatomy.

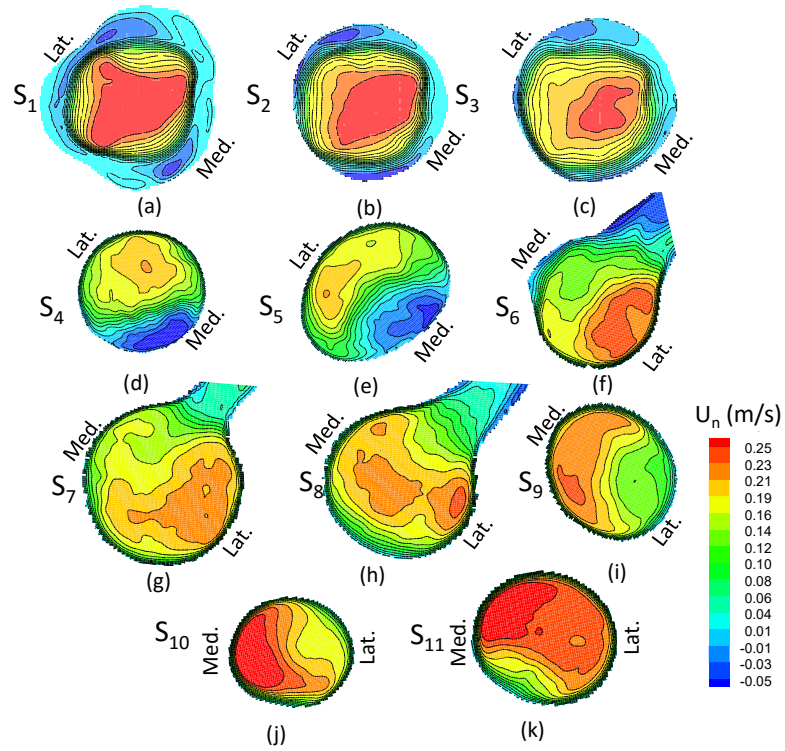


Figure 5-11. Time-averaged (cycles 2-5) contours of normal projected velocity for different normal to the flow cross-sections defined in Figure 5-7c. The lateral and medial walls denote the outer and inner walls of the aorta, respectively.

Figure 5-9 demonstrates the normal to plane (for Slices S1-S11 defined in Figure 5-7c) time averaged (cycles 2-5) vorticity. There are no coherent vortices formation at any of the slices except for some near wall local structures. The reason for this observation is further explained in the Discussion section.

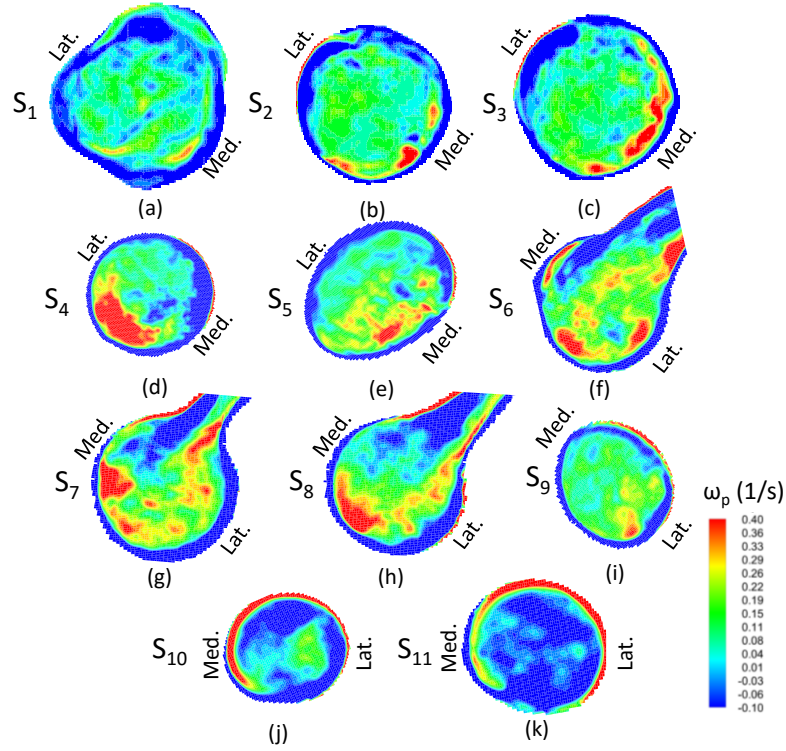


Figure 5-12. Time-averaged (cycles 2-5) contours of normal projected vorticity for different normal to the flow cross-sections defined in Figure 5-7c. The lateral and medial walls denote the outer and inner walls of the aorta, respectively.

5.3.2. Contrast Dispersion

Figure 5-14 shows the cross-sectional averaged contrast concentration time profile (AIF) at two location in the descending and ascending aorta defined in the reference planes in Figure 5-7d for $Sc=1000$. The green dashed line is the inlet contrast profile that is provided as the boundary condition. The concentration in the ascending aorta is calculated by taking the average of two cross-sectional averaged concentration defined at the ROIs shown in Figure 5-13a and b at the left main coronary ostium. Thus, C_{Asc} simply is calculated to be $C_{Asc} = \frac{C_{avg-xp} + C_{avg-yp}}{2}$. The two circles shown in this figure correspond to the cross-section of a typical coronary ostium (small circle) and a typical ROI defined at the

ascending aorta when calculating the AIF. As Seen in Figure 5-14 a and b, the smaller ROI will result in a “noisier” AIF and therefore, the larger ROI section will be considered for further analysis.

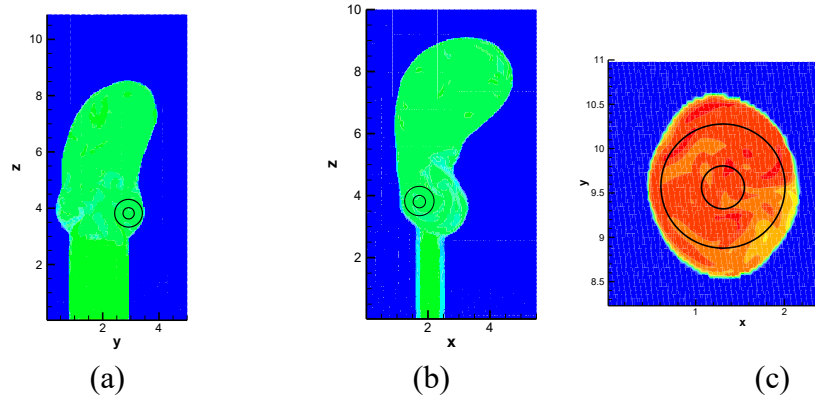
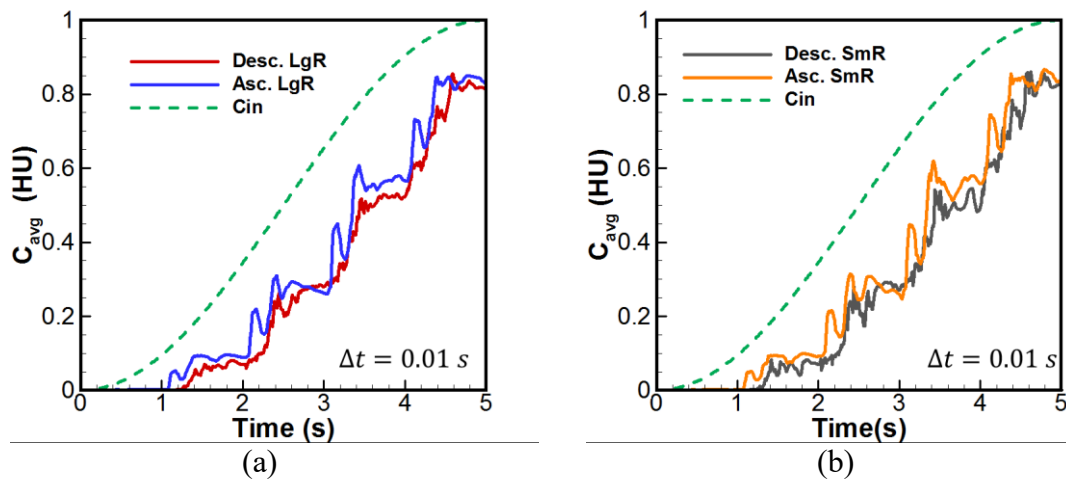


Figure 5-13. Cross sectional ROI's defined at the X-plane (a) and Y-plane (b) in ascending aorta and the normal plane (c) at the descending aorta. The reference definitions are shown in Figure 5-7d. The small and large circles are for two different sizes of ROI's to reflect the coronary ostium (small circle) and about $\frac{3}{4}$ of the size of descending aorta to calculate the cross sectional average contrast attenuation.



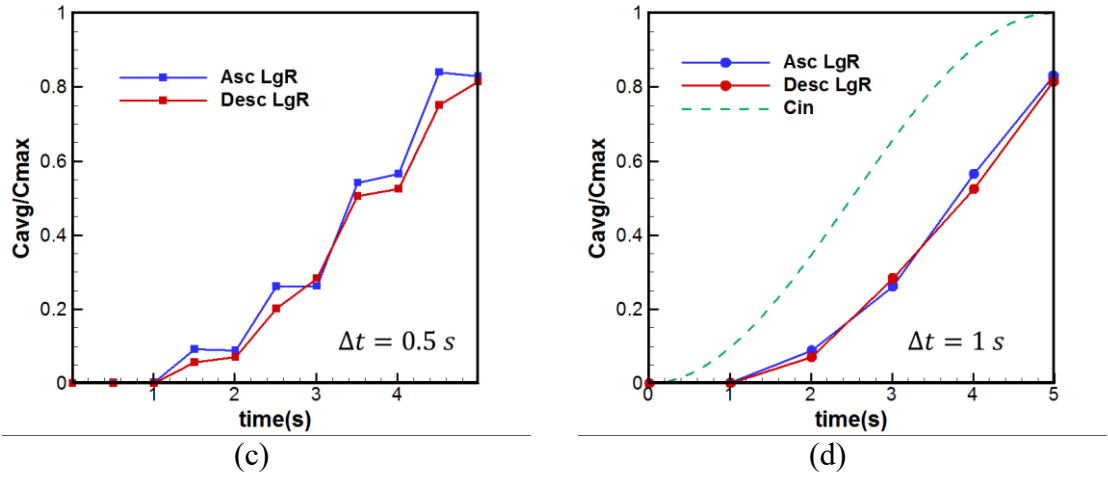


Figure 5-14. Time profile of normalized cross-sectional averaged contrast concentration at ascending and descending aorta at $\Delta t = 0.01$ s for the large ROI (a) and small ROI (b) defined in Figure 5-13 for $Sc=1000$. Sampled AIF shown in (a) for $\Delta t = 0.5$ s (c) and $\Delta t = 1$ s (d) for $Sc=1000$. The green dashed line represents the inlet contrast concentration profile. Ascending aorta concentration is calculated by: $C_{Asc} = \frac{C_{avg-Xp} + C_{avg-Yp}}{2}$.

Figure 5-14c and 5-11d show the AIF that has been sampled with $\Delta t = 0.5$ s and 1 s, respectively where the pulsatile behavior reflected on the contrast profile is no longer present and the AIF at both locations of ascending and descending aorta is similar to that of the inlet contrast profile. In addition, the AIF curves and ascending and descending aorta are compared for two $Sc=1$ (solid lines) and 1000 (dashed lines) in Figure 5-15 where there is marginal differences observed between the two cases.

Contours of time-accumulated contrast concentration are plotted (for slices S_1 - S_{11} defined in Figure 5-7c) for two $Sc=1$ and 1000 (Figure 5-16). Each slice contour level is adjusted locally to capture the contrast variation radially; however, the levels are kept constant across the two Sc numbers. Comparing each cross-section at two different Sc

numbers, we note that while there is a slight difference in the distribution of contrast, the peak location of accumulation of contrast with time is very similar in both cases.

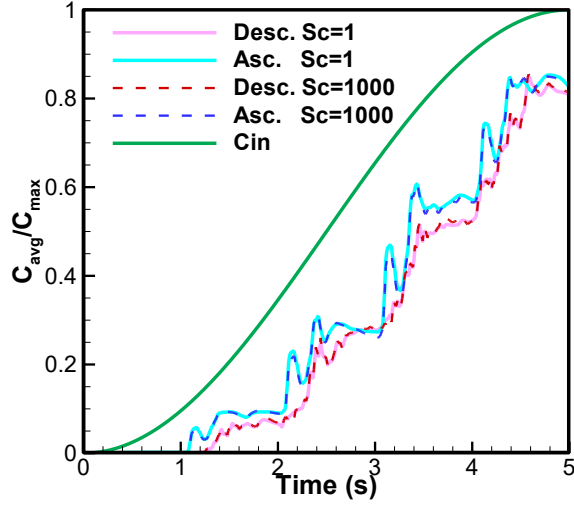
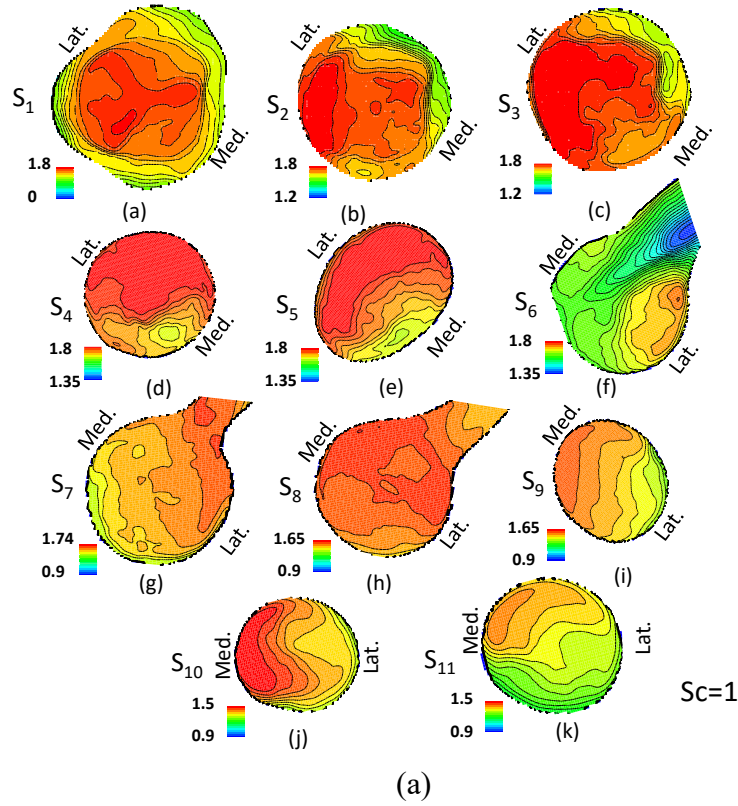


Figure 5-15. Comparison of time profile of normalized cross-sectional averaged contrast concentration at ascending and descending aorta for $Sc=1$ (solid lines) and $Sc=1000$ (dashed lines). The green solid line is the inlet contrast time profile.



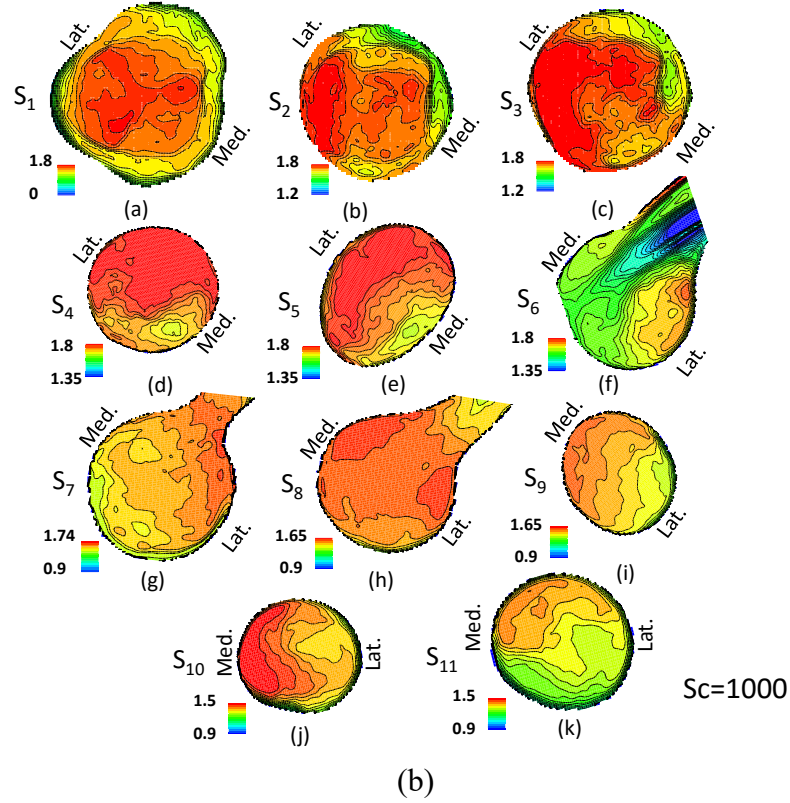


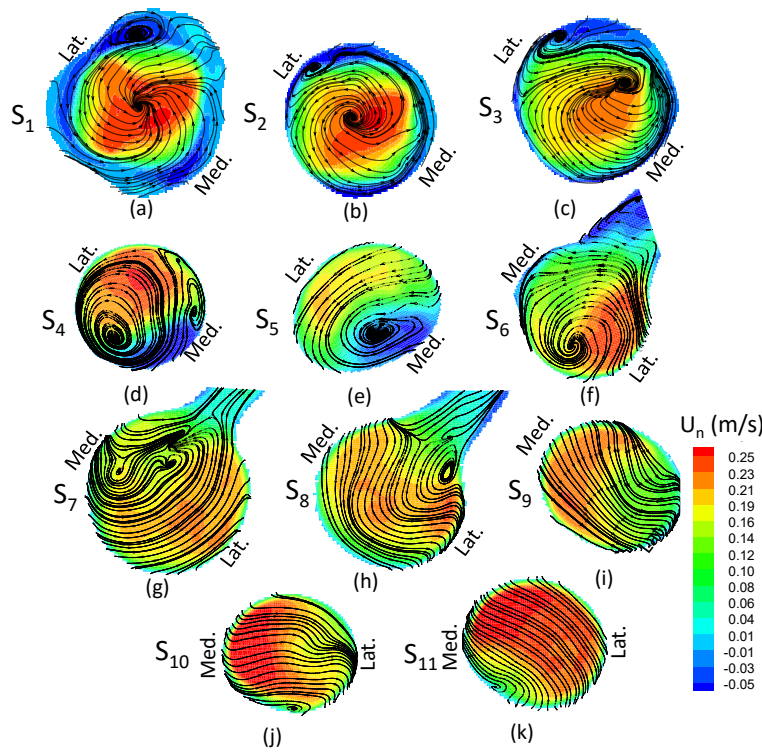
Figure 5-16. Contours of time-accumulated (cycles 2-5) contrast concentration are plotted (for slices S_1 - S_{11} defined in Figure 5-7c) for $Sc=1$ (a) and $Sc=1000$ (b)

5.1. DISCUSSION

5.1.1. Flow Pattern and its Correlation with Contrast Dispersion

Despite the large curvature, we note that the aortic arch in the current study does not form any clear Dean-type vortices (S. a Berger et al., 1983; Dean & Hurst, 1959)(similar to those observed in Mori et al., Feintuch et al, Shahcheraghi et al. and Kim et al. (Feintuch et al., 2007; Kim et al., 2004; Mori & Yamaguchi, 2002; Shahcheraghi et al., 2002)). This is primarily due to the fact that the inclusion of the aortic valve and the corresponding creation of a narrow, high velocity jet at the valve outlet leads to the situation that flow does not reach a fully developed stage before the for the Dean vortices to form in

the arch. In addition, this is reflected in Figure 5-9, where the vortex structures break down as they impact the wall and do not stretch sufficiently to create a Dean-type flow pattern. It is worth pointing out that many past studies of flow patterns in the aortic arch have employed simple models of the aorta, which crucially, lack the dynamic (opening and closing) aortic valve. The effect of the valve is to create a narrow, high velocity jet which is highly dynamic and which creates a complex pattern of recirculation as it impact the top of the ascending aorta. This complex pattern does not allow for a clear establishment of a Dean-type flow pattern in the aortic arch in our modeling study. Time-averaged tangential streamlines are plotted at each cross-section in Figure 5-17a-k where the contour levels are the same as Figure 5-11 of normal projected velocities. The streamline pattern is compared with the available computational studies of the flow in the aortic arch in Figure 5-17l-o where unlike to our simulation results, Dean-type flow pattern is present.



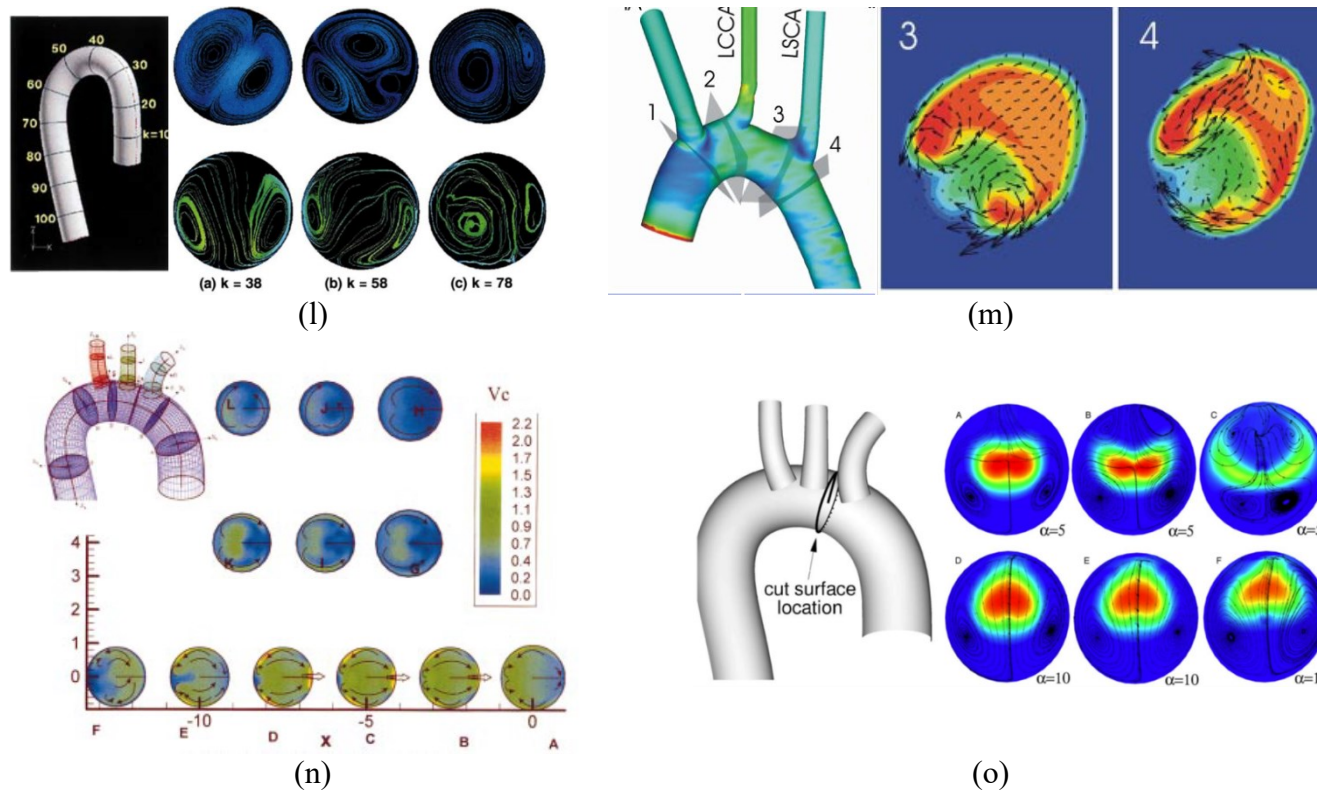


Figure 5-17. Tangential to plane time-averaged streamlines at each cross-section defined in Figure 5-7c where the background contour levels are time-averaged normal projected velocity. This figure demonstrates that there is no Dean-type flow pattern present in the aortic arch in contrary to the cases studied in Mori et al. where the streamlines are drawn in planes denoted with k and the locations for different k is shown on the (l), Feintuch et al. where the planar velocity vectors are plotted at the two reference planes 3 and 4 defined on the corresponding aorta (m), Shahcheraghi et al. where the secondary flow pattern are plotted for the defined cross-sections (n) and Kim et al. where the streamlines are shown for the location indicated in the figure with different Womersley numbers, α (o).

To compare our flow results to the available data in literature qualitatively, streamlines in the aortic arch at three different points of early systole, peak systole and late systole has been show in Figure 5-18. In a computational study, Numata et al. (Numata et al., 2016) studied blood flow through the aortic arch (including the sinus without the aortic valve) in a patient with CABG procedure with no aortic valve disease - similar to the patient

in this study. Comparing streamlines in Figure 3 for Patient 6 in Numata et al. (see Figure 5-18d) with Figure 5-18b in this study at peak systole, very similar flow pattern can be observed. However, because of the absence of the aortic valve in Numata et al. study, the spiral like motion at the valve tip is not observed.

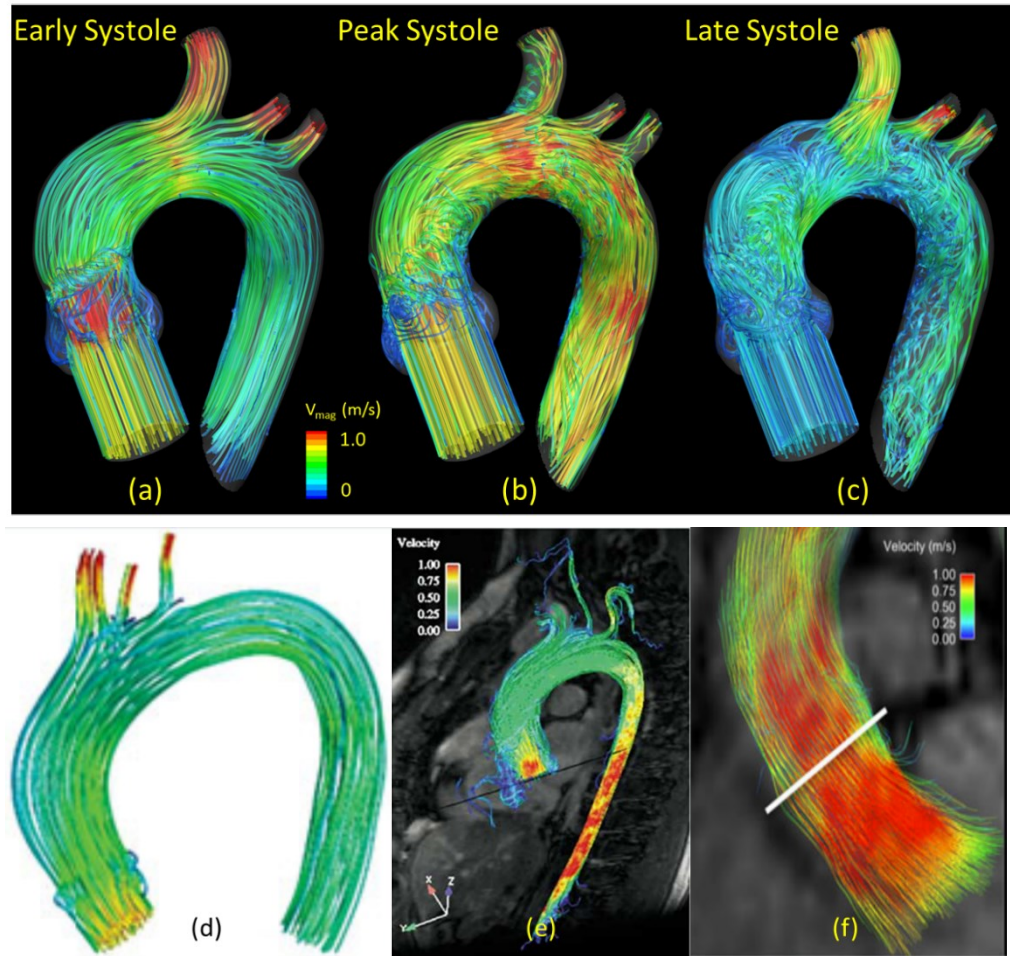


Figure 5-18. Streamlines through the aortic arch colored by velocity magnitude at three different points in early systole at $t=1.06$ s (a), mid systole at $t=1.12$ s (b) and late systole at $t=1.33$ s (c). Streamlines in available literature in the aortic arch in the computational work of Numata et al. with a patient with the CABG procedure done at peak systole (d) 4D PcMRI visualization of streamline above the valve plane level through the whole aorta in Markl et al. for a healthy patient (e) and PcMRI

In addition, Figure 5-18 can be compared with the flow visualization via PCMRI in normal patients with Figure 1. in Markl et al. (see Figure 5-18e) in the whole aorta (Markl et al., 2005) and Figure 5A. in Hope et al. (see Figure 5-18f) in the truncated ascending aorta (Hope, Wrenn, & Dyverfeldt, 2013) where the streamlines of flow velocity at the systolic are shown and are in good agreement with the present study.

While there is no clear evidence of the formation of Dean-typed vortices in the simulations here, we do note that vortices in Fig. 5-7 are not evenly distributed across the cross-section of the aorta in the arch. Instead, they indicate a tendency to accumulate on the inside wall of the arch. This is suggestive of some degree of axial swirl that is formed due to the flow through the arch and might be indicative of a weak Dean-type flow patterns. However, due to the complexity induced by the valves as well as the pulsatile nature of the flow, this pattern is difficult to confirm.

5.1.2. AIF Comparison in the Ascending and Descending Aorta

As seen in Figure 5-14, there is relatively little qualitative difference between the AIF profiles at the ascending (or coronary ostium) and descending aorta. This provide some level of support for our assumption that the AIF from the descending aorta can provide a reasonable measure of the AIF at the coronary ostium. The difference between the two AIF profiles become even smaller when the AIF is sampled at coarser time intervals (Figure 5-14c and 5-11d) that are typical of cardiac CT protocols. The time-filtered AIF is similar to what is observed clinically (Figure 5-2b) where the effect of flow puslatility is much less apparent in the contrast dispersion with time.

It is important to note that with the step-wise behavior observed in Figure 5-14a, the time point (or cardiac phase) at which the volume scan is acquired in the AIF curve

significantly influences the measured slope of the AIF. In other words, if the volume scan is taken at where the AIF is “flat”, TCG will be considerably lower compared to the TAG values in the volume scan that has been acquired at the “shoot up” part of AIF. Therefore, depending on where in the cardiac cycle the volume image is scanned, the AIF slope change needs to be accounted. To better visualize this, the AIF at descending aorta with $\Delta t = 0.5$ s has been plotted in Figure 5-19 where t_{shift} indicates the time point in cardiac cycle the volume scanned may have been acquired. In addition, the slope of the AIF at $t \approx 4$ s using a central difference in scheme has been calculated and listed in Table 5-2 where the mean value of the slope is 0.5847 ± 0.0489 (HU/s). One way of adjusting the AIF slope is to use the readily available ECG data shown in Figure 5-2d to synchronize the volume scan point to cardiac cycle. The overall lack of a significant time-lag between the two AIFs is surprising given the axial separation between these two planes and this issue is addressed in detail in Sec. 5.1.4.

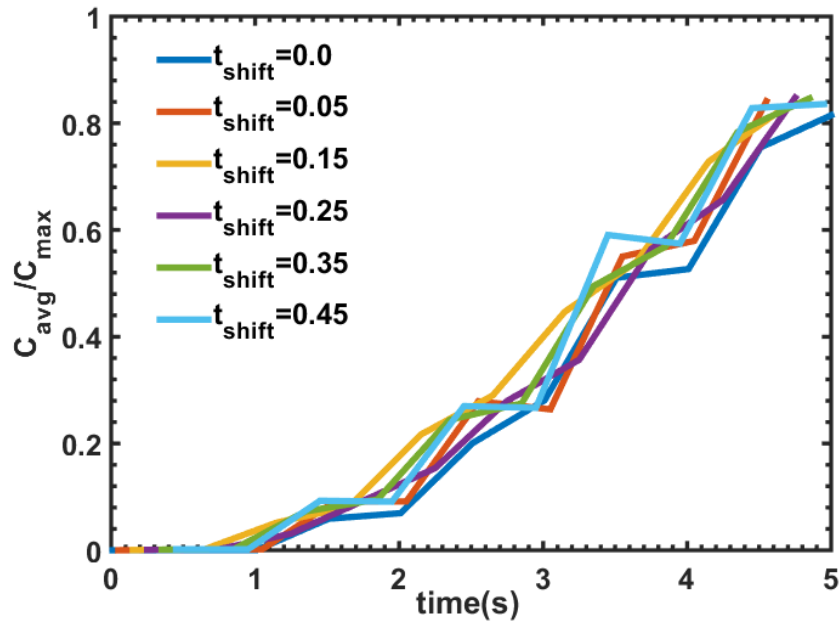


Figure 5-19. AIF at descending aorta with sampling rate of $\Delta t = 0.5$ s where the starting point is shifted by 0.1 second to demonstrate that depending on the time point in cardiac cycle, the AIF slope can vary significantly.

Table 5-2. List of calculated slope of the AIF (dC/dt) at $t \approx 4$ s for the shifted AIF in cardiac cycle

$t_{shift}(s)$	0	0.05	0.15	0.25	0.35	0.45
$dC/dt(t$	0.488	0.609	0.625	0.586	0.596	0.602
$\approx 4.0)(HU/s)$	3	2	0	8	6	2

5.1.3. Effect of Schmidt Number on Contrast Dispersion and Diffusion

Given that a number of different contrast agents are available for clinical use and that definitive information on the diffusivity coefficient (or Sc number) is not fully available(Durant et al., 2008; Kim et al., 2004), two simulations with highly disparate (Sc=1 and 1000) values of Sc have been performed. Interestingly, as seen in Figure 5-15, even with the three-orders of magnitude difference in the Sc numbers, the arterial input functions and the ascending and descending aorta are virtually unchanged. Similarly, when computing time-accumulated contrast concentration (Figure 5-16) at different slices along the aortic arch, the radial contrast dispersion have very similar pattern. As expected, in case of Sc=1 because of higher diffusivity, the contrast has a more homogenous mixing compared to the case of Sc=1000 confirming that the different contrast agents with different molecular diffusion coefficient will not influence the contrast dispersion

radically. This indicates that the choice of contrast agent used in patients will not have a dramatic effect on the AIF formation and contrast dispersion through the aorta. A caveat in the current study is that the effect of numerical diffusion on the higher Schmidt number simulation is not fully characterized. ViCard3D employs a slightly upwinded scheme for these simulations and as the molecular diffusivity is reduced, numerical diffusivity would increase in magnitude. This effect could be investigated by modulating the upwinding and/or changing resolution but this has not been pursued in the current study.

5.1.4. Transient Time vs. Transport Time

The observed close match between the AIFs at the ascending and descending aortas is somewhat surprising given the average flow velocity and the axial separation of these two locations. From the velocity profile shown in Figure 5-4, the average velocity of the flow entering the aorta is about 18 cm/s. The approximate axial distance between the two planes where the AIFs are measured is about 16 cm. If the contrast is travelling at this average velocity, then the time-lag between the two AIFs should be about $(16\text{cm}) / (18\text{cm/s}) = 0.88$ seconds. A visual assessment of the two AIFs in Figure 5-14 and Figure 5-15 suggests that the actual time-lag between the two is significantly smaller than 0.88 seconds. This simple analysis however makes a number of assumptions including: that the flow profile is uniform across the cross-section, the cross-sectional area is constant along the aorta, unsteady effects can be neglected and that contrast dispersion is entirely determined by advection. From the view point of cardiac imaging, this observed behavior is intriguing and worthy of further investigation and we explore this issue in detail here.

In order to conduct a quantitative analysis of this issue, two variables are computed: the transient time, $\tau_{transient}$, is the time that takes for a contrast particle at Slice 1 (S_1) to

travel to Slice 11 (S_{11}) (defined in Figure 5-7c) and $\tau_{transport}$, is the observed time-lag in the AIFs at the ascending and descending aortas. This can be determined by computing the cross-correlation between the two AIF curves as a function of the time lag τ as follows:

$$E(\tau) = \text{mean}(|C_{Asc}(t) - C_{Dec}(t - \tau)|)$$

$\tau_{transport}$ is then estimated as the value of τ that minimizes $E(\tau)$. Figure 5-15 shows the variation of $E(\tau)$ with τ for the two different Sc number. We note that first, the two Schmidt number simulations show very similar variations in $E(\tau)$. Second, the values of $\tau_{transport}$ estimated from these curves are $\tau_{transport} = 0.19s$ and $\tau_{transport} = 0.18s$ for $Sc=1$ and 1000 , respectively. This very short transport time-lag, which is about $1/5^{\text{th}}$ of our cardiac cycle is extremely good news for TAFE since it implied that temporal gradients of the contrast concentration estimated from the descending aorta AIF will provide a reasonably good estimate of the corresponding values at the coronary ostium.

The transient time involves finding a pathline (see Figure 5-20b) based on cross-sectional average at each slice defined in Figure 5-7c and is calculated by the following steps:

- Linear interpolation of average velocities $u_{avg}(s, t)$ between each consecutive

$$\text{slice with } u_{avg}^{S_i \rightarrow i+1}(s(t), t) = u_{avg}^{S_i}(t)(\alpha) + u_{avg}^{S_{i+1}}(t)(1 - \alpha) \text{ where } \alpha = \frac{|S_i|}{|S_{i+1} - S_i|}$$

and S_i is the axial location down the centerline of each slice (Figure 5-20c).

- Calculation of the total interpolated velocity between slices S_1 and S_{11} by:

$$u_{avg}^{S_1 \rightarrow N} = \sum_{i=1}^N u_{avg}^{S_i \rightarrow i+1}(S(t), t)$$

- Determining the distance between the start and end slices as a function of time by:

$$S_{pathline}(t) = \sum_{j=1}^{t_{end}} \Delta t \cdot u_{avg}(s_j, t_j) + s_{j-1}$$

- Transient time $\tau_{transient}$ is then t_j when $S_{pathline}(\tau_{transient}) = S_{11}$

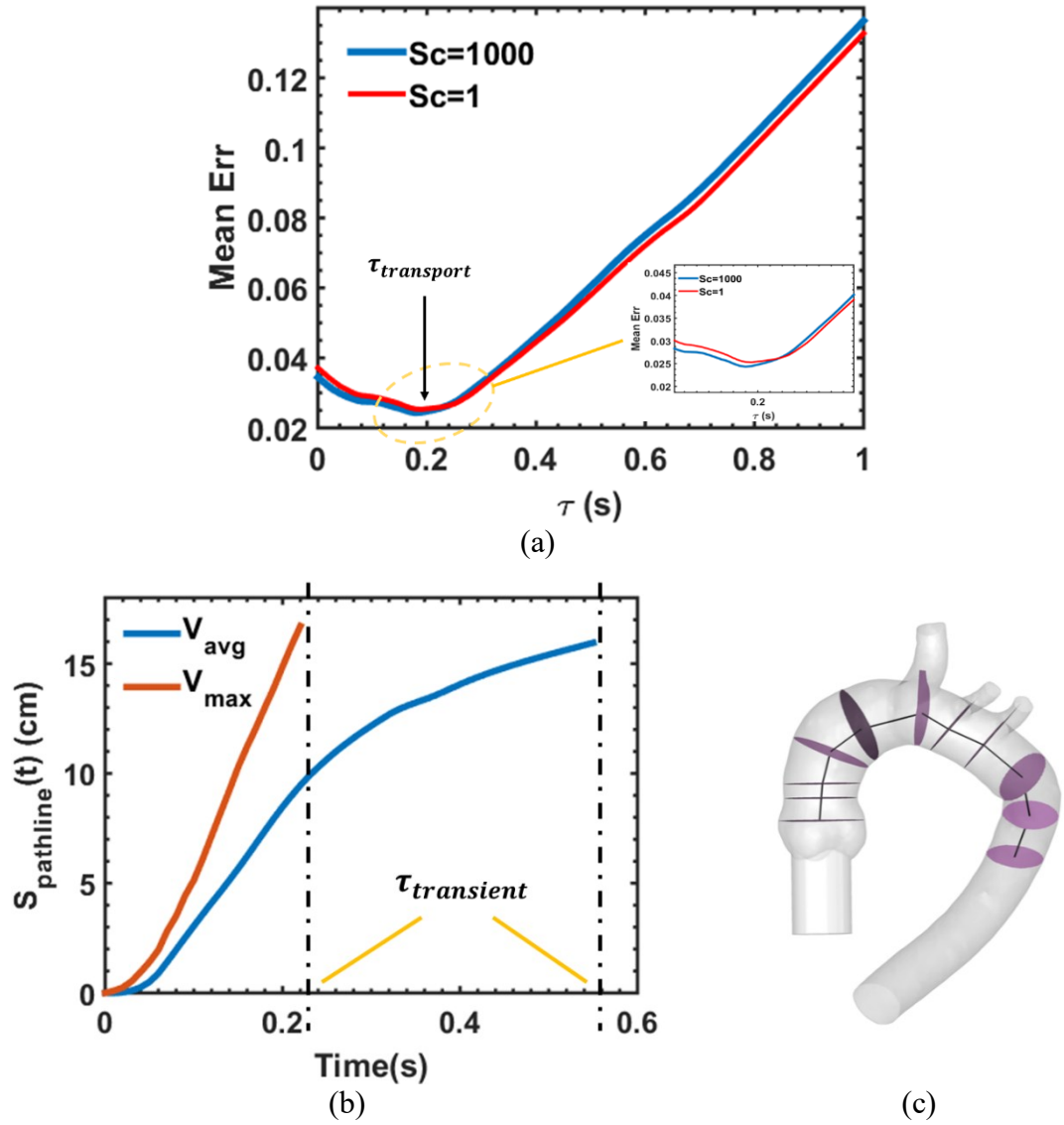


Figure 5-20.(a) Mean error between the two AIF curves at ascending and descending aorta. The minimum in this plot is defined as the transport with very close values for $Sc=1$ and 1000. The concave part of the plot is zoomed in to see the difference in the curve for the two Sc numbers. (b) Pathline calculated between the first slice (S_1) and last slice (S_{11}) shown in Figure 5-7c where the transient time is the time that takes for a fluid particle to travel on the pathline. (c) Centerline defined between each slice on the aortic arch.

With the above described method, the transient time is calculated to be $\tau_{transient} = 0.55$ s. Comparing the calculated reference times, it is evident that the transient time is longer than the transport time where $\tau_{transient} \approx 3 \tau_{transport}$. This leads to the interesting and somewhat puzzling conclusion that the contrast disperses faster than would be predicted by the average convective velocity. This naturally raises the question as to the physical mechanism(s) for this seeming inconsistency between the two time scales.

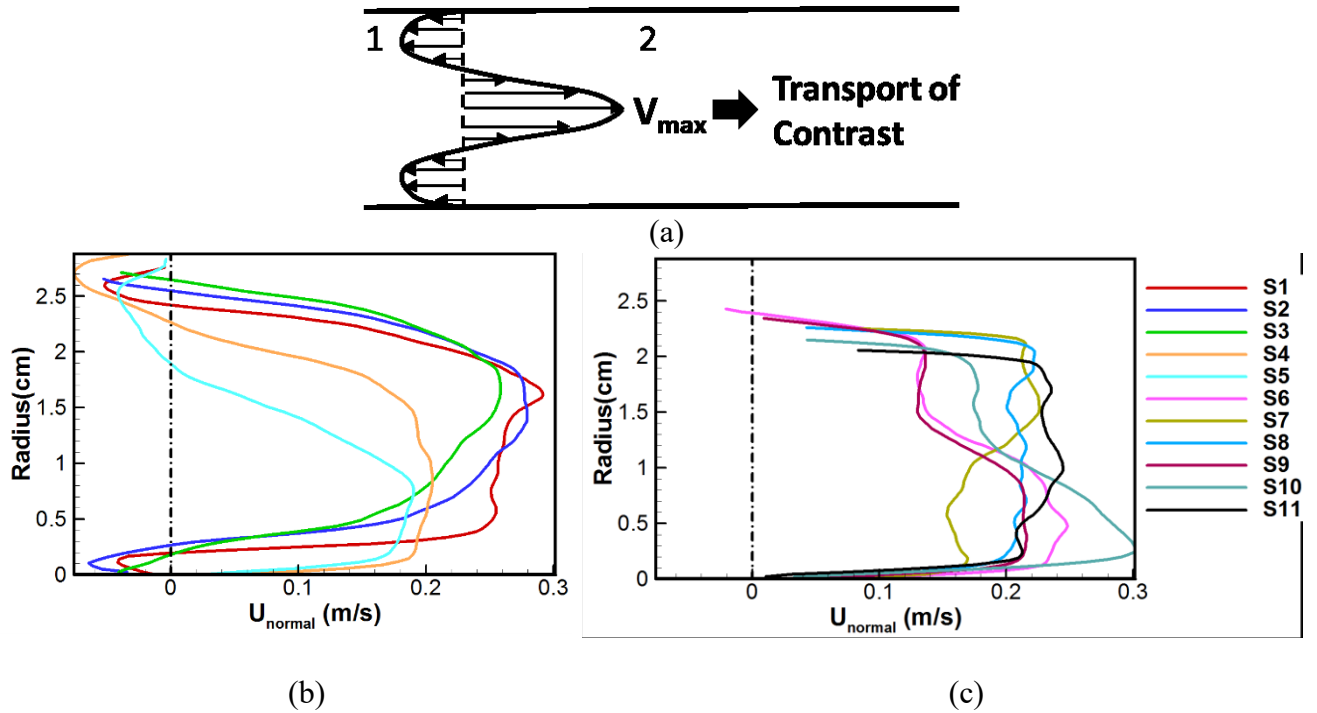


Figure 5-21. (a) Schematic of velocity profile with pulsatile (Womersely flow) characteristic. The maximum flow V_{max} is much higher than the mean flow velocity and is transporting the contrast as a faster velocity. Radial time-averaged normal velocity show similar radial profile as the schematic in (a) and are shown for Slices 1 to 5 in (b) and 6-11 in (c)

As pointed out earlier, the non-uniformity of the flow across the cross-section could possibly result in a significant different in the two transit times. In fact, it can readily be

shown that the observed speed of transport of a scalar could be quite different from the average speed of the flow by considering the schematic below (Figure 5-21a) that shows a flow with nearly zero mean velocity. Despite the velocity being nearly zero, the contrast in the center of the pipe will be convected to the right in this flow at a speed that is close to V_{\max} . This indicates that an upper estimate of the contrast advection speed might be obtained by considering the maximum velocity at a given cross-section.

Figure 5-21a and 5-20b show velocity profiles at selected planes S₁-S₅ and S₆-S₁₁ in the aorta and these figures clearly show that the velocity profile in the aorta are, not surprisingly, highly non-uniform. Furthermore, comparing time-averaged velocity cross-sectional contours in Figure 5-11 and time-accumulation of contrast concentration cross-sectional contours in Figure 5-16a and Figure 5-16b, the peak regions are at very similar locations implying that the flow with higher velocity transport majority of contrast. However, because of the incoherent time-averaged vorticity at each cross-section, there seems to be no correlation between the cross-section contours shown in Figure 5-12 and Figure 5-15. In order to test the degree to which this flow non-uniformity might contribute to the discrepancy in the time scales, we have recomputed $\tau_{transient}$ by using the peak velocity (instead of the cross-sectional average) at each location. Figure 5-20a shows the particle “flight” with this calculation and we find that this gives us a $\tau_{transient}$ of 0.21 s. The new transient time calculated by the peak velocity is now much closer to the calculated transport time ($\tau_{transient} \approx 1.2 \tau_{transport}$) indicating that the contrast is transported much faster than the mean bulk flow and is primarily transported by the fastest flow regions.

5.2. SUMMARY

Hemodynamics in the aortic arch has been investigated here using high resolution simulations employing an immersed boundary method based flow solver. The flow field is compared qualitatively with the existing literature shows reasonable agreement. In addition, contrast dispersion has been studied. The key conclusions of the current study are:

- a) The simulations do not show a strong and/or noticeable Dean-vortex type flow pattern in the aortic arch. This might be a result of the inclusion of the dynamically moving aortic valve and/or pulsatility, both of which create complex, temporally evolving swirling flow patterns in the arch;
- b) The arterial input function at the ascending and descending aorta have very similar shape and the time-lag between the two AIFs is a fraction of the cardiac cycle time. Therefore, using the readily available data from the descending aorta instead of ascending aorta (or coronary ostium) should not contribute to significant errors in TAFE;
- c) Comparing the AIF curves along with radial contrast dispersion for different cross-sections along the aortic arch for two cases with $Sc=1$ and 100, it can be concluded that there is a negligible effect of molecular diffusivity of contrast agent. This is suggestive of the fact that the conclusions reached here might be applicable to a wide variety of available contrast agents used in cardiac imaging. The effect of numerical diffusion at high Schmidt numbers remains to be explored.

- d) Concentration accumulation of the contrast agent with time at each cross-section along the aortic arch can be correlated to the peak time-averaged normal projected velocity indicating that contrast is convected rapidly by the high speed localized “current” in the aorta. .
- e) Time scale for contrast dispersion from ascending to descending aorta seems to be approximately 3 times faster than the time scale of fluid particles traveling the same path with a cross-sectional average velocity. However, when the transport time of contrast is compared with the fluid particles traveling with cross-sectional peak velocity, the two time scales are very close implying that high concentration contrast is carried by the localized high velocity flow currents in the aorta thereby reducing the time-lag between the two AIF to a value that is a fraction of a cardiac cycle. This is highly advantageous for the TAFE formulation.

CHAPTER 6: CONCLUSIONS

6.1. SUMMARY

In the present study, original research has been conducted using both experimental assays and computational fluid dynamics to examine methods for estimating coronary flow velocity from contrast dispersion patterns imaged in CT angiography. The key findings of the study are as follows:

- 1) Transluminal contrast gradients (TCG) do encode for coronary flow velocity. Our original hypothesis that a higher velocity in the coronary vessel will tend to “stretch” (and therefore decrease) the contrast agent gradient whereas a lower flow velocity will tend to steepen (and increase) the gradient, is borne in both simulations and experiments.
- 2) The study reveals that TCG is only one piece of the puzzle and that the arterial input function (AIF) at the coronary ostium, and more specifically, the temporal gradient of this AIF, is an equally important aspect of this coronary contrast dispersion. Past studies have not appreciated the importance of this AIF and therefore neither controlled for, nor measured the AIF.
- 3) Interestingly, AIF is relatively easily recorded in a typical coronary CT study and by employing simple ideas of contrast dispersion, we can find an analytical relationship between these contrast gradients and coronary flow velocity as follows:

$$V_{coronary} = -\frac{(\partial c / \partial t)}{(\partial c / \partial x)}$$

and this estimate, as well as the associated method used to obtain the estimate is called transluminal attenuation flow encoding or TAFE.

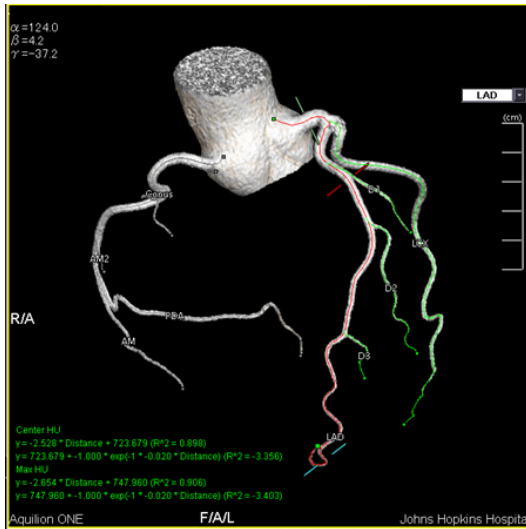
- 4) Simulations as well as experiments with CT compatible phantoms indicate that TAFE is indeed capable of providing relatively accurate estimates of flow velocity and in doing so, might provide a power non-invasive diagnosis of coronary artery disease.
- 5) The study however, also reveals a number of outstanding issues that limit the overall accuracy of the TAFE estimates. Chief among these are imaging artifacts such as partial-volume averaging, kernel filtering and image reconstruction artifacts. The current research has made some headway in quantifying, and even correcting for these effects, but more work needs to be done in the future.
- 6) The study of contrast dispersion in the aortic arch has revealed interesting flow related dispersion patterns that might inform future studies and methods. In the context of TAFE, this study indicates that the AIF recorded at the downstream aorta is a good approximation to the AIF at the coronary ostium.

6.2. Ongoing and Future Work

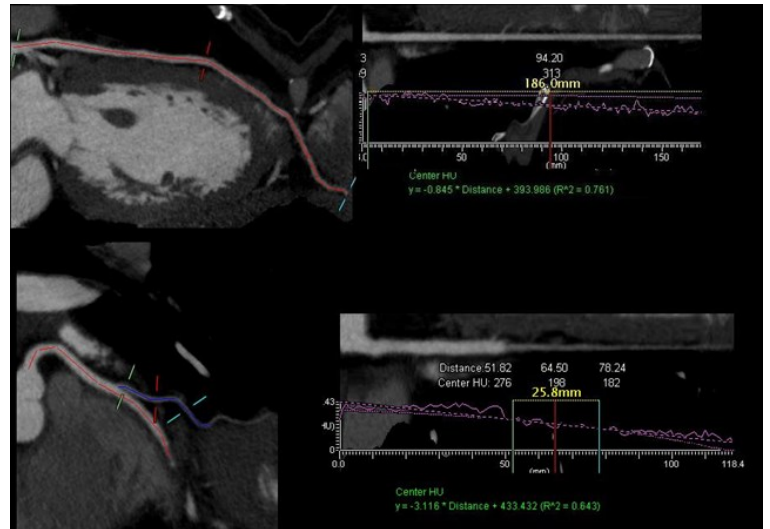
The next step in validating the TAFE formulation is to test it in clinical studies. This work requires analyzing patients with coronary artery disease (CAD) that have had CT angiograms with the AIF available at the descending aorta. These images were taken part of the Core320 trial- a multi-center trial comparing the effectiveness of 320-multidetector row dynamic volume CT to SPECT technology in patients with known or suspected CAD. These images are available to us via a collaboration with the National Institute of Blood, Lung and Heart (NHLBI) at National Institute of Health (NIH).

There are several steps involved in TAFE analysis (see Figure 6-1):

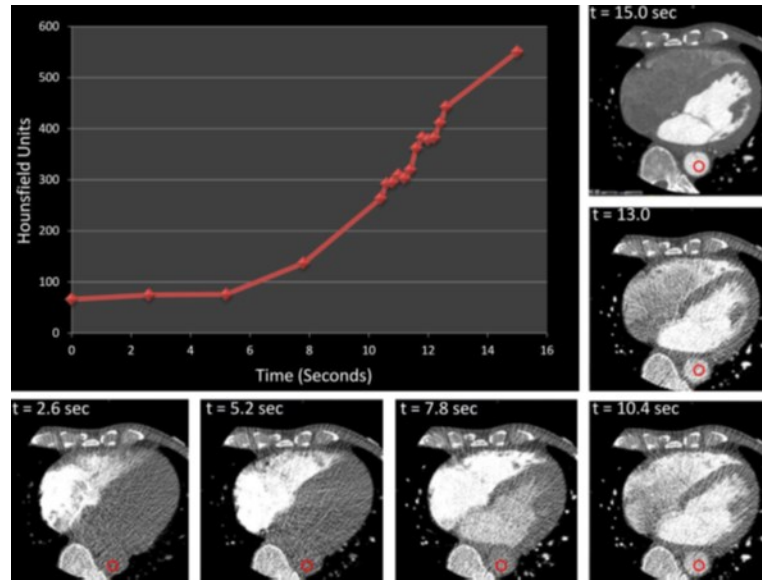
- 1) Reconstruct volumetric and dynamic images of the whole heart scan with the filtering kernel that's best fitted for this study
- 2) Track each vessel and its branches of interest in the volumetric CT scans
- 3) Find the center point at each cross-section in the tracked vessels
- 4) Edit the lumen of each vessel based manually based on the lumen attenuation, center-point and the cross-sectional area
- 5) Measure AIF available from the sure-start (dynamic) images
- 6) Calculate TCG from the output files created in steps 1-4 (done using a custom made software by Toshiba (Otagawa, Japan) by linearly interpolating the lumen mean attenuation level (in HU) along the centerline of each vessel.
- 7) Calculate the slope of the fitted AIF curve
- 8) Calculate the average flow rate in vessel and its branches based on the formulation developed on Chapter 2.
- 9) Add up all the flowrates measured to get the total flow through the main branch.



(a)



(b)



(c)

Figure 6-1. Steps involved in TAFE analysis with tracking the vessel and determining the centerline (a) editing the lumen wall and finding the TCG along the centerline of each vessel with its branches(b) and measuring AIF at the descending aorta (c). Images taken from (Lardo, Rahsepar, Seo, Eslami, Korley, Kishi, et al., 2015)

Once, the TAFE analysis is completed, these flow rates are going to be compared against a previously measured total flow at each myocardial bed region using stress cardiac MRI (CMR) perfusion images of the corresponding patients. Our collaborators at NIH have developed a methodology to non-invasively measure the total myocardial blood flow and have previously validated this method against a standard reference of fluorescent microsphere measurements in canine models (L.-Y. Hsu et al., 2012). In this method, myocardial time-signal intensity curves of the images were quantified on a pixel-by-pixel basis using a model-constrained deconvolution analysis. A sector-wise MBF measurements from CMR perfusion at endocardial and epicardial borders of the left ventricle (LV) myocardium were manually traced on the image series (Argus CMR software-Syngo, Siemens Healthcare, Erlangen, Germany). Figure 6-2a and Figure 6-2b

show the CMR perfusion mapping of a patient with left circumflex (LCX) moderate stenosis and a patient with no substantial CAD, respectively at the rest condition. These mappings are shown for three different levels of basal, medial and apical regions in the long axis of the LV and then added up for each coronary territory. As seen in Figure 6-2a, the LCX region (shown in yellow square) gains very small flow consistently in the three basal, medial and apical levels where as no such lack of flow region is observable in the “normal” patient in Figure 6-2b.

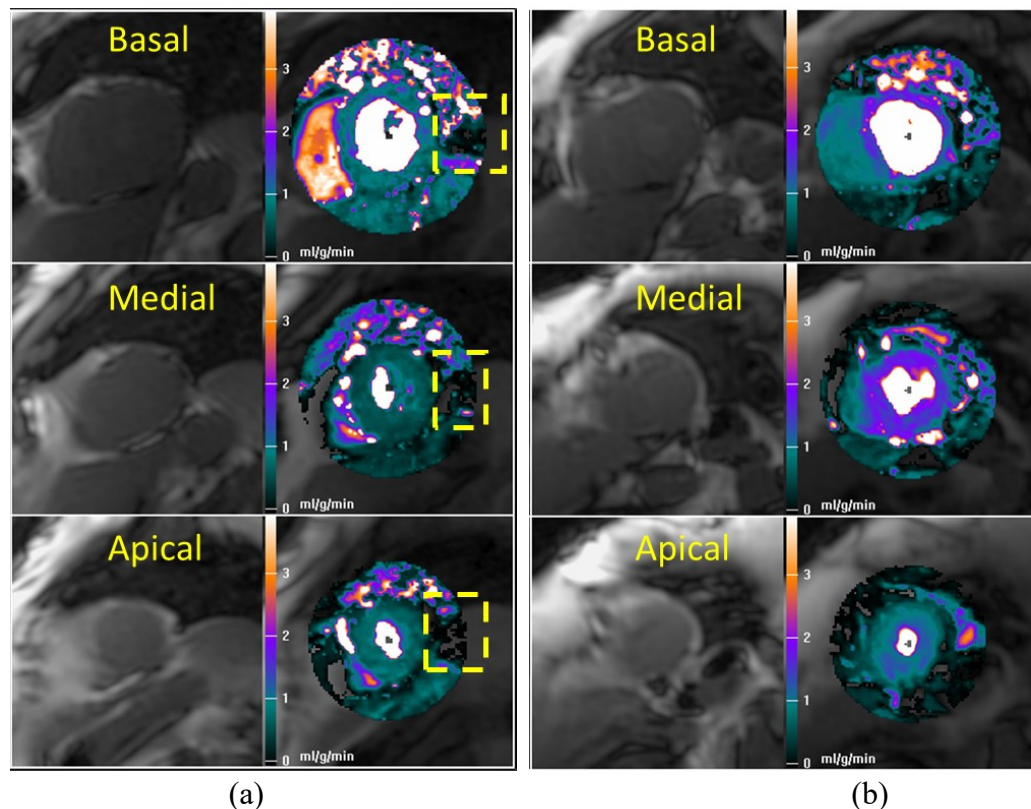


Figure 6-2. Two representative case of CMR perfusion cases for a patient with severe LCX disease (a) and patient with no significant CAD (b).

LIST OF REFERENCES

- Abd, T. T., & George, R. T. (2015). Association of coronary plaque burden with fractional flow reserve: should we keep attempting to derive physiology from anatomy? *Cardiovascular Diagnosis and Therapy*, 5(1), 67–70. <http://doi.org/10.3978/j.issn.2223-3652.2015.01.07>
- Ahmed, S. A., & Giddens, D. P. (1984). Pulsatile poststenotic flow studies with laser Doppler anemometry. *Journal of Biomechanics*, 17(9), 695–705. [http://doi.org/10.1016/0021-9290\(84\)90123-4](http://doi.org/10.1016/0021-9290(84)90123-4)
- Akbudak, E., & Conturo, T. E. (1996). Arterial input functions from MR phase imaging. *Magnetic Resonance in Medicine: Official Journal of the Society of Magnetic Resonance in Medicine / Society of Magnetic Resonance in Medicine*, 36(6), 809–815. <http://doi.org/10.1002/mrm.1910360602>
- Al-Shakhrah, I., & Al-Obaidi, T. (2003). Common artifacts in computerized tomography: A review. *Applied Radiology*, 32(8), 25–30.
- Angelsen, B. A. J., & Brubakk, A. O. (1976). Transcutaneous measurement of blood flow velocity in the human aorta. *Cardiovascular Research*, 10(3), 368–379.
- Appel, A. (1968). Some Techniques for Shading Machine Renderings of Solids. AFIPS Conference Proc.
- Bajcsy, R., & Kovačič, S. (1989). Multiresolution elastic matching. *Computer Vision, Graphics, and Image Processing*, 46(1), 1–21. [http://doi.org/10.1016/S0734-189X\(89\)80014-3](http://doi.org/10.1016/S0734-189X(89)80014-3)
- Barfett, J. J. ohn, Velauthapillai, N., Fierstra, J., Crawley, A., Coolens, C., Crean, A., ... Mikulis, D. (2014). Intra-vascular blood velocity and volumetric flow rate calculated from dynamic 4D CT angiography using a time of flight technique. *The International Journal of Cardiovascular Imaging*, 30(7), 1383–1392. <http://doi.org/10.1007/s10554-014-0471-3>
- Barrett, J. F., & Keat, N. (2004). Artifacts in CT: recognition and avoidance. *Radiographics*, 24(6), 1679–91. <http://doi.org/10.1148/rg.246045065>
- Barth, T.J, Jespersen, D. . (1989). The design and application of upwind schemes on unstructured meshes. *AIAA Paper*, (89-0366).
- Becker, C. R., Ohnesorge, B. M., Schoepf, U. J., & Reiser, M. F. (2000). Current development of cardiac imaging with multidetector-row CT. *European Journal of Radiology*, 36(2), 97–103. Retrieved from <http://www.ncbi.nlm.nih.gov/pubmed/11116173>
- Beg, M. F., Miller, M. I., Troune, A., & Younes, L. (2005). Computing large deformation metric mappings via geodesic flows of diffeomorphisms. *International Journal of Computer Vision*, 61(2), 139–157. <http://doi.org/10.1023/B:VISI.0000043755.93987.aa>
- Bellhouse, B. J., & Talbot, L. (1969). Fluid mechanics of the aortic valve. *J. Fluid Mech.*, 35(4), 721–735. Retrieved from <http://www.ncbi.nlm.nih.gov/pubmed/2974076>
- Berger, A., Botman, K. J., & MacCarthy, P. A. (2005). Long-Term Clinical Outcome After Fractional Flow Reserve-Guided Percutaneous Coronary Intervention in Patients With Multivessel Disease. *ACC Current Journal Review*, 14(11), 48–49. <http://doi.org/10.1016/j.accreview.2005.10.050>
- Berger, S. a, Berger, S. a, Talbot, L., Talbot, L., Yao, L. S., & Yao, L. S. (1983). Flow in

- Curved Pipes. *Annual Review of Fluid Mechanics*, 15, 461–512. <http://doi.org/10.1146/annurev.fl.15.010183.002333>
- Besi, P. J., & Mckay, N. D. (1992). A Method for Registration of 3-D Shapes 1 Introduction 2 Literature Review. *Robot. Tentat.*, 1611, 586–606.
- Bishop, A. H., & Samady, H. (2004). Fractional flow reserve: critical review of an important physiologic adjunct to angiography. *American Heart Journal*, 147(5), 792–802. <http://doi.org/10.1016/j.ahj.2003.12.009>
- Blankstein, R. (2012). Introduction to noninvasive cardiac imaging. *Circulation*, 125(3), 267–272. <http://doi.org/10.1161/CIRCULATIONAHA.110.017665>
- Blankstein, R., Shturman, L. D., Rogers, I. S., Rocha-Filho, J. A., Okada, D. R., Sarwar, A., ... Cury, R. C. (2009). Adenosine-Induced Stress Myocardial Perfusion Imaging Using Dual-Source Cardiac Computed Tomography. *Journal of the American College of Cardiology*, 54(12), 1072–1084. <http://doi.org/10.1016/j.jacc.2009.06.014>
- Bogren, H. G., & Buonocore, M. H. (1994). Blood flow measurements in the aorta and major arteries with MR velocity mapping. *Journal of Magnetic Resonance Imaging : JMRI*, 4(2), 119–30. <http://doi.org/10.1002/jmri.1880040204>
- Canny, J. (1986). A computational approach to edge detection. *IEEE Transactions on Pattern Analysis and Machine Intelligence*, 8(6), 679–698. <http://doi.org/10.1109/TPAMI.1986.4767851>
- Chan, T. F., & Vese, L. A. (2001). Active contours without edges. *IEEE Transactions on Image Processing*, 10(2), 266–277. <http://doi.org/10.1109/83.902291>
- Choi, J.-H., Koo, B.-K., Yoon, Y. E., Min, J. K., Song, Y.-B., Hahn, J.-Y., ... Choe, Y. H. (2012). Diagnostic performance of intracoronary gradient-based methods by coronary computed tomography angiography for the evaluation of physiologically significant coronary artery stenoses: a validation study with fractional flow reserve. *European Heart Journal Cardiovascular Imaging*, 13(12), 1001–7. <http://doi.org/10.1093/ehjci/jes130>
- Choi, J.-H., Min, J. K., Labounty, T. M., Lin, F. Y., Mendoza, D. D., Shin, D. H., ... Choe, Y. H. (2011). Intracoronary transluminal attenuation gradient in coronary CT angiography for determining coronary artery stenosis. *JACC. Cardiovascular Imaging*, 4(11), 1149–57. <http://doi.org/10.1016/j.jcmg.2011.09.006>
- Chow, B. J. W., Kass, M., Gagné, O., Chen, L., Yam, Y., Dick, A., & Wells, G. a. (2011). Can differences in corrected coronary opacification measured with computed tomography predict resting coronary artery flow? *Journal of the American College of Cardiology*, 57(11), 1280–8. <http://doi.org/10.1016/j.jacc.2010.09.072>
- Chung, J., & Hulbert, G. M. (1993). A Time Integration Algorithm for Structural Dynamics With Improved Numerical Dissipation: The Generalized-alpha Method. *ASME-Journal of Applide Mechancis*, 60, 371–375.
- Clark, C., & Schultz, D. L. (1973). Velocity distribution in aortic flow. *Cardiovascular Research*, 7(5), 601–613. <http://doi.org/10.1093/cvrese/7.5.601>
- Cury, R. C., Magalhães, T. A., Paladino, A. T., Shiozaki, A. A., Perini, M., Senra, T., ... Rochitte, C. E. (2011). Dipyridamole stress and rest transmural myocardial perfusion ratio evaluation by 64 detector-row computed tomography. *Journal of Cardiovascular Computed Tomography*, 5(6), 443–448. <http://doi.org/10.1016/j.jcct.2011.10.012>
- De Hart, J., Baaijens, F. P. T., Peters, G. W. M., & Schreurs, P. J. G. (2003). A computational fluid-structure interaction analysis of a fiber-reinforced stentless aortic

- valve. *Journal of Biomechanics*, 36(5), 699–712. [http://doi.org/10.1016/S0021-9290\(02\)00448-7](http://doi.org/10.1016/S0021-9290(02)00448-7)
- De Hart, J., Peters, G. W. M., Schreurs, P. J. G., & Baaijens, F. P. T. (2003). A three-dimensional computational analysis of fluid-structure interaction in the aortic valve. *Journal of Biomechanics*, 36(1), 103–112. [http://doi.org/10.1016/S0021-9290\(02\)00244-0](http://doi.org/10.1016/S0021-9290(02)00244-0)
- Dean, W. R., & Hurst, J. . (1959). Note on the Motion of Fluid in a Curved Pipe. *Mathematika*, 6, 77–85.
- Desjardins, B., & Kazerooni, E. a. (2004). ECG-gated cardiac CT. *AJR. American Journal of Roentgenology*, 182(4), 993–1010.
- Durant, J., Waechter, I., Hermans, R., Weese, J., & Aach, T. (2008). Toward Quantitative Virtual Angiography: Evaluation with in vitro studies. Philips Research Europe , Aachen , Germany Institute of Imaging and Computer Vision , RWTH Aachen University , Aachen , Germany Centre for Medical Image Computing , University Coll, 632–635.
- Eslami, P., Seo, J.-H., Rahsepar, A. A., George, R., Lardo, A. C., & Mittal, R. (2015). Computational Study of Computed Tomography Contrast Gradients in Models of Stenosed Coronary Arteries. *Journal of Biomechanical Engineering*, 137(9), 091002. <http://doi.org/10.1115/1.4030891>
- Feintuch, A., Ruengsakulrach, P., Lin, A., Zhang, J., Zhou, Y.-Q., Bishop, J., ... Ethier, C. R. (2007). Hemodynamics in the mouse aortic arch as assessed by MRI, ultrasound, and numerical modeling. *American Journal of Physiology. Heart and Circulatory Physiology*, 292(2), H884–H892. <http://doi.org/10.1152/ajpheart.00796.2006>
- Funabashi, N., Kobayashi, Y., Perlroth, M., & Rubin, G. D. (2003). Coronary artery: quantitative evaluation of normal diameter determined with electron-beam CT compared with cine coronary angiography initial experience. *Radiology*, 226(1), 263–71. Retrieved from <http://www.ncbi.nlm.nih.gov/pubmed/12511700>
- Gao, M., Huang, J., & Zhang, S. (2011). 4D Cardiac Reconstruction Using High Resolution CT Images. *Methodology*, 153–160. http://doi.org/10.1007/978-3-642-21028-0_19
- Gatehouse, P. D., Elkinington, A. G., Ablitt, N. a, Yang, G.-Z., Pennell, D. J., & Firmin, D. N. (2004). Accurate assessment of the arterial input function during high-dose myocardial perfusion cardiovascular magnetic resonance. *Journal of Magnetic Resonance Imaging : JMRI*, 20(1), 39–45. <http://doi.org/10.1002/jmri.20054>
- George, Richard T;Ichihara, Takashi; Lima, Jaoa A.C.; Lardo, A. C. A. (2010). A Method for Reconstructing the Arterial Input Function during Helical CT : Implications for Myocardial Perfusion Distribution Imaging. *Radiology*, 255(November2-May2010), 396–404.
- George, R. T., Arbab-Zadeh, A., Miller, J. M., Kitagawa, K., Chang, H. J., Bluemke, D. A., ... Lima, J. A. C. (2009). Adenosine stress 64-and 256-row detector computed tomography angiography and perfusion imaging a pilot study evaluating the transmural extent of perfusion abnormalities to predict atherosclerosis causing myocardial ischemia. *Circulation: Cardiovascular Imaging*, 2(3), 174–182. <http://doi.org/10.1161/CIRCIMAGING.108.813766>
- George, R. T., Ichihara, T., Lima, J. A. C., & Lardo, A. C. (2010). A method for reconstructing the arterial input function during helical CT: implications for myocardial perfusion distribution imaging. *Radiology*, 255(2), 396–404. Retrieved

- from <http://dx.doi.org/10.1148/radiol.10081121>
- George, R. T., Jerosch-Herold, M., Silva, C., Kitagawa, K., Bluemke, D. A., Lima, J. A. C., & Lardo, A. C. (2007). Quantification of myocardial perfusion using dynamic 64-detector computed tomography. *Investigative Radiology*, 42(12), 815–22. <http://doi.org/10.1097/RLI.0b013e318124a884>
- George, R. T., Rahsepar, A. A., Eslami, P., Seo, J. H., Mittal, R., Zhao, D., ... Lardo, A. C. (2014). Abstract 17975: Coronary and Myocardial Blood Flow Measurements Derived from Coronary Computed Tomography Angiography and Transluminal Attenuation Flow Encoding in the Multicenter AIDS Cohort Study. *Circulation*, 130(Suppl_2), A17975–. Retrieved from http://circ.ahajournals.org/cgi/content/long/130/Suppl_2/A17975
- George, R. T., Silva, C., Cordeiro, M. A. S., DiPaula, A., Thompson, D. R., McCarthy, W. F., ... Lardo, A. C. (2006). Multidetector Computed Tomography Myocardial Perfusion Imaging During Adenosine Stress. *Journal of the American College of Cardiology*, 48(1), 153–160. <http://doi.org/10.1016/j.jacc.2006.04.014>
- Ghias, R., Mittal, R., & Dong, H. (2007). A sharp interface immersed boundary method for compressible viscous flows. *Journal of Computational Physics*, 225(1), 528–553. <http://doi.org/10.1016/j.jcp.2006.12.007>
- Gisvold, S. E., & Brubakk, a O. (1982). Measurement of instantaneous blood-flow velocity in the human aorta using pulsed Doppler ultrasound. *Cardiovascular Research*, 16(1), 26–33. Retrieved from <http://www.ncbi.nlm.nih.gov/pubmed/7060059>
- Gould, K. L., Lipscomb, K., & Hamilton, G. W. (1974). Physiologic basis for assessing critical coronary stenosis. Instantaneous flow response and regional distribution during coronary hyperemia as measures of coronary flow reserve. *The American Journal of Cardiology*, 33(1), 87–94. Retrieved from <http://www.ncbi.nlm.nih.gov/pubmed/4808557>
- Haller, G. (2005). An objective definition of a vortex. *Journal of Fluid Mechanics*, 525, 1–26. <http://doi.org/10.1017/S0022112004002526>
- Hoi, Y., Meng, H., Woodward, S. H., Bendok, B. R., Hanel, R. a., Guterman, L. R., & Hopkins, L. N. (2004). Effects of arterial geometry on aneurysm growth: three-dimensional computational fluid dynamics study. *Journal of Neurosurgery*, 101(4), 676–681. <http://doi.org/10.3171/jns.2004.101.4.0676>
- Hope, M. D., Wrenn, S. J., & Dyverfeldt, P. (2013). Clinical Applications of Aortic 4D Flow Imaging. *Current Cardiovascular Imaging Reports*, 6(2), 128–139. <http://doi.org/10.1007/s12410-012-9187-8>
- Hozumi, T., Yoshida, K., Akasaka, T., Asami, Y., Ogata, Y., Takagi, T., ... Morioka, S. (1998). Noninvasive assessment of coronary flow velocity and coronary flow velocity reserve in the left anterior descending coronary artery by Doppler echocardiography: comparison with invasive technique. *Journal of the American College of Cardiology*, 32(5), 1251–9. Retrieved from <http://www.ncbi.nlm.nih.gov/pubmed/9809933>
- Hsiao, E. M., Rybicki, F. J., & Steigner, M. (2010). CT coronary angiography: 256-slice and 320-detector row scanners. *Current Cardiology Reports*, 12(1), 68–75. <http://doi.org/10.1007/s11886-009-0075-z>
- Hsu, L.-Y., Groves, D. W., Aletras, A. H., Kellman, P., & Arai, A. E. (2012). A Fully Quantitative Pixel-Wise Measurement of Myocardial Blood Flow Using Contrast-Enhanced First-Pass Cardiac Magnetic Resonance Perfusion Imaging: Microsphere

- Validation in Dogs and Feasibility Study in Humans. *JACC. Cardiovascular Imaging*, 5(2), 154–166. <http://doi.org/10.1016/j.jcmg.2011.07.013>.A
- Hsu, M.-C., Kamensky, D., Bazilevs, Y., Sacks, M. S., & Hughes, T. J. R. (2014). Fluid--structure interaction analysis of bioprosthetic heart valves: significance of arterial wall deformation. *Computational Mechanics*, 54(4), 1055–1071. <http://doi.org/10.1007/s00466-014-1059-4>
- Hulten, E. A., Carbonaro, S., Petrillo, S. P., Mitchell, J. D., & Villines, T. C. (2011). Prognostic value of cardiac computed tomography angiography: A systematic review and meta-analysis. *Journal of the American College of Cardiology*, 57(10), 1237–1247. <http://doi.org/10.1016/j.jacc.2010.10.011>
- Ionasec, R. I., Voigt, I., Georgescu, B., Wang, Y., Houle, H., Vega-Higuera, F., ... Comaniciu, D. (2010). Patient-specific modeling and quantification of the aortic and mitral valves from 4-D cardiac CT and TEE. *IEEE Transactions on Medical Imaging*, 29(9), 1636–1651. <http://doi.org/10.1109/TMI.2010.2048756>
- Kamensky, D., Hsu, M. C., Schillinger, D., Evans, J. A., Aggarwal, A., Bazilevs, Y., ... Hughes, T. J. R. (2015). An immersogeometric variational framework for fluid-structure interaction: Application to bioprosthetic heart valves. *Computer Methods in Applied Mechanics and Engineering*, 284, 1005–1053. <http://doi.org/10.1016/j.cma.2014.10.040>
- Karmonik, C., Bismuth, J. X., Davies, M. G., & Lumsden, A. B. (2008). Computational hemodynamics in the human aorta: A computational fluid dynamics study of three cases with patient-specific geometries and inflow rates. *Technology and Health Care*, 16(5), 343–354. Retrieved from <http://www.ncbi.nlm.nih.gov/pubmed/19126973>
- Kass, M., Witkin, A., & Terzopoulos, D. (1988). Snakes: Active contour models. *International Journal of Computer Vision*. <http://doi.org/10.1007/BF00133570>
- Kilner, P. J., Yang, G. Z., Mohiaddin, R. H., Firmin, D. N., & Longmore, D. B. (1993). Helical and retrograde secondary flow patterns in the aortic arch studied by three-directional magnetic resonance velocity mapping. *Circulation*, 88(5 Pt 1), 2235–2247. <http://doi.org/10.1161/01.CIR.88.5.2235>
- Kim, T., Cheer, a Y., & Dwyer, H. a. (2004). A simulated dye method for flow visualization with a computational model for blood flow. *Journal of Biomechanics*, 37(8), 1125–36. <http://doi.org/10.1016/j.jbiomech.2003.12.028>
- Ko, B. S., Cameron, J. D., Meredith, I. T., Leung, M., Antonis, P. R., Nasis, A., ... Seneviratne, S. K. (2012). Computed tomography stress myocardial perfusion imaging in patients considered for revascularization: A comparison with fractional flow reserve. *European Heart Journal*, 33(1), 67–77. <http://doi.org/10.1093/eurheartj/ehr268>
- Koo, B. K., Erglis, A., Doh, J. H., Daniels, D. V., Jegere, S., Kim, H. S., ... Min, J. K. (2011). Diagnosis of ischemia-causing coronary stenoses by noninvasive fractional flow reserve computed from coronary computed tomographic angiograms: Results from the prospective multicenter DISCOVER-FLOW (Diagnosis of Ischemia-Causing Stenoses Obtained Via Noni. *Journal of the American College of Cardiology*, 58(19), 1989–1997. <http://doi.org/10.1016/j.jacc.2011.06.066>
- Korporaal, J. G., Benz, M. R., Schindera, S. T., Flohr, T. G., & Schmidt, B. (2016). Contrast Gradient-Based Blood Velocimetry With Computed Tomography. *Investigative Radiology*, 51(1), 41–49.

- <http://doi.org/10.1097/RLI.0000000000000202>
- Kung, E., Baretta, A., Baker, C., Arbia, G., Biglino, G., Corsini, C., ... Migliavacca, F. (2013). Predictive modeling of the virtual Hemi-Fontan operation for second stage single ventricle palliation: Two patient-specific cases. *Journal of Biomechanics*, 46(2), 423–429. <http://doi.org/10.1016/j.jbiomech.2012.10.023>
- Kupari, M., Hekali, P., & Poutanen, V. (1995). Cross sectional profiles of systolic flow velocities in left ventricular outflow tract of normal subjects, 34–39.
- Lange, R. a, & Hillis, L. D. (2003). Cardiology patient pages. Diagnostic cardiac catheterization. *Circulation*, 107(17), e111–e113. <http://doi.org/10.1161/01.CIR.0000070982.94049.A2>
- Lardo, A. C., Rahsepar, A. A., Seo, J. H., Eslami, P., Korley, F., George, R. T., & Flow, A. (2015). Computed Tomography Transluminal Attenuation Flow Encoding (TAFE): Formulation, Preclinical Validation and Clinical Feasibility. *JCCT [In Review]*.
- Lardo, A. C., Rahsepar, A. A., Seo, J. H., Eslami, P., Korley, F., Kishi, S., ... George, R. T. (2015). Estimating coronary blood flow using CT transluminal attenuation flow encoding: Formulation, preclinical validation, and clinical feasibility. *Journal of Cardiovascular Computed Tomography*, 9(6), 559–566. <http://doi.org/10.1016/j.jcct.2015.03.018>
- Ledesma-Carbayo, M., Kybic, J., Desco, M., Santos, A., Sühling, M., Hunziker, P., & Unser, M. (2005). Spatio-Temporal Nonrigid Registration for Ultrasound Cardiac Motion. *IEEE Trans. Med. Imag.*, 24(9), 1113–1126.
- Leyh, R. G., Schmidtke, C., Sievers, H. H., & Yacoub, M. H. (1999). Opening and closing characteristics of the aortic valve after different types of valve-preserving surgery. *Circulation*, 100(21), 2153–2160. <http://doi.org/10.1161/01.CIR.100.21.2153>
- Lloyd-Jones, D., Adams, R. J., Brown, T. M., Carnethon, M., Dai, S., De Simone, G., ... Wylie-Rosett, J. (2010). Executive summary: Heart disease and stroke statistics-2010 update: A report from the american heart association. *Circulation*, 121(7), 46–215. <http://doi.org/10.1161/CIRCULATIONAHA.109.192667>
- Long, C. C., Hsu, M.-C., Bazilevs, Y., Feinstein, J. A., & Marsen, A. L. (2012). Fluid–structure interaction simulations of the Fontan procedure using variable wall properties. *International Journal for Numerical Methods in Biomedical Engineering*, 28(1), 72–86. <http://doi.org/10.1002/cnm.1485>
- Maintz, J. B., & Viergever, M. A. (1998). A survey of medical image registration. *Medical Image Analysis*, 2(1), 1–36. <http://doi.org/10.1.1.39.4417>
- Mäkelä, T., Clarysse, P., Sipilä, O., Pauna, N., Cuong Pham, Q., Katila, T., & Magnin, I. E. (2013). A Review of Cardiac Image Registration Methods. *Journal of Chemical Information and Modeling*, 53(9), 1689–1699. <http://doi.org/10.1017/CBO9781107415324.004>
- Makhijani, V., Yang, H. ., Dionne, P. J., & Thubrikat, M. J. (1997). Thre Dimensional Coupled Fluid Structure Simulations of Parcardial Bioprosthetic Aortic Valve Functon. *ASAIO*, (43), 387–392.
- Markl, M., Draney, M. T., Miller, D. C., Levin, J. M., Williamson, E. E., Pelc, N. J., ... Herfkens, R. J. (2005). Time-resolved three-dimensional magnetic resonance velocity mapping of aortic flow in healthy volunteers and patients after valve-sparing aortic root replacement. *Journal of Thoracic and Cardiovascular Surgery*, 130(2), 456–463.

- <http://doi.org/10.1016/j.jtcvs.2004.08.056>
- McInerney, T., & Terzopoulos, D. (1995). A dynamic finite element surface model for segmentation and tracking in multidimensional medical images with application to cardiac 4D image analysis. *Comp. Med. Imag. Graph.*, 419(1), 69–83.
- Melikian, N., De Bondt, P., Tonino, P., De Winter, O., Wyffels, E., Bartunek, J., ... De Bruyne, B. (2010). Fractional Flow Reserve and Myocardial Perfusion Imaging in Patients With Angiographic Multivessel Coronary Artery Disease. *JACC: Cardiovascular Interventions*, 3(3), 307–314. <http://doi.org/10.1016/j.jcin.2009.12.010>
- Miller, M. I., Trounev, A., & Younes, L. (2002). On the metrics and euler-lagrange equations of computational anatomy. *Annual Review of Biomedical Engineering*, 4, 375–405. <http://doi.org/10.1146/annurev.bioeng.4.092101.125733>
- Min, J. K., Leipsic, J., Pencina, M. J., Berman, D. S., Koo, B.-K., van Mieghem, C., ... Mauri, L. (2012). Diagnostic accuracy of fractional flow reserve from anatomic CT angiography. *Jama*, 308(12), 1237–45. <http://doi.org/10.1001/2012.jama.11274>
- Min, J. K., Shaw, L. J., Devereux, R. B., Okin, P. M., Weinsaft, J. W., Russo, D. J., ... Callister, T. Q. (2007). Prognostic Value of Multidetector Coronary Computed Tomographic Angiography for Prediction of All-Cause Mortality. *Journal of the American College of Cardiology*, 50(12), 1161–1170. <http://doi.org/10.1016/j.jacc.2007.03.067>
- Mittal, R., Dong, H., Bozkurtas, M., Najjar, F. M., Vargas, A., & von Loebbecke, A. (2008). A versatile sharp interface immersed boundary method for incompressible flows with complex boundaries. *Journal of Computational Physics*, 227(10), 4825–4852. <http://doi.org/10.1016/j.jcp.2008.01.028>
- Mittal, R., Seo, J. H., Vedula, V., Choi, Y. J., Liu, H., Huang, H. H., ... George, R. T. (2015). Computational modeling of cardiac hemodynamics: Current status and future outlook. *Journal of Computational Physics*, 305, 1065–1082. <http://doi.org/10.1016/j.jcp.2015.11.022>
- Morbiducci, U., Ponzini, R., Rizzo, G., Cadioli, M., Esposito, A., De Cobelli, F., ... Redaelli, A. (2009). In vivo quantification of helical blood flow in human aorta by time-Resolved three-dimensional cine phase contrast magnetic resonance imaging. *Annals of Biomedical Engineering*, 37(3), 516–531. <http://doi.org/10.1007/s10439-008-9609-6>
- Mori, D., & Yamaguchi, T. (2002). Computational fluid dynamics modeling and analysis of the effect of 3-D distortion of the human aortic arch. *Computer Methods in Biomechanics and Biomedical Engineering*, 5(3), 249–60. <http://doi.org/10.1080/10255840290010698>
- Motoyama, S., Kondo, T., Sarai, M., Sugiura, A., Harigaya, H., Sato, T., ... Narula, J. (2007). Multislice Computed Tomographic Characteristics of Coronary Lesions in Acute Coronary Syndromes. *Journal of the American College of Cardiology*, 50(4), 319–326. <http://doi.org/10.1016/j.jacc.2007.03.044>
- Motoyama, S., Sarai, M., Harigaya, H., Anno, H., Inoue, K., Hara, T., ... Narula, J. (2009). Computed Tomographic Angiography Characteristics of Atherosclerotic Plaques Subsequently Resulting in Acute Coronary Syndrome. *Journal of the American College of Cardiology*, 54(1), 49–57. <http://doi.org/10.1016/j.jacc.2009.02.068>
- Nakanishi, R., & Budoff, M. J. (2014). A New Approach in Risk Stratification by Coronary

- CT Angiography. *Scientifica*, 2014.
- Nakazato, R., Park, H. B., Berman, D. S., Gransar, H., Koo, B. K., Erglis, A., ... Min, J. K. (2013). Noninvasive fractional flow reserve derived from computed tomography angiography for coronary lesions of intermediate stenosis severity results from the DeFACTO study. *Circulation: Cardiovascular Imaging*, 6(6), 881–889. <http://doi.org/10.1161/CIRCIMAGING.113.000297>
- Numata, S., Itatani, K., Kanda, K., Doi, K., Yamazaki, S., Morimoto, K., ... Yaku, H. (2016). Blood flow analysis of the aortic arch using computational fluid dynamics. *European Journal of Cardio-Thoracic Surgery*, 49(January), e459. <http://doi.org/10.1093/ejcts/ezv459>
- Parker, G. J. M., Roberts, C., Macdonald, A., Buonaccorsi, G. A., Cheung, S., Buckley, D. L., ... Jayson, G. C. (2006). Experimentally-derived functional form for a population-averaged high-temporal-resolution arterial input function for dynamic contrast-enhanced MRI. *Magnetic Resonance in Medicine*, 56(5), 993–1000. <http://doi.org/10.1002/mrm.21066>
- Patel, M. R., Peterson, E. D., Dai, D., Brennan, J. M., Redberg, R. F., Anderson, H. V., ... Douglas, P. S. (2010). Low diagnostic yield of elective coronary angiography. *The New England Journal of Medicine*, 363(1), 93–94; author reply 94–95.
- Peyrat, J. M., Delingette, H., Sermesant, M., Pennec, X., Xu, C., & Ayache, N. (2008). Registration of 4D time-series of cardiac images with multichannel Diffeomorphic Demons. *Lecture Notes in Computer Science (Including Subseries Lecture Notes in Artificial Intelligence and Lecture Notes in Bioinformatics)*, 5242 LNCS(PART 2), 972–979. <http://doi.org/10.1007/978-3-540-85990-1-117>
- Pijls, N. H. J., de Bruyne, B., Peels, K., van der Voort, P. H., Bonnier, H. J. R. M., Bartunek, J., & Koolen, J. J. (1996). Measurement of Fractional Flow Reserve to Assess the Functional Severity of Coronary-Artery Stenoses. *New England Journal of Medicine*, 334(26), 1703–1708. <http://doi.org/10.1056/NEJM199606273342604>
- Port, R. E., Knopp, M. V., & Brix, G. (2001). Dynamic contrast-enhanced MRI using Gd-DTPA: Interindividual variability of the arterial input function and consequences for the assessment of kinetics in tumors. *Magnetic Resonance in Medicine*, 45(6), 1030–1038. <http://doi.org/10.1002/mrm.1137>
- Prevrhal, S., Forsythe, C. H., Harnish, R. J., Saeed, M., & Yeh, B. M. (2011). CT Angiographic Measurement of Vascular Blood Flow Velocity by Using Projection Data. *Radiology*, 261(3), 923–929. <http://doi.org/10.1148/radiol.11110617>
- Ranga, A., Bouchot, O., Mongrain, R., Ugolini, P., & Cartier, R. (2006). Computational simulations of the aortic valve validated by imaging data: evaluation of valve-sparing techniques. *Interactive Cardiovascular and Thoracic Surgery*, 5(4), 373–378. <http://doi.org/10.1510/ievts.2005.121483>
- Rangayyan, R. . (2005). *Biomedical Image Analysis*. CRC press-Taylor & Francis group.
- Richard T. George, Amir Ali Rahsepar, Jung-Hee Seo, Parastou Eslami, F. K. K., & Rajat Mittal, A. C. L. (2014). Abstract: Application of Translumenal Attenuation Flow Encoding (TAFE) to Quantify Absolute Coronary Blood Flow. *SCCT 9th Annual Scientific Meeting*, 7–9.
- Roger, V. L., Go, A. S., Lloyd-Jones, D. M., Adams, R. J., Berry, J. D., Brown, T. M., ... Wylie-Rosett, J. (2011). Heart disease and stroke statistics-2011 update: A report from the American Heart Association. *Circulation*, 123(4).

- <http://doi.org/10.1161/CIR.0b013e3182009701>
- Salvi, J., Matabosch, C., Fofi, D., & Forest, J. (2007). A review of recent range image registration methods with accuracy evaluation. *Image and Vision Computing*, 25(5), 578–596. <http://doi.org/10.1016/j.imavis.2006.05.012>
- San Román, J. a, Vilacosta, I., Castillo, J. a, Rollán, M. J., Hernández, M., Peral, V., ... Fernández-Avilés, F. (1998). Selection of the optimal stress test for the diagnosis of coronary artery disease. *Heart (British Cardiac Society)*, 80(4), 370–376.
- Schaller, R. R. (1997). Moore's law: past, present and future. *Spectrum, IEEE*, 34(6), 52–59. <http://doi.org/10.1109/6.591665>
- Seed, W. A., & Wood, N. B. (1971). Velocity patterns in the aorta. *Cardiovascular Research*, 5(3), 319–330. <http://doi.org/10.1093/cvrese/5.3.319>
- Segadal, L., & Matre, K. (1987). Blood velocity distribution in the human ascending aorta. *Circulation, Vascular Heart Disease*, 76(1), 90–100.
- Sengupta, D., Kahn, A. M., Burns, J. C., Sankaran, S., Shadden, S. C., & Marsden, A. L. (2012). Image-based modeling of hemodynamics in coronary artery aneurysms caused by Kawasaki disease. *Biomechanics and Modeling in Mechanobiology*, 11(6), 915–932. <http://doi.org/10.1007/s10237-011-0361-8>
- Seo, J. H., Abd, T., George, R. T., & Mittal, R. (2016). *A Coupled Chemo-Fluidic Computational Model for Thrombogenesis in Infarcted Left Ventricles. American Journal of Physiology - Heart and Circulatory Physiology*. <http://doi.org/10.1152/ajpheart.00855.2015>
- Seo, J. H., & Mittal, R. (2011). A sharp-interface immersed boundary method with improved mass conservation and reduced spurious pressure oscillations. *Journal of Computational Physics*, 230(19), 7347–7363. <http://doi.org/10.1016/j.jcp.2011.06.003>
- Shahcheraghi, N., Dwyer, H. a, Cheer, a Y., Barakat, a I., & Rutaganira, T. (2002). Unsteady and three-dimensional simulation of blood flow in the human aortic arch. *Journal of Biomechanical Engineering*, 124(4), 378–387. <http://doi.org/10.1115/1.1487357>
- Shen, D., Sundar, H., Xue, Z., Fan, Y., & Litt, H. (2005). Consistent estimation of cardiac motions by 4D image registration. *Medical Image Computing and Computer-Assisted Intervention : MICCAI ... International Conference on Medical Image Computing and Computer-Assisted Intervention*, 8(Pt 2), 902–10. http://doi.org/10.1007/11566489_111
- Staniak, H. L., Bittencourt, M. S., Pickett, C., Cahill, M., Kassop, D., Slim, A., ... Hultén, E. (2014). Coronary CT angiography for acute chest pain in the emergency department. *Journal of Cardiovascular Computed Tomography*, 8(5), 359–367. <http://doi.org/10.1016/j.jcct.2014.08.001>
- Steigner, M. L., Mitsouras, D., Whitmore, A. G., Otero, H. J., Wang, C., Buckley, O., ... Rybicki, F. J. (2010). Iodinated contrast opacification gradients in normal coronary arteries imaged with prospectively ECG-gated single heart beat 320-detector row computed tomography. *Circulation. Cardiovascular Imaging*, 3(2), 179–86. <http://doi.org/10.1161/CIRCIMAGING.109.854307>
- Stuijzand, W. J., Danad, I., Rajmakers, P. G., Marcu, C. B., Heymans, M. W., van Kuijk, C. C., ... Knaapen, P. (2014). Additional value of transluminal attenuation gradient in CT angiography to predict hemodynamic significance of coronary artery stenosis.

- JACC. Cardiovascular Imaging*, 7(4), 374–86.
<http://doi.org/10.1016/j.jcmg.2013.12.013>
- Sun, Z. (2013). Cardiac Imaging Modalities in the Diagnosis of Coronary Artery Disease. *Journal of Clinical & Experimental Cardiology*, 1–4. <http://doi.org/10.4172/2155-9880.S6-e001>
- Svensson, J., Gårdhagen, R., Heiberg, E., Ebberts, T., Loyd, D., Länne, T., & Karlsson, M. (2006). Feasibility of patient specific aortic blood flow CFD simulation. *Medical Image Computing and Computer-Assisted Intervention: MICCAI ... International Conference on Medical Image Computing and Computer-Assisted Intervention*, 9(Pt 1), 257–63. Retrieved from <http://www.ncbi.nlm.nih.gov/pubmed/17354898>
- Swanson, W. M., & Clark, R. E. (1973). Aortic valve leaflet motion during systole. Numerical-graphical determination. *Circulation Research*, 32(1), 42–48. <http://doi.org/10.1161/01.RES.32.1.42>
- Taylor, C. A., Fonte, T. A., & Min, J. K. (2013). Computational fluid dynamics applied to cardiac computed tomography for noninvasive quantification of fractional flow reserve: Scientific basis. *Journal of the American College of Cardiology*, 61(22), 2233–2241. <http://doi.org/10.1016/j.jacc.2012.11.083>
- Taylor, G. (1953). Dispersion of Soluble Matter in Solvent Flowing Slowly through a Tube. *Proceedings of the Royal Society A: Mathematical, Physical and Engineering Sciences*, 219(1137), 186–203. <http://doi.org/10.1098/rspa.1953.0139>
- Tonino, P. A. ., de Bruyne, B., Pijls, N. H. J., Siebert, U., Ikeno, F., Van 't Veer, M., ... Fearon, W. F. (2009). Fractional Flow Reserve versus Angiography for Guiding Percutaneous Coronary Intervention. *The New England Journal of Medicine*, 360(3), 333–340.
- Van Der Vorst, H. A. (1992). BI-CGSTAB: A FAST AND SMOOTHLY CONVERGING VARIANT OF BI-CG FOR THE SOLUTION OF NONSYMMETRIC LINEAR SYSTEMS, 13(2), 631–644.
- Vedula, V., Seo, J. H., Lardo, A. C., & Mittal, R. (2016). Effect of trabeculae and papillary muscles on the hemodynamics of the left ventricle. *Theoretical and Computational Fluid Dynamics*, 30(1-2), 3–21. <http://doi.org/10.1007/s00162-015-0349-6>
- Vincent Ho, & Reddy, G. P. (2010). *Cardiovascular Imaging- Volume 2: (1 Har/Psc)*. Saunders, Philadelphia.
- WD, F., & M., K. (2003). Computed tomography angiography: principles and clinical applications. *J Comput Assist Tomogr.*, 27(Supp 1), 23–30.
- Wentland, A. L., Grist, T. M., & Wieben, O. (2014). Review of MRI-based measurements of pulse wave velocity: a biomarker of arterial stiffness. *Cardiovascular Diagnosis and Therapy*, 4(2), 193–206. <http://doi.org/10.3978/j.issn.2223-3652.2014.03.04>
- Wong, D. T. L., Ko, B. S., Cameron, J. D., Nerlekar, N., Leung, M. C. H., Malaiapan, Y., ... Seneviratne, S. K. (2013). Transluminal Attenuation Gradient in Coronary Computed Tomography Angiography Is a Novel Noninvasive Approach to the Identification of Functionally Significant Coronary Artery Stenosis: A Comparison With Fractional Flow Reserve. *Journal of the American College of Cardiology*, 61(12). <http://doi.org/10.1016/j.jacc.2012.12.029>
- Wu, J. Z., Xiong, A. K., & Yang, Y. T. (2005). Axial stretching and vortex definition. *Physics of Fluids*, 17(3). <http://doi.org/10.1063/1.1863284>
- Yoon, Y. E., Choi, J.-H., Kim, J.-H., Park, K.-W., Doh, J.-H., Kim, Y.-J., ... Park, Y.-B.

- (2012). Noninvasive Diagnosis of Ischemia-Causing Coronary Stenosis Using CT Angiography: Diagnostic Value of Transluminal Attenuation Gradient and Fractional Flow Reserve Computed From Coronary CT Angiography Compared to Invasively Measured Fractional Flow Reserve. *JACC. Cardiovascular Imaging*, 5(11), 1088–96. <http://doi.org/10.1016/j.jcmg.2012.09.002>
- Young, S. W., Noon, M. A., & Marincek, B. (1980). Dynamic Computed Tomography Time Density Study of Normal Human Tissue after Intravenous Contrast Administration. *Investigative Radiology*.
- Zang, Y., Street, R. L., & Koseff, J. R. (1994). A Non-staggered Grid, Fractional Step Method for Time-Dependent Incompressible Navier-Stokes Equations in Curvilinear Coordinates. *Journal of Computational Physics*. <http://doi.org/10.1006/jcph.1994.1146>
- Zheng, M., Wei, M., Wen, D., Zhao, H., Liu, Y., Li, J., & Li, J. (2015). Transluminal attenuation gradient in coronary computed tomography angiography for determining stenosis severity of calcified coronary artery: a primary study with dual-source CT. *European Radiology*, 25(5), 1219–1228. <http://doi.org/10.1007/s00330-014-3519-9>
- Zheng, Y., John, M., Liao, R., Boese, J., Kirschstein, U., Georgescu, B., ... Comaniciu, D. (2010). Automatic Aorta Segmentation and Valve Landmark Detection in C-Arm CT: Application to Aortic Valve Implantation. *Medical Image Computing and Computer-Assisted Intervention - Miccai 2010, Pt I*, 6361(12), 476–483. Retrieved from <Go to ISI>://WOS:000287946100058

Parastou Eslami

Email: peslami20@gmail.com

Phone: (415)857-5352

Education	JOHNS HOPKINS UNIVERSITY – BALTIMORE, MD: PHD	2012 – 2016
	<ul style="list-style-type: none">• Graduate Partnership Program Fellow at NIH• Creel Family Teaching Assistant Award• Mentor at SABES (STEM Achievement in Baltimore Elementary Schools)• Society of Women in Engineering	
	STANFORD UNIVERSITY – STANFORD, CA : M.S	2008 – 2010
	UNIVERSITY OF CALIFORNIA, BERKELEY– BERKELEY, CA: B.S	2005 – 2008
	<ul style="list-style-type: none">• Graduated: Best Chemistry Student of the year Award, Best Math Student of the year Award, Jet Propulsion Laboratory Undergraduate Scholar• Activities: Pi Tau Sigma Honor Society, Women in Engineering Society	
Work Experience	Cardiac MR PET CT PROGRAM at MGH- <i>Post-doctoral Fellow</i>	Boston, MA
	June 2016- Present	
	FLOW PHYSICS & COMPUTATION LAB – <i>PhD Candidate</i>	
	Baltimore, MD	
	Jan 2012- June 2016	
	<ul style="list-style-type: none">• Decoding coronary blood flow information from CT imaging techniques.• Analyzing patient specific coronary CT images to extract Transluminal Attenuation Gradient• Validating the analytical flow rate formulation with computational and CT compatible phantom data• Developing automated and simulation ready patient specific computational models in cerebral aneurysms• Analyzing the risk for rupture or restructure of cerebral aneurysms	
	L-3 COMMUNICATIONS – <i>Engineer II</i>	San Diego, CA
	2010- 2012	
	<ul style="list-style-type: none">• Analyzed finite element simulation to better understand head and helmet interactions in various impacts and head injuries	
	NEUROMUSCULAR BIOMECHANICS LABORATORY–<i>Independent Study</i>	
	Stanford, CA	
	Spring 2010	
	<ul style="list-style-type: none">• Assisted with finite element analysis to define knee joint muscle forces in patients with patellofemoral pain with MRI imaging techniques.	
	STANFORD COMPUTATIONAL BIOMECHANICS LAB–<i>Research Assistant</i>	
	Stanford, CA	
	2008-2010	

- Developed a simulation/model to define solid properties and wall motions of an infarcted ovine left ventricle based on empirical measurements using MatLab
- Observed surgery on implantation of titanium markers for the empirical measurements

CARDIOVASCULAR BIOMECHANICS LAB–*Summer Intern* UC San Francisco, CA
2008-2010

- Simulated the mechanical properties of an akinetic and dyskinetic ovine heart based on actual measurements
- Implication: in analyzing dilated cardiomyopathy and its correlated stiffness
- Observed surgery and helped with data collection on implantation of titanium markers for the empirical measurements

NON-LINEAR DYNAMICS AND TRANSPORT LAB–*Research Undergraduate*
UC Berkeley, CA

2007-2008

- Simulated an analytical model for the maximum bubble growth in a cluster
- Important to kidney stone treatment and biofluidics industry

Journal Publications

Eslami P, Seo J, Rahsepar A, George R, Lardo AC, Mittal R. “Computational Study of Computed Tomography Contrast Gradients in Models of Stenosed Coronary Arteries”. J Biomech Eng.;137(9):091002-091002-11. doi:10.1115/1.4030891. September 2015

Albert C. Lardo, Amir Ali Rahsepar, Jung Hee Seo, **Parastou Eslami**, Frederick Korley, Satoru Kishi, Thura Abd, Rajat Mittal, Richard T. George. “Estimating Coronary Blood Flow using Computed Tomography Transluminal Attenuation Flow Encoding (TAFE): Formulation, Preclinical Validation and Clinical Feasibility.” *Journal of Cardiovascular Computed Tomography*, (10.1016/j.jcct.2015.03.018), March 30, 2015

Wenk, J.F., **Eslami, P.**, Zhang, Z., Xu, C., Kuhl, E., Gorman, J.H., Robb, J.D., Ratcliffe, M.B., Gorman, R.C., and Guccione, J.M., “A Novel Method for Quantifying the In-Vivo Mechanical Effect of Material Injected into a Myocardial Infarction,” *Annals of Thoracic Surgery*, (2011;92:935-941), April 26, 2011

Abstracts & Conference Proceedings

Parastou Eslami, Jung-Hee Seo, Thura Abd, Albert C. Lardo, Marcus Y. Chen, Rajat Mittal Computational Modeling of the Dispersion of Contrast in the Aorta and Implications for the Estimation of Coronary Flow Rates via Coronary Transluminal Gradients. BMES/FDA Frontiers in Medical Devices Conference; May 23-25, 2016; Washington, DC.

Parastou Eslami, Jung-Hee Seo, Albert C. Lardo, Marcus Chen, Rajat Mittal. Decoding Hemodynamics of Large Vessels via Contrast Dispersion of Contrast Agent in Cardiac Computed Tomography. In Proceedings of the 68th Annual Meeting of the APS Division of Fluid Dynamics; November 24–26, 2015; Boston, Massachusetts

Parastou Eslami, Jung-Hee Seo, Amir Ali Rahsepar, Richard George, Albert C. Lardo, Rajat Mittal. Novel Non-invasive Estimation of Coronary Blood Flow using Contrast Advection in Computed Tomography Angiography. In

Proceedings of the 67th Annual Meeting of the APS Division of Fluid Dynamics; November 24–26, 2014; San Francisco, California

Parastou Eslami, Jung-Hee Seo , Albert C. Lardo , Rajat Mittal.
Hemodynamics and flow-vessel interaction in patient-specific aorta using unified lattice Boltzmann computation and simulation. In Proceedings of the 66th Annual Meeting of the APS Division of Fluid Dynamics; November 24–26, 2013; Pittsburgh, Pennsylvania

Richard T. George, Amir Ali Rahsepar, Jung-Hee Seo, **Parastou Eslami** and A. C. L. Rajat Mittal, “Abstract: Application of Transluminal Attenuation Flow Encoding (TAFE) to Quantify Absolute Coronary Blood Flow,” *SCCT 9th Annu. Sci. Meet.*, pp. 7–9, 2014

R. T. George, A. A. Rahsepar, **P. Eslami**, J. H. Seo, R. Mittal, D. Zhao, E. Guallar, L. P. Jacobson, M. Budoff, W. S. Post, and A. C. Lardo, “Abstract 17975: Coronary and Myocardial Blood Flow Measurements Derived from Coronary Computed Tomography Angiography and Transluminal Attenuation Flow Encoding in the Multicenter AIDS Cohort Study,” *Circulation*, vol. 130, no. Suppl_2, p. A17975–, Nov. 2014.

A.C. Lardo, J.H. Seo, **P. Eslami**, R. Mittal, Computational Fluid Dynamics Predicts Correlations between Transluminal Contrast and Pressure Gradients in Models of Stenosed Arteries, *Circulation* 126 (21 Supplement), A19280- Nov 2012.

A. J. Szeri, J. Toilliez, C. Heckman, **P. Eslami**, Bubble-bubble interaction in disperse bubble clouds, Acoustics '08, Paris, June 29-July 4, 2008.

Patents & Disclosures

Fortran, MatLab, C ++, LSDYNA, ANSYS, ABAQUS, TrueGrid, Rapidform, Comsol, ANSYS CFX, MIMICS, Paraview, ITKSNAP, Vitrea, Solid Works, Pro-Engineering,

Qualifications & Skills

Fluent in Persian (Farsi)